

RICE UNIVERSITY

**Effects of the Charge Exchange of Solar Wind with the
Martian Exosphere**

by

Yue Chen

A THESIS SUBMITTED
IN PARTIAL FULFILLMENT OF THE
REQUIRMENT FOR THE DEGREE

Doctoral of Philosophy

APPROVED, THESIS COMMITTEE:

Paul A. Cloutier, Chair, Professor of Physics and
Astronomy

Richard A. Wolf, Professor of Physics and
Astronomy

Edison P. Liang, Professor of Physics and
Astronomy

Andre W. Droxler, Professor of Earth Science

Houston, TEXAS

DECEMBER, 2002

EFFECTS OF THE CHARGE EXCHANGE OF SOLAR WIND WITH THE MARTIAN EXOSPHERE

by

YUE CHEN

ABSTRACT

Charge exchange of solar wind with the Martian exosphere is shown to have two-fold consequences. From the solar wind perspective, the thermal pressure is removed by charge exchange with Martian neutral particles. To maintain a constant total pressure in the flow, increase of magnetic field occurs and therefore accounts for the formation of the magnetic pileup boundary observed by the Mars Global Surveyor Magnetometer. To simulate this a fluid model is constructed and results from it are shown to successfully fit observations. On the other hand, the Martian exosphere is affected by the charge exchange, too. Compared to Venus, Mars has an ionosphere that is so dilute that charge exchange of solar wind should play an important role in the formation of a nonthermal Martian hydrogen exosphere component. In order to study quantitatively how the Martian exosphere is influenced by it, we develop a 3-dimensional Monte Carlo exosphere model in which effects of charge exchange with solar wind are isolated. Simulation results show the existence of that hot population does change the exospheric temperature structure greatly, and we also investigate the simulation results by calculating the contribution of the hot component to Ly- α emission and comparing it with data acquired by Mariners' ultraviolet spectrometers. Finally, it is concluded that charge exchange is important in the interaction between solar wind and Martian exosphere. Output of our models can be used in future modeling and data analysis for the coming Mars missions.

Acknowledgements

First I would express my great appreciation to my advisor Dr. Paul A. Cloutier for the origination of my thesis topics and all his guidance along the whole way. I am grateful for his unique approach to the graduate school experience, for all the meetings of research group, and especially for showing me how physics can be illustrated and interpreted. Of course, I can't forget the happy time of Air-chair days, either. No one could ask for a better advisor. I would like to also thank Dana Crider for being so generous with offering help anytime. Thanks to MGS MAG/ER team for useful discussions. Thanks for Dr. Richard Hodges for providing his original Monte Carlo codes. I am also grateful to all the members of this department for putting up with me.

My parents have been great helpful and many thanks to you for your unending encouragements and supports. Most importantly, I want to thank my dear wife, Yang Jin. She is always there waiting for me and cozying my heart when I feel stuck. It is her eternal love that accompanies me during the past five years, even in the hardest time, and lights my brain up. This dissertation would be dedicated to her specifically.

The work leading towards this dissertation was supported by NASA and JPL under grant numbers CIT-JPL-1207348, NAG5-7037, and JPL-NASA-1230020.

TABLE OF CONTENTS

1. Introduction	1
2. Interactions Between Solar Wind and Non-magnetic Obstacles	4
2.1 Solar wind Interactions	4
2.2 The Class of Non-magnetic and Conducting Obstacles	6
2.3 Solar Wind Interaction with Mars	7
3. Planetary Exosphere	13
3.1 Classical Exosphere Theory	14
3.2 Collisional Exosphere	21
3.3 Exosphere Observation	31
3.4 Mars Atmosphere and Exosphere	33
4. Solar Wind Charge Exchange with Martian Exosphere	42
4.1 Magnetic Pileup Boundary Observed by MGS	42
4.2 Underlying Physical Picture	45
4.3 Fluid Model of Solar Wind	47
4.4 Model Results	58
5. Martian H Exosphere Charge Exchange with Solar wind	67
5.1 Underlying Physical Picture	67
5.2 Monte Carlo Model of Martian Hydrogen Exosphere	71
5.3 Model Results	79
6. Discussions	99
6.1 Effects of Charge Exchange on Solar Wind	99

6.2 Effects of Charge Exchange on Martian Hydrogen Exosphere	100
7. Conclusions	107
7.1 Summary of Results	107
7.2 Future Work and Prospects	109
References	111
Appendix: Missions to Mars	119

1. Introduction

Mars is one of the solar system planets lacking the protection from the solar wind by a strong global magnetic field. Primarily solar wind can penetrate deeply and interact directly with the Martian atmosphere until it is finally diverted and stopped by the Martian ionosphere. In this interaction the charge exchange of solar wind proton with the Martian exosphere plays an important role and has a strong influence on both incident solar wind and Martian exosphere.

On one hand, by analyzing data from Magnetometer/Electron Reflectometer (MAG/ER) onboard Mars Global Surveyor (MGS) has identified the existence of the magnetic pileup boundary (MPB), which locates the beginning of the magnetic pileup region. Within this boundary, the observed magnetic field grows so precipitously that previous solar wind-ionosphere models cannot explain it, therefore implying the presence of some other factor(s). When we take effects of the Martian exospheric neutral particles into account, these observations become understandable. In this picture, the solar wind protons are removed directly from the flow by charge exchange with Martian exospheric neutrals and therefore the solar wind plasma loses part of its thermal pressure. In order to keep the total pressure constant, the magnetic field has to increase to compensate. In this way the magnetic field piles up more efficiently than usual and behaves as we observed. A fluid model of the solar wind is developed to test this idea.

On the other hand, the structure of the Martian exosphere should be altered by the charge exchange, too. As with other solar system planets, Mars has an atmosphere and therefore an exosphere. Although sharing many characteristics with that of the Earth, the Martian exosphere has been and is being directly exposed to the solar wind because any

global Martian magnetic field died out billions of years ago. This means that the solar wind can interact with the Martian exosphere, by charge exchange and electron impact ionization followed by pick-up, more strongly than it does on the Earth. This can help to explain why the loss rate of Martian exosphere calculated by some models has the same order of magnitude of that of the Earth. Charge exchange with high speed and high temperature solar wind protons is expected to produce very energetic neutral particles and therefore a nonthermal exospheric component can be produced in such a way and change the exospheric profiles. To study this problem quantitatively, a Monte Carlo model of the Martian hydrogen exosphere is constructed and effects of charge exchange with solar wind are thoroughly studied.

Although the problem of charge exchange has been studied before, to my knowledge, this is the first attempt to connect charge exchange with the enhancement of post-shock solar wind magnetic field. Additionally, due to the lack of sufficient in-situ measurements, we have sparse knowledge of the Martian hydrogen exosphere. Consequently, few have attempted to study quantitatively how the Martian exosphere is changed by the charge exchange.

In this thesis there are two main blocks included to deal with the effects of charge exchange on solar wind and exosphere separately. After providing a background of the general solar wind interaction firstly and then specifically that of a non-magnetic obstacle, we discuss the classical picture of a planetary exosphere and introduce some former models. Afterwards our current knowledge of the Martian atmosphere/exosphere and models of Martian exosphere are discussed. Then model of charge exchange between solar wind and Martian exosphere is presented to demonstrate the role of charge

exchange in the formation of Martian magnetic pileup boundary; the calculation simultaneously provides the charge exchange rates. Whereafter by employing results from the first model, we use a Monte Carlo method to construct a Martian hydrogen exosphere model with all relevant physical processes included to study the effects of charge exchange.

After the discussion of the results, a final note will be made as to the relation of this research to the exploration of Mars or other similar solar system objects theoretically and practically. The effects of charge exchange should be considered in models describing the interaction between solar wind and similar obstacles. Furthermore, applying the results expounded here, future mission teams may have better estimates of what to expect with regard to the exospheric temperature and density structure, aiding instrument design and data analysis.

2. Interaction Between Solar Wind and Non-magnetic Conducting Obstacles

In this section we present our current knowledge of the interaction between solar wind and Mars. First is a general outline of the solar wind interaction with solar system objects, followed by the characteristics of the non-magnetic conducting obstacle class. The last section describes the latest observations of Mars.

2.1 Solar wind interactions

The solar wind, a collection of highly magnetized plasma originating from the solar surface and traveling through interplanetary space supersonically and super-alfvenically, sweeps across the whole solar system. Planets and moons, behaving somewhat like stones in a river, interact with and change the solar wind flowing around them. Despite the diverse characteristics carried by different obstacles, Spreiter et al. [1970], according to data acquired, divided the interaction with solar wind into three different basic types, as are represented by the Moon, the Earth and Venus, respectively. Accordingly, three classes of obstacles are defined by whether or not the obstacle has an ionosphere or/and intrinsic magnetic field sufficiently strong to divert the solar wind flow around itself [Law, 1995], and cartoons illustrating how they interacts with the solar wind are displayed in figure 2.1.

The interaction between the solar wind and a Moon-like body, which has neither atmosphere nor magnetic field, is the simplest type (see figure 2.1a). Without being diverted by any obstacle, the solar wind particles travel undisturbed until they impact the Lunar surface and then are absorbed and neutralized. Consequently there is no bow shock (except for some regions with exceptional minor and weak crustal magnetic field [Lin et al., 1998]). Also, because the Moon is an insulator, the interplanetary magnetic field lines

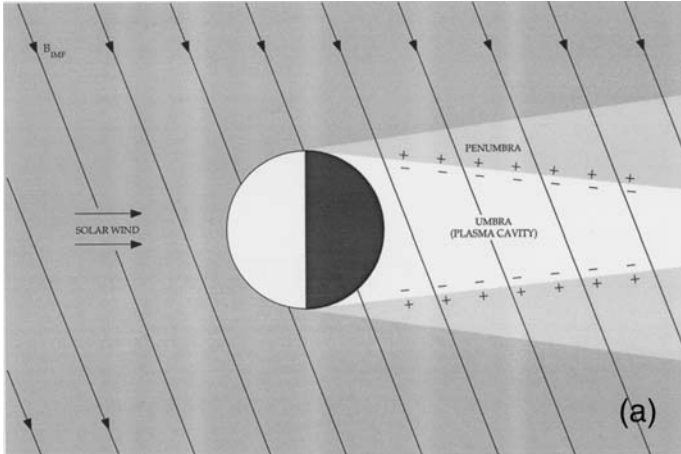
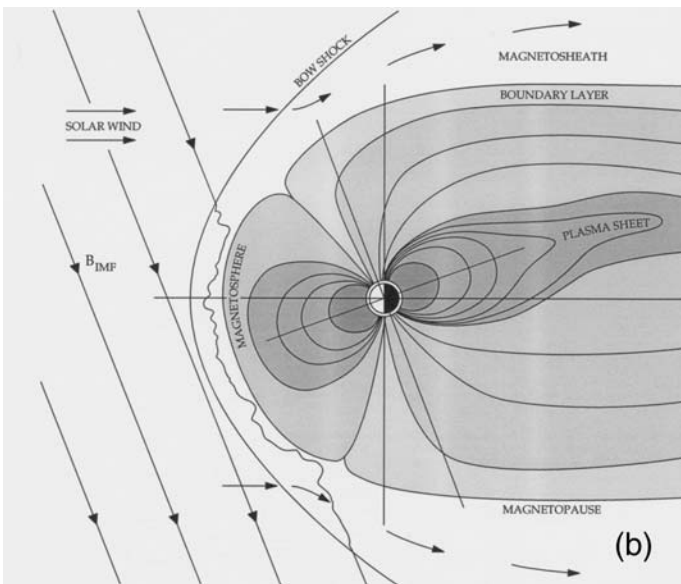
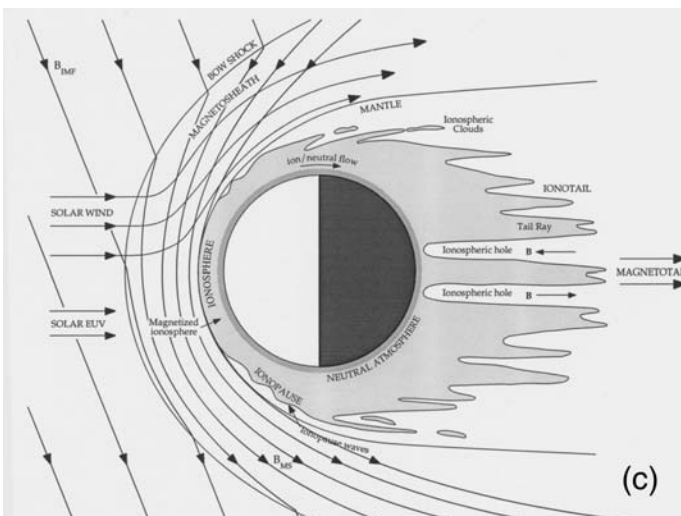


Figure 2.1 Solar wind interaction with solar system objects (after Law [1995]).

(a) Moon-like case: solar wind interacts with a non-conducting object with neither atmosphere nor intrinsic magnetic field; no shock forms due to the absorption of the incident flow.



(b) Earth-like case: solar wind interacts with an obstacle which has an intrinsic magnetic field which is so strong that solar wind is stopped far from the planet and diverted around; bow shock forms through which solar wind flow is decelerated to subsonic.



(c) Venus-like case: solar wind interacts with an obstacle with no intrinsic magnetic field but ionosphere and dense atmosphere; bow shock forms due to mass load of solar wind.

can diffuse through unimpeded. In other word, solar wind particles cannot feel the existence of the Moon until they reach it and the magnetic field behaves as if the Moon did not exist at all. In this case, neither magnetic field nor solar wind accumulate on the dayside while on the nightside, due to the shield of the Moon, a plasma-free cavity forms into which solar wind plasma diffuses.

Objects with an intrinsic magnetic field and atmosphere, such as Earth, interact totally differently with the solar wind (see figure 2.1b). It is this type that has been studied most intensively. Unlike the case of the Moon, the solar wind interacts with the strong planetary intrinsic magnetic field instead of the hard planetary surface. Solar wind magnetic field reconnects with intrinsic magnetic field and the magnetosphere forms. The magnetosphere acts as an obstacle to prevent the solar wind from approaching too near to the planet, and a bow shock upstream of the magnetosphere decelerates the solar wind to subsonic speed. In this case, except for a small fraction of solar wind being able to penetrate the magnetospheric barrier and enter the upper atmosphere along cusp open lines, the planetary atmosphere and ionosphere hardly have direct contact with solar wind particles.

2.2 The class of non-magnetic, conducting obstacles

The third type of interactions can be taken as the intermediate case between the Moon-like and Earth-like cases. This class of obstacles includes objects such as Venus, Mars, and comets approaching the Sun. Unlike the Earth, none of the objects in this class have significant intrinsic magnetic field to stand off the solar wind. However, unlike the Moon, they do have atmospheres that, like the Earth's, can be ionized partly by solar EUV to form an ionosphere, which is dense enough that the solar wind is prevented from

penetrating too deeply into the planetary atmosphere. The main obstacle in this type of interaction with the solar wind is the ionosphere and atmosphere, which deflect the solar wind; a bow shock forms upstream of the object to slow down the solar wind flow. The solar wind magnetic field lines pile up in front and drape around the obstacle because of the high ionospheric conductivity. Venus is the typical instance in this class and major features of its interaction with solar wind are shown in figure 2.1c. In this type of interaction the solar wind transfers its momentum to the planet through the ionosphere. Fluid models by Spreiter et al. [1972] and Spreiter and Stahara [1980; 1992] give good simulation results to the Venus-like interaction.

This class of obstacles can be categorized into two subclasses: Venus standing for the high mass limit and comets standing for the low mass limit [Crider, 1999]. The small gravity of comets leads to a cometic atmosphere extending much further out, and cometary ionospheres generally cover a wide range of distance [Cravens, 1989]. A weak bow shock can form and a magnetic pileup boundary occurs between the bow shock and nucleus [Neubauer et al., 1986]. Solar wind interacts strongly with the comet atmosphere and carries away large numbers of cometary particles. Detailed descriptions of the above two subclasses can be found in Law [1995], Coates [1997] and Crider [1999].

Mars, being very similar to Venus in many aspects, has been argued to belong to either the Earth-like or Venus-like class for long time. The conclusion has not been drawn until the success of Mars Global Surveyor (MGS) in the late 1990's and we discuss it in the next section.

2.3 Solar wind interaction with Mars

Before the arrival of MGS, although Mars was one of the planets mostly intensively observed by missions (refer to the Appendix) that include flying-by, orbiting and landing schemes, the solar wind interaction with Mars was ironically less well understood than that with more distant Jovian planets [Law, 1995]. This odd situation results from the fact that spacecraft reaching Mars either did not carry proper instrument or did not have a good geometric position to observe the magnetic field at low altitude! Therefore even though analysis of in-situ data shows that the Martian atmosphere and ionosphere share many characteristics with that of Venus, the argument of whether the interaction between solar wind and Mars is Venus-like or Earth-like or hybrid type lasted for decades. During that time, people tried to determine whether Mars is magnetized or not by different approaches. Studies led by the dynamo theory [Luhmann et al., 1992] drew a conclusion that a weak Martian magnetic dipole may have ceased. Curtis [1988] studied the SNC meteorites and concluded that Martian dynamo died a long time ago but a remnant magnetic field existed and played a part in the solar wind interaction. The majority of researchers studied this problem by checking the pressure balance or the shape and location of different boundaries, such as bow shock, magnetosheath, ionosphere, and etc., and seemed to reach the same conclusion: Mars must have an intrinsic magnetic field which looks much weaker than that of the Earth. Models of solar wind interacting with Mars in different ways have also been developed (Venus-like by Cloutier et al. [1969]; Hybrid by Intrilligator [1979]).

The true picture finally emerged when MGS reached Mars in 1997. The MAG/ER [Acuna et al, 1992] onboard MGS and the low altitude of periapsis made it for the first time possible to measure any Martian intrinsic magnetic field. Acuna et al. [1998]

reported the initial results: no significant intrinsic magnetic field but multiple magnetic

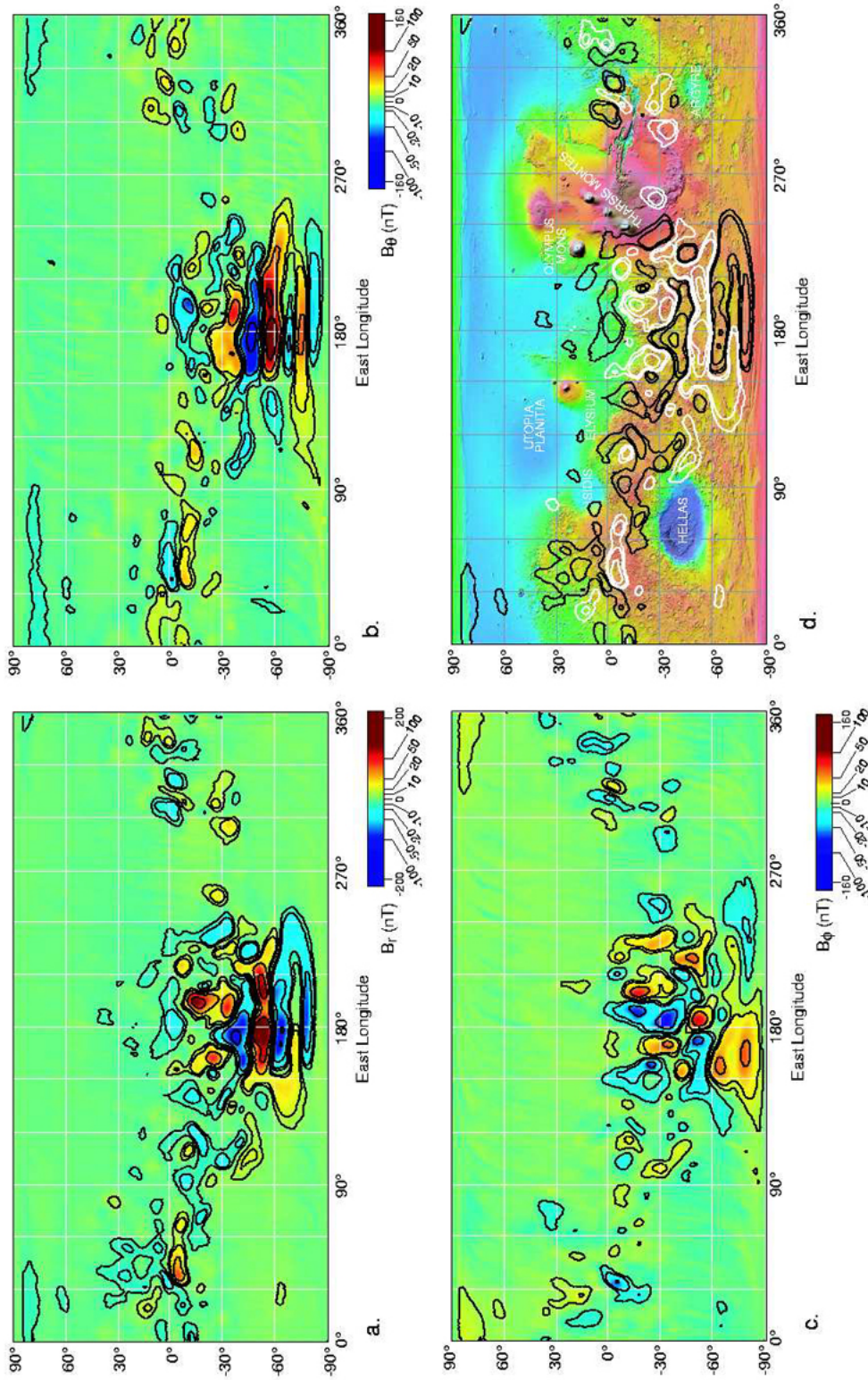


Figure 2.2 Map of the magnetic field of Mars at 400(+/-30) km altitude. The radial component (a) of the field is shown with a colorbar scaled to +/-220nT; the theta (b) and phi (c) components share a colorbar with reduced scale (180nT). Comparison of radial field contours with MOLA topography(d). Isomagnetic contours are drawn for $B = \pm 10, 20, 50, 200$ nT (Copy from Connerney et al.,[2001]).

anomalies with small scale were detected. This discovery was confirmed by continued observation by MAG/ER and identified to be crustal remanent magnetic field [Connerney et al., 1999]. The intensity, distribution and configuration of those magnetic field are shown in figure 2.2 [Connerney, 1999; 2001].

So now we can safely say that the conducting Martian ionosphere presents the main obstacle to the solar wind and the interaction between solar wind and Mars is basically Venus-like [Cloutier, 1999], especially at high altitude. This is the static, averaged picture of the interaction on one hand. On the other hand, at low altitude, especially in the southern hemisphere, effects of localized and sometimes quite strong crustal magnetic anomalies have been observed in the ionosphere. The superposition of the anomaly field and the interplanetary magnetic fields can substantially alter the local field topology. Cartoons in figure 2.3 depict the sum magnetic field in two specified cases in which the anomaly field is simplified to a dipole. Furthermore, evidence of exchange of photoelectrons and solar wind electrons along reconnected magnetic field lines, for the reason above described, has been reported by Michell et al. [1999] and one example of the observed electron spectra is shown in figure 2.4 [Walker and Chen, 1999]. Moreover, because of the planets' rotation, the effects of the abnormal magnetic field would be dynamic. This is the time-dependent picture of interaction.

Currently, significant interest has arisen in the study of interaction between solar wind and Mars with effects of the magnetic anomalies included and some simulation models have been constructed [e.g. Ma et al., 2001]. However, in this dissertation, we still take the simplified picture that the interaction between solar wind and Mars is

Venus-like, since we are concerned with large altitudes; this point will be clarified furthermore when the development of the fluid model is introduced in section 4.

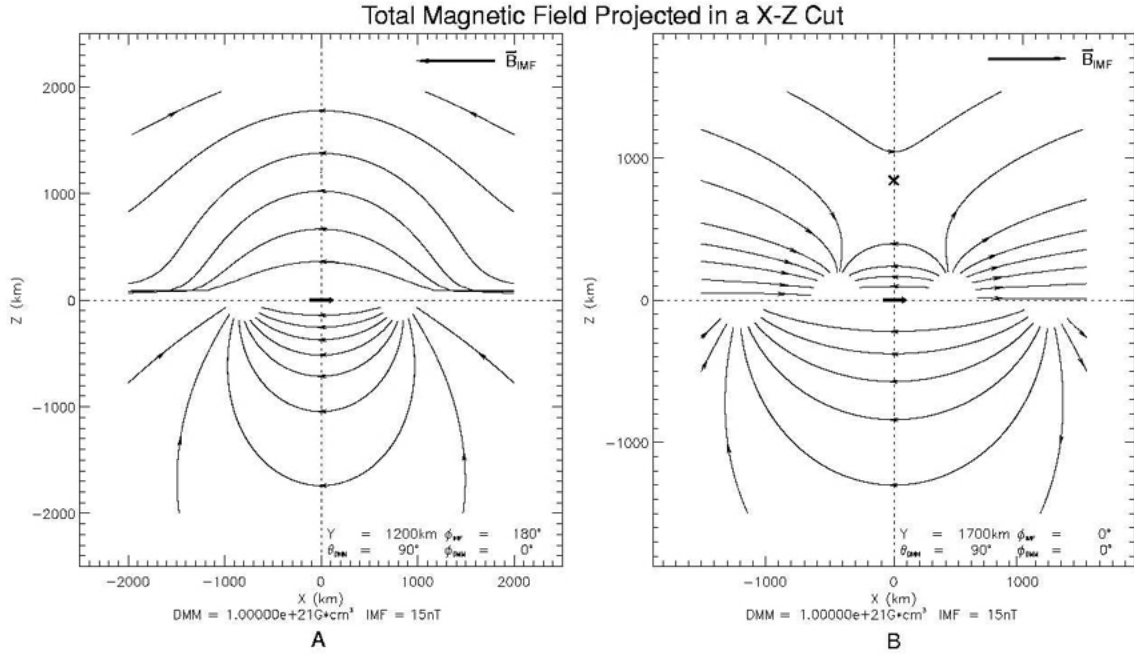


Figure 2.3 Magnetic field topology, shown in XZ cut, calculated from simple model that combines the uniform horizontal-oriented interplanetary magnetic field (IMF) in the upper-half free space with the field of a dipole locating on the origin. Magnetic field lines in two typical cases are shown: **A.** “Speed-bump” case, in which the orientation of dipole is anti-parallel to that of IMF pointing to +Z direction. The thick arrow in the panel’s upper right corner denotes the direction of IMF. Parameters of dipole and IMF are shown in the lower right corner and Y is the position of this XZ plane on y-axis. The subtitle shows that the magnetic moment of the dipole is $1 \times 10^{21} \text{ G} \cdot \text{cm}^3$ and IMF has magnitude of 15nT. In this case, the ionosphere may be raised locally, and the ionosphere transfer between dayside and nightside could be impeded. **B.** “Pot-hole” case. Here direction of IMF is parallel to that of the dipole. Reconnection can happen in this case and the “X” in the panel shows the sketchy location of the neutral point. Open filed lines like those of Earth cusp form in this case and planetary origin plasma and solar wind charged particles can both move along them and exchange with each other.

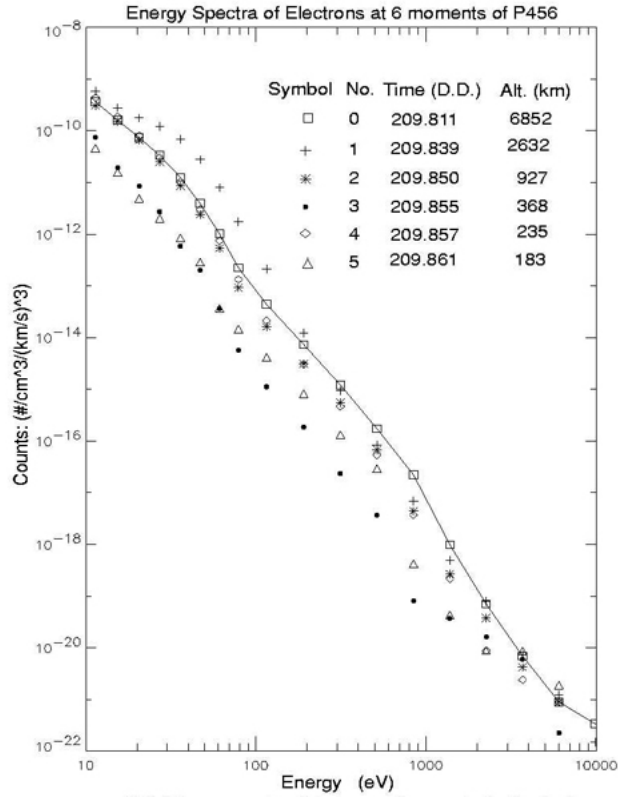


Figure 2.4 Energy spectra of electron at 6 moments observed by ER onboard MGS. Altitude and time (in unit of decimal day) of the six positions are given in the panel. Note the similarity between the spectra at moment 2 (with altitude 927km) and 4 (with altitude 235km), especially for electron with energy below 1000eV(data in that range is more reliable), This similarity strongly implies the exchange between ionosphere and solar wind plasmas.

3. Planetary Exosphere

According to Hunten [1990], the concept of exosphere, in which neutral particles move ballistically with rare collisions, was first introduced by G.J. Stoney in his paper in 1868, long before the dawn of the Space Age. Although it may be true that Stoney brought up the idea of planetary atmospheric thermal escaping as early as in 1880, it was Jeans who originally presented and studied this problem theoretically in 1925, from whence the term "Jeans escape" was coined. After endeavors from many researchers, the theory of collisionless exosphere came to maturity when Chamberlin published his milestone paper in 1963 and finally provided a solid reference with which the observation can be compared. However, it's only one half of the whole picture. Back in 1952 the study of helium loss by Spitzer showed that thermal escape may not be the only way of losing atmosphere. That is the first indication that an exosphere theory including nonthermal loss procedure, i.e., the collisional exosphere theory, is important. From then on and until today, much theoretical and model development work has been done, and solving the relevant Boltzmann equation and constructing a three dimensional collisional exosphere has remained intriguing and arduous.

Knowledge of the exosphere is important not only in the field of kinetic theory research but also in the framework of the global study of the terrestrial environment and planetary evolution. Furthermore, practical interest rises when it is a matter of defining spacecraft's aerodynamic characteristics, estimating manmade satellite orbital lifetime, choosing the most suitable orbits for orbiters, and even predicting the environment around an astronaut or cosmonaut who is doing space walking, maintenance or retrieval jobs. In short, study of the exosphere is necessary both to research and space exploration.

Subsequently section 3.1 introduces briefly the description of the classical collisionless exosphere theory. Then some general comments on the collisional exosphere theory, which focuses on the effects of nonthermal processes in planetary atmospheres, can be found in section 3.2. Section 3.3 briefly presents observations of the exosphere. Finally we introduce our current knowledge about the Martian exosphere/atmosphere as well as research works and models based on it.

3.1 Classical (Collisionless) Exosphere Theory

Planetary exospheres involve two major issues: one is the density and temperature profiles [Herring and Kyle, 1961; Öpik and Singer, 1960 and 1961; Aamodt and Case, 1962], and the other is how to calculate the escaping flux [Jean, 1925]. On one hand, those two issues are independent: by studying the first one we can have a picture of general planetary exosphere and the answer to the second problem can provide us clues of atmosphere evolution; on the other hand, those two issues are interrelated and can be solved simultaneously by employing kinetic theory to get the particles' velocity distribution functions. The classical collisionless theory is actually a specified branch dealing with a simplified exosphere. Before moving on, I will present a brief description of a planetary atmosphere.

Generally, with increasing altitude, a planetary atmosphere can be divided into three regions: homosphere, heterosphere and exosphere. Homosphere is the lowest portion of the atmosphere with homogenous composition caused by the strong vertical turbulent motions. This part of the atmosphere interacts directly with the planetary surface. Above it is the heterosphere, in which molecular diffusion takes over the role of turbulence so that vertical distribution of individual gases is determined by their

respective masses. According to the hydrodynamic theory, atmosphere with the assumption of constant temperature abides by hydrostatic equilibrium equation of the i th constituent,

$$dp_i/dr = -GMn_im_i/r^2 \quad (3.1.1)$$

where pressure is $p_i = n_i kT$, G is the gravitational constant, M is the planetary mass and m_i is the molecular mass of the i th constituent. Integration of (3.1.1) can give barometric density variation with radial distance r ,

$$n_i(r) = n_i(r_0) \exp[\lambda_i(r) - \lambda_i(r_0)] \quad (3.1.2)$$

where r_0 is the reference level, and

$$\lambda_i(r) = GMm_i/kTr \quad (3.1.3)$$

So each species has its own scale height

$$H_i(r) = r/\lambda_i(r) = kT/m_i g(r) \quad (3.1.4)$$

and $g(r)$ is the gravitational acceleration. If we set $z = r - r_0$ and discard all nonlinear expansion of the term in square brackets in (3.1.2), then we obtain density profile in a familiar exponential form

$$n_i(r) = n_i(r_0) \exp\left[-\frac{z}{H_i(r_0)}\right] \quad (3.1.5)$$

Obviously, one direct consequence of the above diffusive equilibrium theory is that lighter component dominates over heavier ones at high altitude.

Above the heterosphere is the exosphere, which is the topmost part of the atmosphere beyond exobase. The exobase or critical level r_c is defined, in an artificial way in most cases, as the altitude on which the mean free path l equals the scale height of the major constituent, that is,

$$l = 1/n\sigma = H(r_c) \quad (3.1.6)$$

where σ is the cross section of collision with major constituent. In standard models [Jeans, 1925; Chamberlain, 1963] the exosphere is simplified to be collisionless while the atmosphere below is collision dominated. As we know, hydrodynamic theory is valid only for fluid with small Knudsen number ($Kn = l/H$) whereas collisionless kinetic theory is valid with large Kn . Although the Boltzmann equation is valid for the whole range of Knudsen number [Shizgal and Arkos, 1996], unfortunately, to date solving the Boltzmann equation with $Kn \sim 1$ has not been achieved. Therefore some approximation must be made.

First let us see how Jean made the first attempt to calculate the exospheric escape rate which has obviously been overestimated. With the assumption of a Maxwellion distribution at r_c ,

$$f^M = n(m/2\pi kT)^{3/2} \exp(-mv^2/2kT) \quad (3.1.7)$$

Jeans (1925) calculated the escape flux by integrating over velocity space with speeds greater than the escape speed, that is,

$$F_J = 2\pi \int_{v_{esc}}^{\infty} \int_{\theta=0}^{\pi/2} f^M \cos \theta v^3 d(\cos \theta) dv \quad (3.1.8)$$

So that the Jeans escape flux, or thermal escape flux, is given by integration (3.1.8) at r_c

$$F_J = \frac{n_c}{2} \sqrt{\frac{2kT_c}{m\pi}} (1 + \lambda_c) e^{-\lambda_c} \quad (3.1.9)$$

Here subscript 'c' denotes values at critical level. Table 3.1.1 shows the escape velocity and energies and exospheric values for Hydrogen from terrestrial planets by employing (3.1.9).

Table 3.1.1 Escaping velocity, energies and exospheric values for hydrogen (based on Table 1 & 2 in Shizgal and Arkos [1996])

Planet	$r_c(km)^*$	$T_c(K)$	$v_{esc}(km/s)$	$E_{esc}^H(eV)$	λ_c^H	$F_J^H/n_c^H(cm/s)$
Venus	200	275	10.2	0.54	22.89	1.65×10^{-4}
Earth	500	1000	10.8	0.61	7.06	7.94×10^2
Mars	250	350	4.8	0.12	3.99	6.48×10^2

* Parameters with subscript 'c' indicate values at critical level

It's evident that an exosphere can't keep its isotropic Maxwellian distribution function. Some modification must be made to the Jeans' calculation. In the following, some details of the standard model are presented. This model was first conceived by Opik and Singer [1960, 1961] and did not come to its maturity until Chamberlain published his milestone paper in 1963. Afterwards many other workers (for example, McAfee [1967], Fahr and Paul [1976], Fahr and Shizgal [1983], and etc.) reviewed and applied this model again and again, so the notation used in the following is the most popular set.

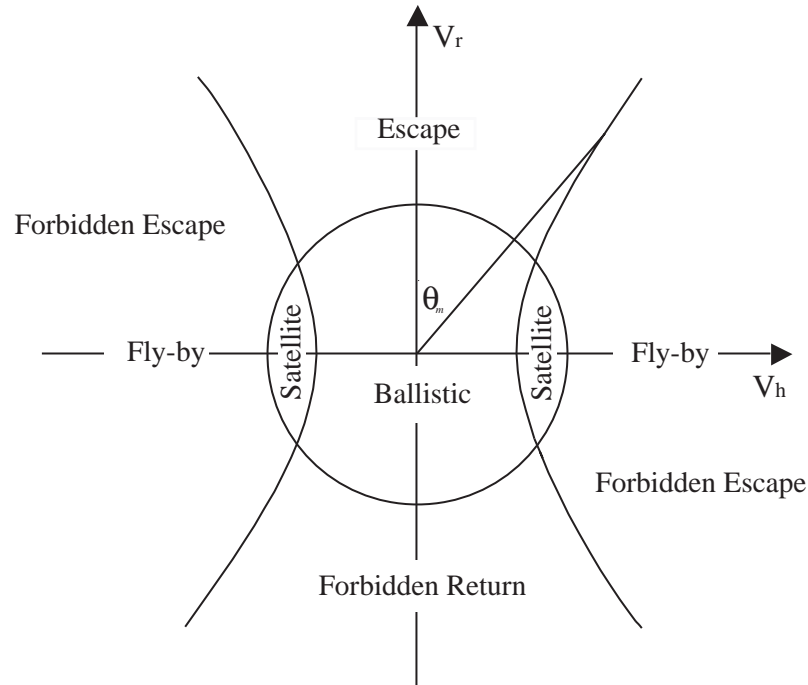


Figure 3.1 Illustration of groups of particles in velocity space due to trajectory type

In the standard model, exospheric particles moving in conic trajectories without collisions with each other are influenced by the gravity field only and can be categorized into three groups (ballistic, satellite and escaping) depending on the particles' energy and angular momentum. Conservation of energy and angular momentum give

$$\frac{1}{2}mv_c^2 - \frac{GMm}{r_c} = \frac{1}{2}mv^2 - \frac{GMm}{r} \quad (3.1.10)$$

and

$$r_c v_c \sin \theta_c = r v \sin \theta \quad (3.1.11)$$

where θ is the angle between \vec{r} and \vec{v} . Or, in dimensionless form, (3.1.10) and (3.1.11) can be rewritten into

$$V_c^2 - 1 = V^2 - y \quad (3.1.12)$$

$$y V_c \sin \theta_c = V \sin \theta \quad (3.1.13)$$

where $V = v/v_{esc}(r_c)$ and $y = r_c/r$. Here (3.1.12) and (3.1.13) are governing equations of particle movement, and types of trajectories are determined by initial values of V and θ (θ_m in the plot) as illustrated in figure 3.1. In this plot groups of particles at a specified y or r are shown in the (V_r, V_h) plane, where $V_r = V \cos \theta$ and $V_h = V \sin \theta$. In the plot two boundaries are worthy of mention: the first one is defined by $V_r^2 + V_h^2 = y$, that is the circle with radius of \sqrt{y} inside of which are non-escaping particles and outside escaping; the second is defined by equation

$$V_h^2 - [y^2/(1-y^2)]V_r^2 = V_b^2 \quad (3.1.14)$$

where $V_b^2 = y^2/(1+y)$, that is the hyperbolic curve which divides the velocity plane into two parts; the one including the origin stands for particles with orbits capable of crossing

the exobase and the other includes particles that always move above the exobase always.

The critical polar angle of the velocity of particles on the hyperbola is given by

$$\theta_m^c = \arcsin\left(\frac{y\sqrt{V^2+1-y}}{V}\right) \text{ as } V \geq V_b \quad (3.1.15)$$

In Table 3.1.2 we can find a summary of divisions of exospheric particles at specified r into five groups: ballistic, satellite, escaping, forbidden escape and forbidden return [Fahr and Shizgal, 1983; Hodges, 1993]. Then by assuming thermal equilibrium at the exobase, we can obtain the density profile of i^{th} group by integrating partially the distribution function over permitted velocity space, that is,

$$n_i = 2\pi n_{bar} \left(\frac{\lambda_c}{\pi}\right)^{\frac{3}{2}} \iint_{(\theta,V) \text{ partial}} \exp(-\lambda_c V^2) V^2 \sin\theta dV d\theta \quad (3.1.16)$$

Table 3.1.2 Types of exospheric particles (based on Table 2 in Fahr and Shizgal [1983])

Particle Type	Orbit Character	Range of V	Range of θ^{***}	Region in (V_r, V_h) Plane
Ballistic (B)	Bound elliptic with $r_{\min} < r_c$	$0 \leq V \leq \sqrt{y}$	$0 \leq \theta \leq \theta_m^c$	$\{\text{Inside solid circle}\} \cap \{\text{inside hyperbola}\}$
Satellite (S)	Bound elliptic with $r_{\min} \geq r_c$	$V_b \leq V \leq \sqrt{y}$	$\theta_m^c < \theta \leq \frac{\pi}{2}$	$\{\text{Inside solid circle}\} \cap \{\text{outside hyperbola}\}$
Escaping (E)	Nonbound hyperbolic with $r_{\min} < r_c$	$\{V > \sqrt{y}\} \cap \{V_r > 0\}$	$0 \leq \theta \leq \theta_m^c$	$\{\text{outside solid circle}\} \cap \{\text{inside hyperbola}\} \cap \{V_r > 0\}$
Forbidden Escape (FE)*	Nonbound hyperbolic with $r_{\min} \geq r_c$	$V > \sqrt{y}$	$\theta_m^c < \theta \leq \frac{\pi}{2}$	$\{\text{outside solid circle}\} \cap \{\text{outside hyperbola}\}$
Forbidden Return (FR)**	Nonbound hyperbolic with $r_{\min} < r_c$	$\{V > \sqrt{y}\} \cap \{V_r < 0\}$	$0 \leq \theta \leq \theta_m^c$	$\{\text{outside solid circle}\} \cap \{\text{outside hyperbola}\} \cap \{V_r < 0\}$

* Sometimes forbidden escape and forbidden return particles are called incoming particles (I) together.

** Sometimes the sum of all forbidden and satellite particles are called fly-by particles.

*** In the upper half-plane, which is symmetric to the lower half-plane for B, S and FE particles.

where n_{bar} is the barometric density defined as (3.1.2) with $r_0 = r_c$. Therefore, if we denote the incomplete gamma function as $\gamma(\alpha, z) = \int_0^z e^{-t} t^{\alpha-1} dt$ and complete gamma function $\Gamma(\alpha) = \gamma(\alpha, \infty)$, then density profile of each class of particle is

$$n_B(y) = \frac{2}{\sqrt{\pi}} n_{bar} \left\{ \gamma\left(\frac{3}{2}, \lambda_c y\right) - \sqrt{1-y^2} \exp\left(-\frac{\lambda_c y^2}{1+y}\right) \gamma\left(\frac{3}{2}, \lambda_c \frac{y}{1+y}\right) \right\} \quad (3.1.17)$$

$$n_S(y) = \frac{2}{\sqrt{\pi}} n_{bar} \left\{ \sqrt{1-y^2} \exp\left(-\frac{\lambda_c y^2}{1+y}\right) \gamma\left(\frac{3}{2}, \lambda_c \frac{y}{1+y}\right) \right\} \quad (3.1.18)$$

$$n_E(y) = \frac{1}{\sqrt{\pi}} n_{bar} \left\{ [\Gamma\left(\frac{3}{2}\right) - \gamma\left(\frac{3}{2}, \lambda_c y\right)] - \sqrt{1-y^2} \exp\left(-\frac{\lambda_c y^2}{1+y}\right) [\Gamma\left(\frac{3}{2}\right) - \gamma\left(\frac{3}{2}, \lambda_c \frac{y}{1+y}\right)] \right\} \quad (3.1.19)$$

$$n_I(y) = n_{bar} \left\{ \left[1 - \frac{1}{\sqrt{\pi}} (\Gamma\left(\frac{3}{2}\right) + \gamma\left(\frac{3}{2}, \lambda_c y\right))\right] + \sqrt{\frac{1-y^2}{\pi}} \exp\left(-\frac{\lambda_c y^2}{1+y}\right) [\Gamma\left(\frac{3}{2}\right) - \gamma\left(\frac{3}{2}, \lambda_c \frac{y}{1+y}\right)] \right\} \quad (3.1.20)$$

where $n_I = n_{FE} + n_{FR} = n_{FE} + n_E$, $n_B + n_S + n_E + n_I = n_{bar}(y)$ and the barometric density $n_{bar}(y) = n_c \exp[-\lambda_c(1-y)]$ are observed. Figure 3.2 and 3.3 show how the contribution from each class of hydrogen particles varies with the altitude and exobase temperature as well as how the departure from Maxwellian distribution builds up with altitude on the Earth and Mars, respectively. Additionally, temperature profiles can also be calculated in this model and we will take this part of calculation in the Martian case to section 3.4.2 as a theoretical reference with which the results from Monte Carlo model can be compared. It should be pointed out that satellite and incoming particles could be expected only if a complete Maxwellian distribution still exists at level y above the exobase, although it can never be true in a collisionless exosphere with only Maxwellian at exobase assumed. In the standard collisionless exosphere model, incoming particles are excluded, but satellite particle is included! This dilemma can only be solved in a collisional model. More details can be found in the next section.

Above we present the collisionless exosphere theory. However, although many calculations based on the standard collisionless exosphere model have been carried out to interpret many observation results successfully [like Johnson and Fish, 1960; Johnson, 1961, as we will discuss in section 3.3, it is clear that the concept of a collisionless exosphere is inconsistent with the existence of satellite particles. To solve this dilemma, collisional exosphere theory must be employed.

3.2 Collisional Exosphere

Despite the simplicity and success of the collisionless exosphere model as we present above, both practical and theoretical reasons for rectifying its inherent deficiency led to the birth of collisional exosphere model. Furthermore, the inconsistent between the observance of the Jeans escape flux and the calculation result indicates that the role of nonthermal processes in the planetary exosphere is significant [Hunten, 1982].

Generally, although the collisional exosphere models are constructed in different ways to deal with different problems, four aspects listed as follows in this field are of the most interest to us:

- 1) Effects of departure from Maxwell distribution at the exobase. Due to the loss of particles at the high-speed end, the distribution function around the exobase actually departs from Maxwellian so that the escaping flux should be smaller than Jeans predicted escaping flux that has been show in (3.1.8). Theoretical and numerical works on this issue can be found in papers by Shizgal and Lindenfeld [1980], Chamberlain and Campbell [1967], Chamberlain and Smith [1971], and etc.

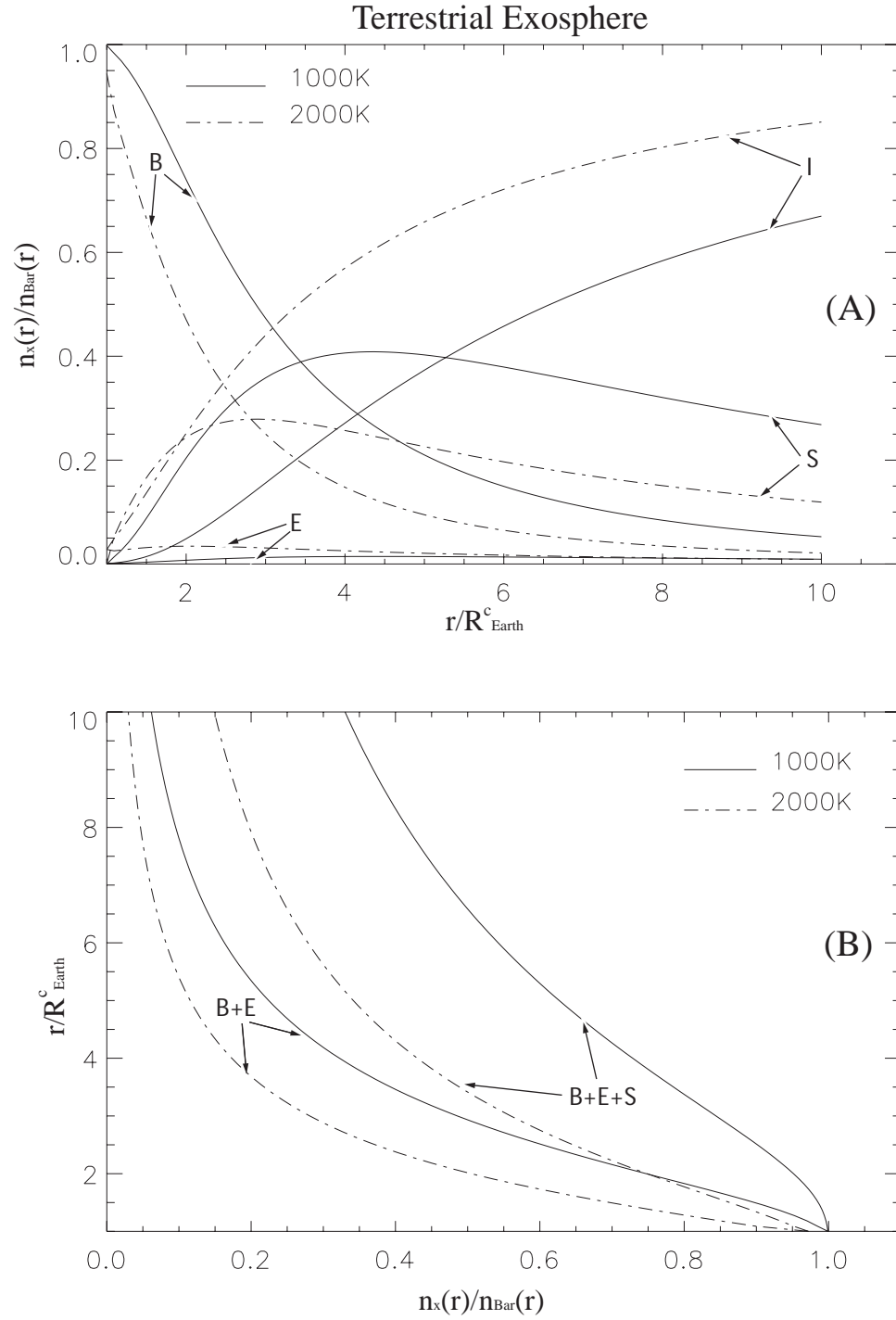


Figure 3.2 Normalized terrestrial hydrogen exosphere density profiles with exobase (with altitude 500km) temperature equals to 1000K and 2000K. (A) Ratio of each class of exospheric particle to the barometric density vs radial distance from the planet center. (B) Normalized density profiles. In case B+E includes ballistic and escaping parts; while B+E+S further includes satellite part (based from Fahr and Shizgal [1983]).

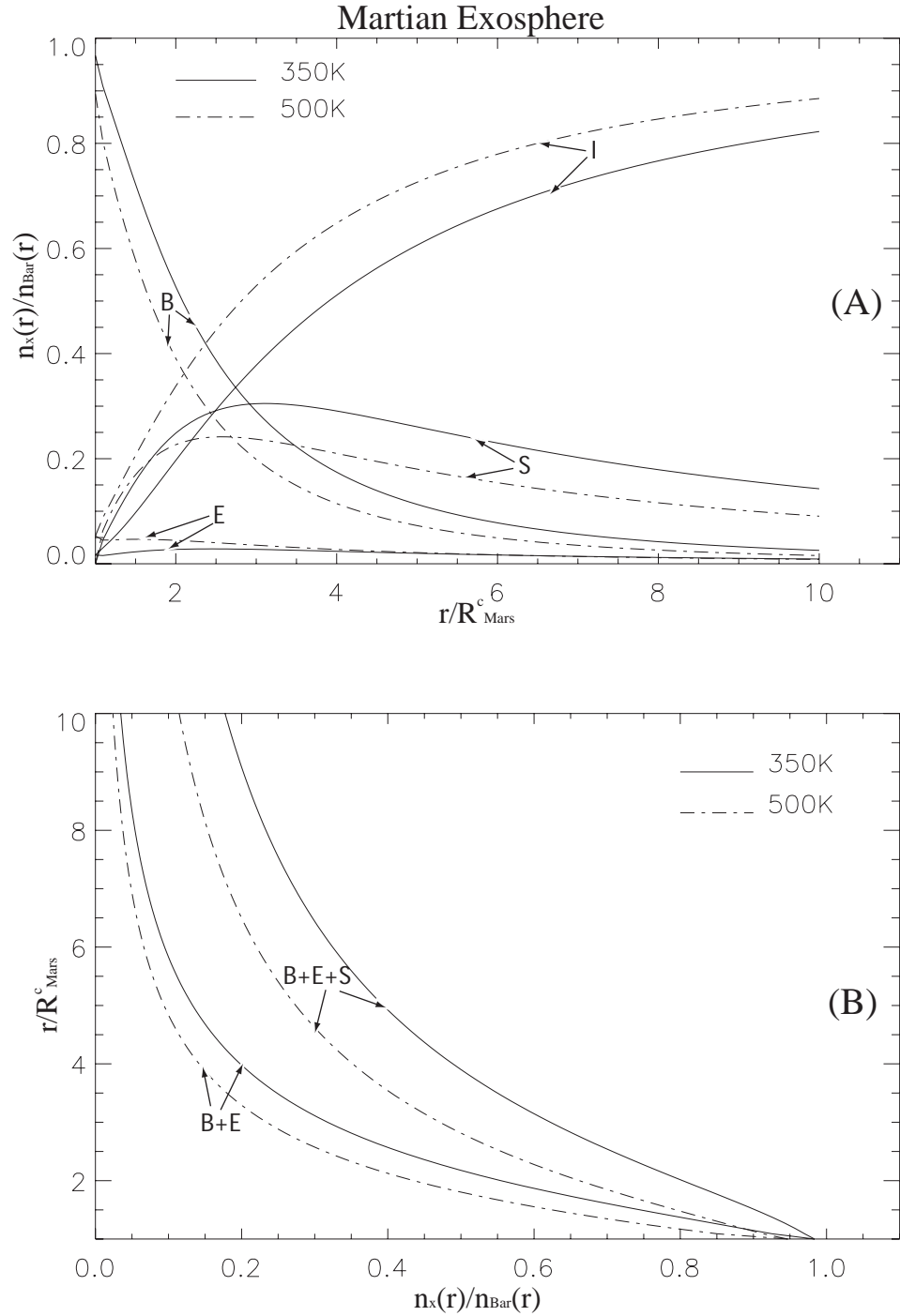


Figure 3.3 Normalized Martian hydrogen exosphere density profiles with exobase (with altitude 250km) temperature equals to 350K and 500K. (A) Ratio of each class of exospheric particle to the barometric density vs radial distance from the planet center. (B) Normalized density profiles. In case B+E includes ballistic and escaping parts; while B+E+S further includes satellite part.

- 2) Correctly represent the transition region from $Kn \ll 1$ to $Kn \gg 1$. This is equivalent to finding a proper description of the exobase with the artificial discontinuity removed and unfortunately so far, to my knowledge, a theoretical solution is still far from being achieved except for several simplified cases [Hays and Liu, 1965; Ziering et. Al., 1968]. However, measures in numerical efforts have been taken by Hodges [1994] by moving the calculation boundary downward below the exobase (if this notion still applies) and into the upper atmosphere. This method can avoid the boundary effects brought by the exobase concept but the drawback is that people need a good knowledge of the upper atmosphere, and a lot of extra computation time will be consumed in the lower region.
- 3) Satellite particles. Explanation of the discrepancy of the existence of satellite particles in collisionless exosphere model is the original motivation for introducing the collisional exosphere theory. Chamberlain [1963] and Chamberlain and Hunten [1987] have presented the mathematical description of the distribution of the satellite particles. The production and destruction of satellite particles are mainly controlled by physical processes such as the exospheric collisions [Ritcher et al., 1979], solar radiation [Chamberlain, 1979], and charge exchange [Ritcher et al., 1979] with solar wind proton [Fahr and Shizgal, 1983]. All above processes will be taken into account in this dissertation.
- 4) Effects of nonthermal processes, especially interaction between solar wind and exosphere. This is actually connected with 3) and, as the central issue in this paper, we will discuss it following in section 3.2.3 in length.

Detailed descriptions and progresses concerning 1) to 3) can be found in review paper by Fahr and Shizgal [1983].

So far collisional exosphere models with nonthermal processes included have been, or at least are expected to be, successful in explaining issues like larger escape flux observed, two-component exosphere [Anderson, 1976] and enrichment of D/H [in Venus, Donahue et al., 1982].

There are two ways of studying a collisional exosphere: the kinetic approach and Monte Carlo method. Discussion about them follows in section 3.2.1 and 3.2.2.

3.2.1 Kinetic Approach

The kinetic approach employs, self-evidently, the kinetic theory that is applicable to describe collisional exosphere. The central issue of this method is to determine the temporal and spatial change of the distribution function of exospheric particles by solving the governing equation—the well-known Boltzmann equation, that is,

$$\frac{\partial}{\partial t} f_{\alpha} + (\bar{v}_{\alpha} \cdot \nabla_r) f_{\alpha} + \left(\frac{\bar{F}_{\alpha}}{m_{\alpha}} \cdot \nabla_v \right) f_{\alpha} = \left(\frac{\partial}{\partial t} f_{\alpha} \right)_C + \left(\frac{\partial}{\partial t} f_{\alpha} \right)_R \quad (3.2.1)$$

where the terms on the left hand side (LHS) of the equation depict the evolution of distribution function (f_{α}) of component α in 6-dimensional (\vec{r}, \vec{v}) phase space under the action of external force \bar{F}_{α} . The ∇_r and ∇_v in LHS are spatial and velocity gradient operators and m_{α} is the mass. The first term of the right hand side (RHS) is the sum of all kinds of collisions and the second term is the sum of all radiative interactions. It is the various RHS terms that make it possible for us to deal with different kinds of problems. The simplest case is the collisionless exosphere with RHS being zero. For collisional exosphere things are getting more complicated and we discuss the two terms one by one in the following.

According to the different collisions being taken into account, the first term in RHS can be divided into several parts. Firstly, when considering the elastic collisions between constituent α and β (β can either be α itself or any other particle), we have,

$$\left(\frac{\partial}{\partial t} f_{\alpha}\right)_C^E = \sum_{\beta} \iint [f_{\alpha}(\bar{v}_{\alpha}') f_{\beta}(\bar{v}_{\beta}') - f_{\alpha}(\bar{v}_{\alpha}) f_{\beta}(\bar{v}_{\beta})] \sigma_{\alpha\beta}(v_{\alpha\beta}, \Omega) \bar{v}_{\alpha\beta} d\Omega d\bar{v}_{\beta} \quad (3.2.2)$$

here $\bar{v}_{\alpha\beta} = \bar{v}_{\beta} - \bar{v}_{\alpha}$ is the relative velocity of particles, Ω is the scattering solid angle, and $\sigma_{\alpha\beta}(v_{\alpha\beta}, \Omega)$ is the differential elastic cross section. The prime in the gain term denotes parameters before an inverse collision. Similarly when the charge exchange (CE), like $\alpha^+ + \beta \rightarrow \alpha + \beta^+$, is included one more gain term should be added to $\left(\frac{\partial}{\partial t} f_{\alpha}\right)_C$

$$\left(\frac{\partial}{\partial t} f_{\alpha}\right)_C^{CE} = \sum_{\beta} \iint f_{\alpha^+}(\bar{v}_{\alpha^+}) f_{\beta}(\bar{v}_{\beta}) \sigma_{\alpha^+\beta}(v_{\alpha^+\beta}, \Omega) \bar{v}_{\alpha^+\beta} d\Omega d\bar{v}_{\beta} \quad (3.2.3)$$

while for $\beta^+ + \alpha \rightarrow \beta + \alpha^+$ we have a loss term

$$\left(\frac{\partial}{\partial t} f_{\alpha}\right)_C^{CE} = - \sum_{\beta} \iint f_{\alpha}(\bar{v}_{\alpha}) f_{\beta^+}(\bar{v}_{\beta^+}) \sigma_{\alpha\beta^+}(v_{\alpha\beta^+}, \Omega) \bar{v}_{\alpha\beta^+} d\Omega d\bar{v}_{\beta^+} \quad (3.2.4)$$

[Shizgal and Arkos, 1996], and if $\alpha = \beta$ or reversible CE reaction then both (3.2.3) and

(3.2.4) should be included in $\left(\frac{\partial}{\partial t} f_{\alpha}\right)_C^{CE}$ [Fahr and Shizgal, 1983]. For special CE cases

like $H + H^+ \rightarrow H^+ + H^*$ which is elastic or $O + H^+ \rightarrow O^+ + H^*$ which is quasi-elastic

$\left(\frac{\partial}{\partial t} f_{\alpha}\right)_C^{CE}$ degenerates into the same form as in (3.2.2) [Shizgal and Lindenfeld, 1982].

Finally, $\left(\frac{\partial}{\partial t} f_{\alpha}\right)_C^{IE}$, the collision term of other inelastic or chemical reactive collision

processes, can be obtained similarly as that of CE. It's evident that when we face

different problems the exact form of $\left(\frac{\partial}{\partial t} f_{\alpha}\right)_C$ may vary.

The second term of RHS of (3.2.1) embraces various photoprocesses, such as resonant absorption, spontaneous and induced radiation, photodissociation, photoionization, Lyman scattering, and etc. Detailed theory about those photoprocesses could be found in the book of Marov and et al. [1997]. In our model, we are concerned about photoionization and Lyman scattering only, and both terms can be approximated to be like

$$\left(\frac{\partial}{\partial t} f_{\alpha}\right)_R^P = -\nu_P f_{\alpha}(v_{\alpha}) \quad (3.2.5)$$

and

$$\left(\frac{\partial}{\partial t} f_{\alpha}\right)_R^L = \nu_L \left(\int f_{\alpha}(\bar{v}_{\alpha} + \hat{\Omega} \cdot \bar{v}_0) d\hat{\Omega} - f_{\alpha}(\bar{v}_{\alpha}) \right) \quad (3.2.6)$$

where ν_P and ν_L are photoionization and Lyman scattering frequency, respectively, with assumption that both photoionization and Lyman scattering cross sections are independent of particle's velocity.

By applying equation (3.2.1) to every atmospheric component, we have a coupled equation group governing the behavior of exosphere particles. However, seeking analytic general solution of such nonlinear differential equation group is formidable. Therefore, as stated above, attempts of pursuing an analytic solution in some very simplified cases or numerical solution under properly set boundary conditions and other assumption have been made [like, for example, Hays and Liu, 1965; Lindenfeld and Shizfal, 1979; and many more]. Obviously, there are still many problems are beyond the abilities of kinetic approach and then under such circumstances people turn to the Monte Carlo method.

3.2.2 Monte Carlo Method

The Monte Carlo method is introduced to this field as an alternative way to solve the Boltzmann equation as stated previously. Fahr and Shizgal [1983] have pointed out that “the results of Monte Carlo calculations, properly performed, are equivalent to solutions of the Boltzmann equation”. This conclusion is drawn not only by comparing results from two approaches but also from work done by Nanbu [1980a, b].

Although models vary in details for different problems, a rough scheme of the calculation based on the Monte Carlo method can be described here [Sahr and Shizgal, 1983]. First, a source particle (e.g., atomic hydrogen) is released from the exobase (or lower boundary of the calculation domain) with randomly chosen velocity from a specified distribution function. Then this particle travels along under the influence of external force field until collision with a target particle (e.g., O) occurs. Here the position of the collision and other parameter (velocity) of the target particles are controlled by some random numbers, and velocity of the source particle after the collision is determined by the collisional physics. If allowed, the source particle keeps on moving with new velocity and above procedure repeats until the life of this source particle is terminated either when it reaches the upper boundary with velocity larger than v_{esc} or it is removed by chemical or photolytic reactions (e.g., H turns into H^+ by charge exchange or photoionization), then that source particle is replaced by a new one starting from the lower boundary again. In this way amounts of source particles are injected into the calculation region one by one and movement of each of them is audited and accumulate by codes. This accumulation doesn't stop until the number of injected particles is large enough to reach an equilibrium status. Finally we say the distribution function is obtained so that the Boltzmann equation is “solved”.

Choosing Monte Carlo methods to study exospheric problem started in 1960's, when the basic techniques were introduced by Lew and Venkatesware [1965] and Liwshitz and Singer [1966]. This method was accepted at once due to its outstanding applicability to various problems and the only constriction on its ability to get solution to Boltzmann equation in whatever complicated cases is the speed of computer. Since then many workers have contributed to the development, amendment and completeness of this method [Brinkmann, 1970; Nanbu, 1980a, b]. So far based on this method many models have been constructed and successfully described or predicted many exospheric phenomena [Chamberlain and Smith, 1971; Hodges, 1994]. Likewise, we choose Monte Carlo method in this dissertation and details will be discussed in section 5.

3.2.3 Aspects Affecting Planetary Exosphere

Before we move on to the next section, in order to give a complete physics picture, it's valuable to make a brief review of the major physical factors affecting the structure and evolution of planetary exosphere. It should be noted that not all of them related to collision and more comments and detailed discussion can be found in the review papers by Fahr and Shizgal [1983], Hunten [1990] and Shizgal and Arkos [1996].

- 1) Planetary rotation. The rotation of a planet can enhance the density at equator comparing to polar region, and effect of rotation is more prominent to heavier components [Hagenbuch and Hartle, 1969]. For example, the rotation of the earth produces the density ratios between equator and polar at $y = 2$ of 1.016, 1.151, and 1.887 for hydrogen, helium and oxygen, respectively [Fahr and Shizgal, 1983], as indicates that rotation has minor effect on hydrogen exosphere.

- 2) Non-uniformed exobase distribution. Many authors have studied the effects of the non-uniformed exobase temperature and density distribution leading to “lateral flow”, which tends to remove or “balance” the unevenness [McAfee, 1967; Vidla-Madjar and Bertaus, 1972]. One very useful result given by Hodges and Johnson [1968] is that the equilibrium distribution of atomic concentration at the exobase tends to $\propto T^{-5/2}$ approximately.
- 3) Solar radiation. In considering the effects of sunlight, generally we are concerned about two things in the optically-thin exosphere case: one is the Lyman scattering, which can change the movement of individual particle in the gravity field; the other is photoionization which, combined with solar wind EM field, can remove exospheric particle from the planet directly.
- 4) Solar wind. Exospheric components can charge exchange with solar wind protons or be ionized by solar wind electron impact. Although the interaction with solar wind has been considered to be a minor role for the Earth’s exosphere [Fahr and Shizgal, 1983], circumstances are different in the cases of Venus and Mars, where owing to the absence of a significant planetary magnetic field, solar wind can penetrate to a fairly low altitude and interact with the bulk planetary exosphere directly. This dissertation is mainly dedicated to determining quantitatively how this could lead to changes in the Martian exosphere.
- 5) Ionosphere and Plasmasphere. For example, coupling with the plasmasphere and ionosphere is an important characteristic of Earth’s exosphere [Hodges, 1994], and charge exchange between ionosphere and exosphere is the main source of the hot oxygen exosphere on both Venus and Mars.

- 6) Solid exobase. This is not a universal factor affecting all exospheres. Only for extremely tenuous exospheres that, like those of Moon and Mercury, have the exobase coincidence with the planetary surface, does the interaction between planetary surface and exosphere crucial play an important role [Curtis and Hartle, 1978].

Among the major factors affecting exospheres listed above, items 1) and 2) are applicable to both collisional and collisionless models and others can happen in collisional models only. In different cases each factor has a different role and due to the limited computation resources, generally different model focuses on only one or several of them.

Since frequently it is difficult to determine the relevant weight of the above factors theoretically and in simulation results must finally match data, observation is still the first source of information about the exosphere. Next, we give a very brief introduction to observations.

3.3. Exosphere Observation

Although a complete discussion of the exosphere observations is beyond the scope of this paper, a brief introduction is valuable for both theoretical and modeling efforts.

Before the space age, little was known about the upper terrestrial atmosphere except for some scattered data obtained from spectrographic observations of polar auroras at ground level or from measurements with instruments on board sounding rockets, which, however, can barely reach altitudes higher than 200 km. The determination of the exospheric physical conditions has really become possible with the

launching of the first artificial satellites. Indeed, the first and reliable method to determine the atmospheric density at heights above 150 km was based on the analysis of satellite's orbital variations due to the air drag. Exospheric density at heights near the perigee of the orbits (where air density is the most important) can be derived by this method. The same method is applicable to other planets, like Mars [Tracadas, 1999], too.

Presently, according to the platforms on which the measurement is carried out, observation methods can be divided into two groups: satellite-based and ground-based. Change of observation platform leads to change of observation approach and emphasis. The observation can also be classified into two groups in another way: in-situ and remote sensing, which we introduce next and provide descriptions on some instruments.

In-situ measurements use instruments located inside the region of interest and are generally carried out onboard satellites. The mass spectrometer is a useful onboard instrument to measure directly both composition and temperature of exospheric neutral/ionized species. For instance, one such kind of instrument, a neutral mass spectrometer, has been installed on Nozomi (Hope) which unfortunately just lost communications and, an energetic neutral atoms analyzer, will be installed on the Mars Express which is planned to be launched in 2003. Another kind of instrument is the energetic neutral particle detector, which can measure the distribution of neutral particles with very high energy (as are generally produced by charge exchange with high temperature plasma and thought to play an important role in planetary evolution) in the exosphere. One such device (ASPERA) is onboard Mars Express, too. Remote sensing instruments are located outside of the measured region. Such instruments generally measure either the absorption of the light by the exosphere or the emission from the

exosphere itself. For example, combined with radiative transfer theory, measurement of the occulted light intensities and polarization allows deduction of the large-scale exospheric density and temperature profiles. For the Mars experiments, this method can be carried out only onboard the satellite, which is located in and outside of planetary exosphere, such as Mariner 6. Measurements of total intensity, absorption of light by a hydrogen (or other gases) cell, Lyman α intensity, Balmer α intensity are examples of this category, too. Another remote sensing instrument is the incoherent scattering radar, generally ground-based, which can measure the temperature of the exosphere.

The importance of those types of measurements is that the combination of observations in a variety of observing wavelengths and directions and altitudes allows a much more complete set of characterizations of the upper atmosphere than any single ground-based (or even in-situ) measurement can possibly provide.

3.4 Martian Atmosphere and Exosphere

3.4.1 Current Knowledge of the Martian Atmosphere and Exosphere

Since the Soviets first began the mankind's journey to Mars by launching two "Marsnik" crafts in 1960, tens of spacecrafts have attempted to reach Mars and, unfortunately, less than half of them succeeded in "hitting" the target and even fewer finally finished their experiments to provide valuable results. Here we give a brief discussion of the relevant atmosphere relevant observations, and a summary of all Martian missions is given in the table in appendix.

It took more than 30 years for people to establish a rough picture of the Martian atmosphere. In 1965, Mariner 4, the first probe flying-by Mars with a closest approach distance $\sim 10000\text{km}$, measured the Martian atmosphere ground level pressure to be about

5mb by radio occultation experiment. Such low pressure indicated the Martian atmosphere was much thinner than predicted before (10~80mb) so that liquid water was unlikely to exist on Mars. Four years later, Mariner 6 and 7 flew by Mars again and confirmed the low pressure of Martian atmosphere. Furthermore, the ultraviolet spectrometer (UVS) telescope onboard Mariner 6 detected a cloud of hydrogen atoms extending 20,000km above the Martian surface. This is the first indication of the existence of the Martian exosphere. Additionally the airglow spectra obtained by UVS showed the atmosphere was almost 100% carbon dioxide, which was bad news for people hoping for settlements on Mars, and the upper atmosphere temperature is cold, only 350K [Barth, 1984]. The existence of very tenuous water vapor was first discovered by Mariner 9, Mars 2 and Mars 3 almost simultaneously in 1971 and then confirmed by Mars 5 two years later [Leverington, 2000]. It was Mars 6 that obtained the first in situ measurements of the Martian atmosphere during its entry [Kerzhanovich, 1977]. Then came the prolific Viking program. This program included Viking 1 and Viking 2, each of which had an orbiter and lander. In 1975, two landers successfully descended to the Martian surface and the atmosphere structure experiment (ASE) onboard for the first time provided high vertical resolution and accuracy temperature, pressure and density in-situ measurement from surface to 120km, simultaneously the upper atmosphere mass spectrometer (UAMS) extended measurements range up to 200km [Seiff and Kirk, 1977]. All in all, results from the Viking program increased our understanding of Mars greatly. In the 1980's, no other probe but Phobos2 returned to Mars. Although Phobos2 operated only several weeks so that limited amount of data was obtained, the Automatic Space Plasma Experiment with a Rotating Analyzer (ASPERA) onboard Phobos2 detected

ionospheric ion outflow [Lundin et al., 1990], which implied that the global magnetic field on Mars was so weak that solar wind could penetrate deep and interact with the atmosphere/ionosphere directly. It meant the interaction between solar wind and Mars was more Venus and comet-like. The US went back to Mars with Pathfinder which landed on Mars in 1997. This time the atmospheric structure investigation (ASI) onboard spanned the atmosphere range 161-8.9km and these results combined with those from previous spacecrafts provided a more accurate picture of the Martian atmosphere changing with season and spatial location. Currently, Mars Global Surveyor is circling around Mars and the aerobraking effects have been employed to deduce characteristics of the Martian exosphere [[Tracadas, 1999]. In the near future, Mars Express is expected to provide us with more knowledge of the Martian atmosphere by the atmospheric instruments onboard.

Our knowledge of the current Martian atmosphere can be summarized as follows. It is composed primarily of carbon dioxide (95.3%) with a small amount of nitrogen (2.7%), argon (1.6%), and lesser constituents including oxygen (0.13%), carbon monoxide (0.07%), and water vapor whose amount changes significantly seasonally and planet-wide (~0.03%). Trace constituents are neon (2.5ppm), krypton (0.3ppm), etc. Surface atmospheric pressure is as low as ~6mb and varies with season and topography. Surface temperature is also low with mean 220K and varies with time of day, season and location on the planet from minimum near 147K in polar regions to maximum around 300K near the subsolar point at perihelion [Barth et al., 1992]. The temperature and density profiles are available in papers by Seiff and Kirk [1977] and Magglhaes et al. [1999].

The upper atmosphere and exosphere with which we are concerned mostly have little information available. As we stated above, the only in-situ measurements carried out by Vikings and Pathfinders covers altitude range about 120-200 km. This part of the upper atmosphere shows large variations of temperature ($\sim 150\text{K}$) and the average is below 200K . CO_2 dominates up to 200km and then atomic O takes over until very high altitude. As we know, the Martian exosphere is dominated by H as well as O and, without the protection of a planetary magnetic field, is directly exposed to the solar wind. Lyman- α airglow measurements indicate the density of Hydrogen in the dayside is of order of $3 \times 10^4 \text{ cm}^{-3}$ and temperature 350K at an altitude of 250km [Anderson and Hord, 1971]. Other characteristics of Martian exosphere are acquired by model research only. For instance, analogous to the case of Venus, for which we know a hot-oxygen component is caused by the dissociative recombination of the ionosphere, as been observed by the Pioneer Venus Orbiter (PVO), the existence of the same hot-oxygen population has been predicted [McElory, 1972; Wallis, 1978] and simulated by the two stream model [Nagy and Cravens, 1988] or Monte Carlo models [Ip, 1988, 1990; Lammer and Bauer, 1991]. In addition, while on Venus the hot-hydrogen exosphere has been observed [Anderson, 1976] by Mariner 5 and explained by charge exchange [Hodges and Tinsley, 1981], no Martian hot-hydrogen exosphere has been observed. On the other hand, although much work have been done on the interaction between the solar wind and the exosphere [Tanaka, 1995; Luhmann and Kozyra, 1991], most of the models focus on the O exosphere and the charge exchange between solar wind and Martian H exosphere has never been studied quantitatively. Although a detailed review about the Martian exosphere is lacking, some limited but helpful descriptions and discussions have

appeared [Hunten, 1990; Luhmann, 1991;Luhmann and Bauer, 1992; Shizgal and Arkos, 1996].

3.4.2 Theoretical Collisionless Martian Exosphere

In order to set up a criteria to which our later computation in section 5.2 can be compared, we make a theoretical calculation based on the collisionless theory. This calculation shares the original model in Aamodt and Case [1962], which--like what we have presented in section 3.1 already--assumes the Maxwellian distribution on critical boundary and then applies the collisionless kinetic theory to obtain distribution function of any point by which macroscopic parameters can be calculated, and extends from density distribution to flux and temperature distributions.

Next let us see the results obtained. First comes the density profile

$$n_{Total,+S} = \frac{n_c}{2} \exp[\alpha(1 - \frac{1}{y})] \cdot \Phi_{Total,+S} \quad (3.4.1)$$

where $\alpha(r) = \frac{GM_{Mars}m}{kT_c r}$ and parameters with subscript ‘c’ have values at the critical level;

y has the same definition as before, that is $y(r) = r_c / r$; Φ is function of r and we take it out to save the formula length since it’s a factor being used frequently in following

$$\Phi_{Total,+S} = \{1 + \phi(\sqrt{\alpha}) - \sqrt{1-y}^2 \exp(-\frac{\alpha y}{1+y}) [1 \pm \phi(\sqrt{\frac{\alpha}{1+y}})] + \sqrt{\frac{4\alpha}{\pi}} e^{-\alpha} [\pm \sqrt{1-y} - 1]\} \quad (3.4.2)$$

where $\phi(x) = \frac{2}{\sqrt{\pi}} \int_0^x e^{-t^2} (-t^2) dt$ is the error function; and all other symbols have their

usual meaning. As you may have noticed, both n and Φ in (3.4.1) and (3.4.2) have two subscripts. The one “Total” means that the calculation includes particles in both ballistic and escaping categories and the upper sign of “ \pm ” (or “ \mp ” in late equations) before some terms in the right hand of equation applies, while the other “+S” means the

calculation includes the “Total” part plus contribution from satellite category and the lower sign applies. The reason the satellite component is included in the calculation is that we want to evaluate the role from this part’s contribution. Both (3.4.1) and (3.4.2) are consistent with the equation (19) in Aamodt and Case [1962] except that a pair of parentheses are missed by typo there. Calculated density profiles are plotted in figure 3.4. Afterwards, the bulk speed in radial direction of the flux is given by

$$\langle V_r \rangle_{Total,+S} = \frac{\langle nV_r \rangle_{Total,+S}}{n_{Total,+S}} = \frac{\sqrt{\frac{2kT}{m}} \frac{e^{-\alpha}}{\sqrt{\pi}} [x(x+\alpha)]}{\Phi_{Total,+S}} \quad (3.4.3)$$

where the inclusion of the satellite component can obviously decrease the increase of speed and make it finally constant (as shown in figure 3.5). Next two equations give out the averaged kinetic temperature component in horizontal and radial direction,

$$\begin{aligned} T_{Total,+S}^h = T_c \{ & 1 - \frac{2e^{-\alpha}}{3\sqrt{\pi}} \alpha^{\frac{1}{2}} (2\alpha + 3) + f(\sqrt{\alpha}) \\ & - e^{-\frac{\alpha x}{1+x}} [(1-x^2)^{1/2} - \frac{(1-x^2)^{3/2}}{3} I(\frac{3}{2}(1 \pm f(\sqrt{\frac{\alpha}{1+x}}))] \\ & \mp \frac{e^{-\frac{\alpha}{1+x}}}{\sqrt{\pi}} (2(\frac{\alpha}{1+x})^{\frac{3}{2}} + 3(\frac{\alpha}{1+x})^{\frac{1}{2}}) I \\ & - e^{-\frac{\alpha x}{1+x}} [\alpha x \sqrt{\frac{1-x}{1+x}} I(1 \pm f(\sqrt{\frac{\alpha}{1+x}})) \mp \frac{2}{\sqrt{\pi}} \sqrt{\frac{\alpha}{1+x}} e^{-\frac{x}{1+x}}]] / \Phi_{Total,+S} \end{aligned} \quad (3.4.4)$$

$$\begin{aligned} T_{Total,+S}^r = T_c \{ & 1 - \frac{e^{-\alpha}}{\sqrt{\pi}} \alpha^{\frac{1}{2}} (\frac{4}{3}\alpha + 2) + \phi(\sqrt{\alpha}) \\ & - e^{-\frac{\alpha x}{1+x}} (1-x^2)^{3/2} [(1 \pm \phi(\sqrt{\frac{\alpha}{1+x}})) \mp \frac{e^{-\frac{\alpha}{1+x}}}{\sqrt{\pi}} (\frac{4}{3}(\frac{\alpha}{1+x})^{\frac{3}{2}} + 2(\frac{\alpha}{1+x})^{\frac{1}{2}})] \} / \Phi_{Total,+S} \\ & - T_c \{ \sqrt{\frac{2}{\pi}} e^{-\alpha} [x(x+\alpha)] / \Phi_{Total,+S} \}^2 \end{aligned} \quad (3.4.5)$$

and then the final averaged temperature can be obtained by

$$T = \frac{2T^h + T^r}{3} \quad (3.4.6)$$

In figures 3.6 we visualize the output from above three equations. It's obvious that including satellite particles can greatly decrease the inhomogeneity in the temperature profiles.

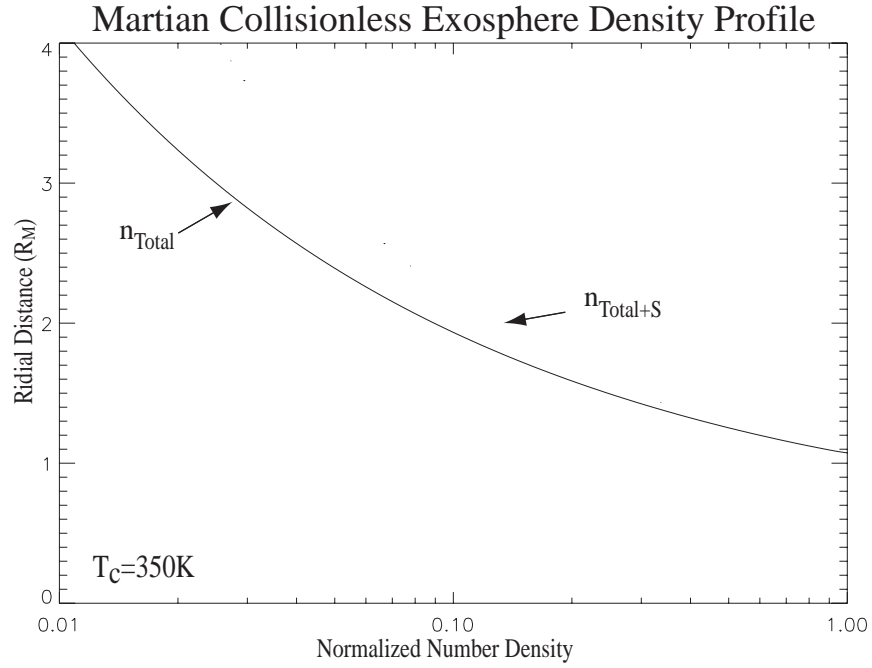


Figure 3.4 Calculated normalized Martian collisionless exosphere density profiles (with and without satellite component) with exobase temperature being 350K.

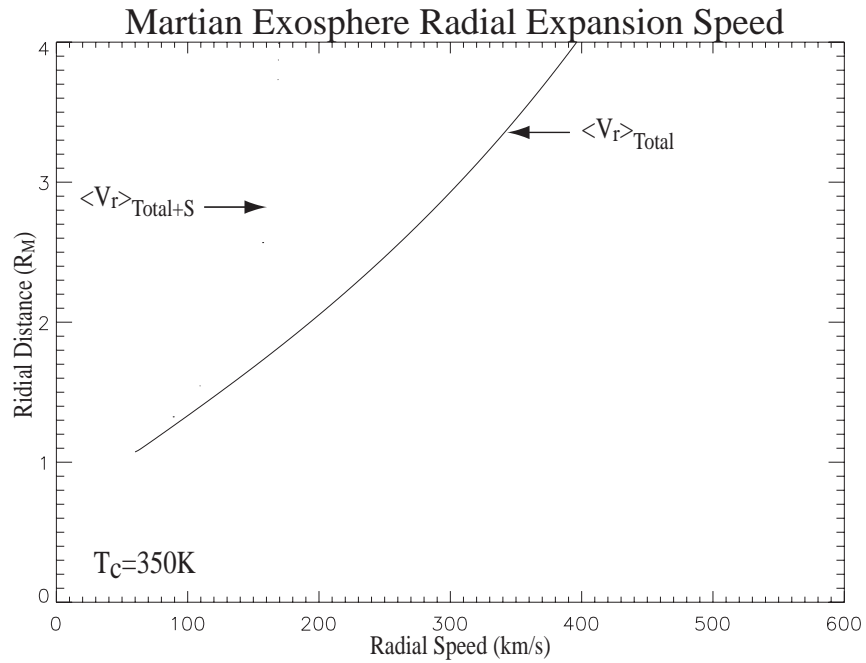


Figure 3.5 Calculated upward bulk speed of the Martian collisionless exosphere (with and without satellite component) with exobase temperature being 350K. Note the inclusion of satellite particles makes the speed approach a constant more quickly.

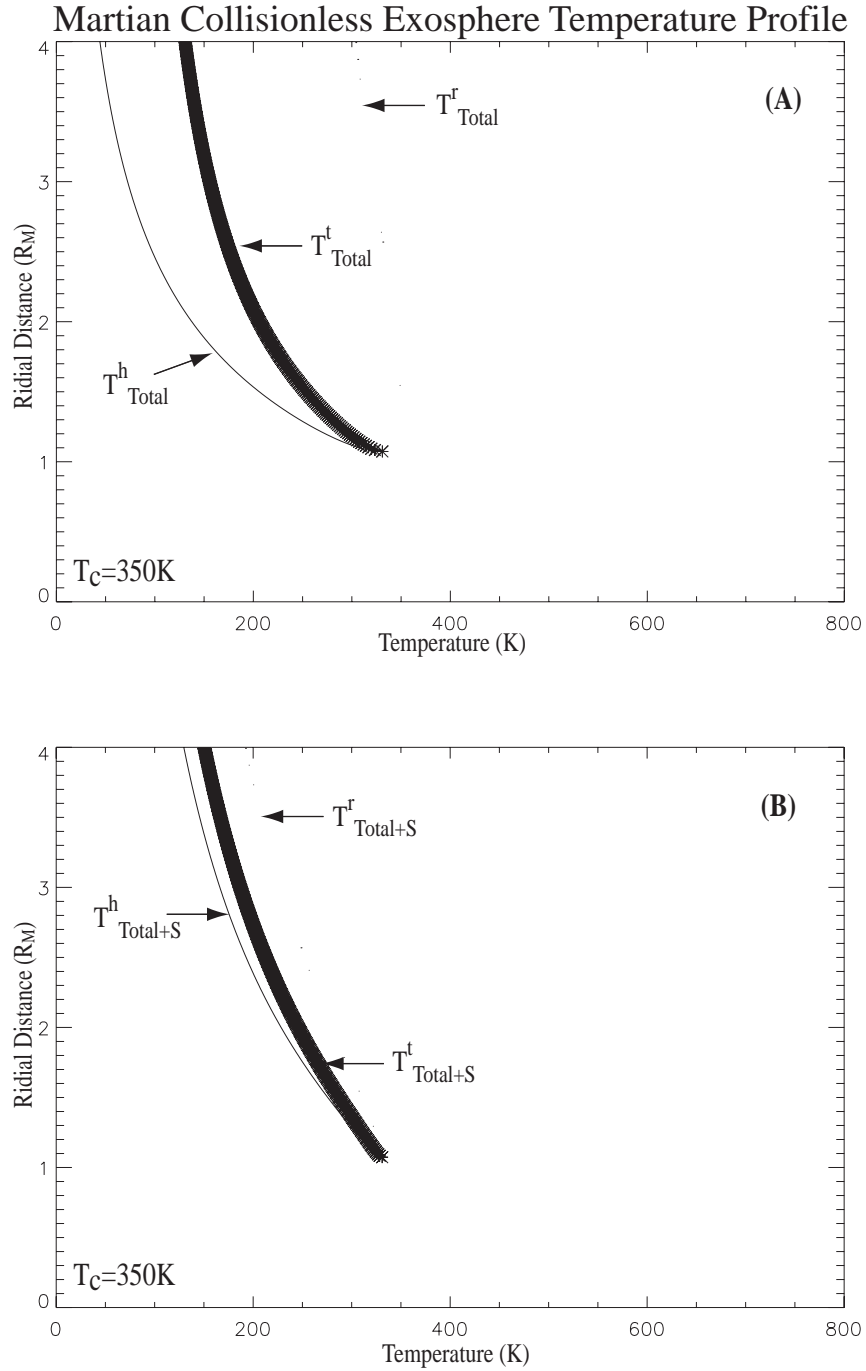


Figure 3.6 Calculated Martian collisionless exosphere temperature profiles (of horizontal and radial components and total temperature) with exobase temperature being 350K. (A) without satellite particle. (B) with satellite particles.

4. Solar Wind Charge Exchange with Martian Exosphere

As we have stated in section 2.3, due to the weak planetary magnetic field, solar wind particles can penetrate deeply into the Martian upper atmosphere and alter the conditions of the exosphere, which in turn strongly affects the shocked solar wind in the magnetosheath. Interactions occurring there include charge exchange, electron impact ionization, ion pick-up, etc. Among those processes charge exchange stands out since it can not only produce the “new” current system which can help the ionosphere to divert solar wind flow but also create an energetic neutral particle group which changes the exosphere greatly. So in this dissertation, we focus our study on the effects of charge exchange on both the solar wind and exosphere.

To achieve this goal, theoretically we need to consider the solar wind and atmosphere simultaneously. Actually some MHD models [e.g., Tanaka, 1995; Murawski and Steinolfson, 1996] emphasizing on solar wind as well as Monte Carlo model on the exosphere [Luhmann and Kozyra, 1991] have been constructed to study other aspects of solar wind/exosphere interaction. Therefore in the similar way, we develop a fluid model of solar wind presented in this section and a Monte Carlo model of the exosphere that will be discussed in next section.

4.1 Magnetic Pileup Boundary Observed by MGS

The magnetic pileup boundary (MPB) is one characteristic of the solar wind flowing around nonmagnetic objects and defined as the boundary marking the beginning of the magnetic field lines piling-up region, which was identified first at comets [Neubauer et al., 1987; Mazelle et al., 1989] and analogous to the plasma mantle observed by Pioneer Venus Orbiter *in situ* at Venus [Spenner et al., 1980] and exists on

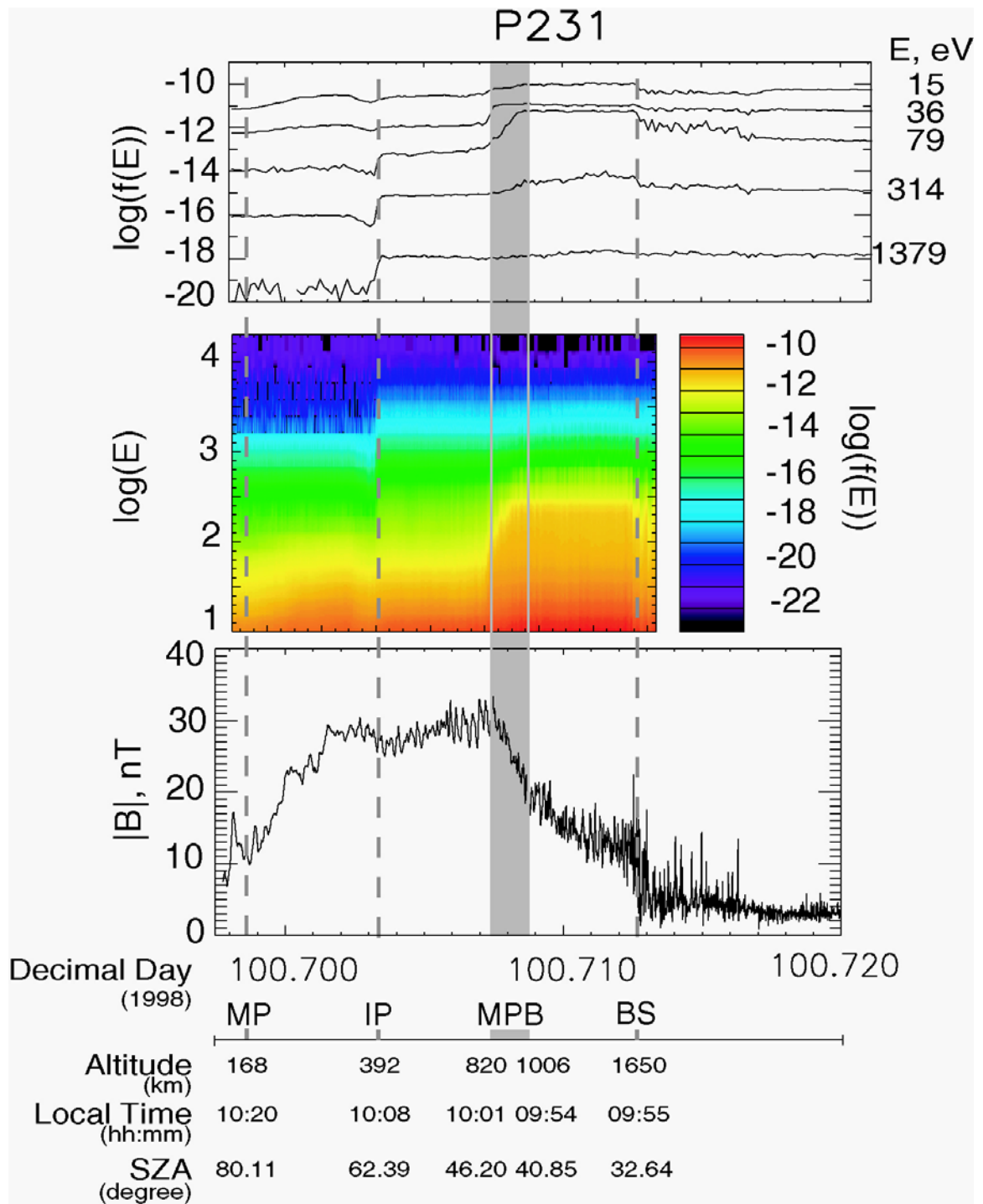


Figure 4.1 (Top and middle) Electron distribution function and (bottom) magnetic field time series data for P231 outbound. Five ER energies are given to the right of traces in top panel. For reference, the locations of the ionospheric main peak (MP), ionosphere (IP), and bow shock (BS) are shown in three extra horizontal axes: altitude, local time, and SZA. The magnetic pileup boundary (MPB) is indicated by the shaded region [Chen et al., 2001].

Mars, too. Then Cloutier et al. [1999] pointed out the existence of the MPB from Pioneer Venus Orbiter data. Unsurprisingly, as an aspect of a Venus-like interaction, the MPB of Mars has already been identified from data of MGS [Acuña et al., 1998; Cloutier et al., 1999] by the characteristics of increase in magnetic field, decrease in electron fluxes (with energy range 15~1380eV) and decrease in magnetic field fluctuations with decreasing altitude.

One typical MPB observed, the outbound pass P231, is shown in figure 4.1 in which detailed MAG/ER data are plotted [Chen et al., 2001]. In that plot the boxed off region is the MPB whose altitude is given for reference. Generally, two features mark the MPB in MAG data: the first is the steep increase of the field strength, which is clearly seen in P231 outbound where the field rises from ~15nT to over 30nT during the time from 100.709 to 100.707 (note we follow the P231 data from right to left, for backward in time corresponds to moving deeper inside); secondly, in the normal case, with decreasing altitude, the crossing of the MPB usually coincides with the attenuation of the waves in the magnetic field. ER data also show us that the electron density declines as the electron distribution evolves in a specified way.

The magnitude of magnetic field in Martian MPB observed by MGS increases so precipitously that common solar wind-ionosphere models do not predict it. For example, in their 3D multi-fluid MHD model, Liu et al. [1999] produce a magnetic increase boundary not at the MPB location but much closer to the Mars surface. Similarly, from the results (e.g., figure 1) of another 3D two-component MHD model presented by Tanaka et al. [1997], we are not able to discern evidences of MPB. Other hybrid models [e.g., Stephen et al., 1991] concentrate on showing the lack of symmetry and make no

predictions of the existence of a MPB. Additionally, traditional gas-dynamic models [e.g., Riedler et al.] cannot reproduce the steep increase of magnetic field at the observed location of the MPB, either. Obviously, some other factor should be incorporated and we will show that charge exchange is a likely mechanism.

4.2 Underlying Physical Picture

The idea that charge exchange may play a role is initially invoked by work of Crider et al. [2000]. In that paper the behavior of electrons in Mars' MPB is reproduced successfully by constructing a model in which electron impact ionizes neutral atmospheric atoms, which strongly implies the involvement of the exosphere in the formation of the MPB.

Besides, at least one observed feature can provide us with a crucial clue to explain the formation of the MPB. That is the partition of pressures. In the conservation of the solar wind's momentum flux, change of the percentages for the three pressure terms (dynamic, thermal and magnetic) strongly implies that nearly all the increase in the thermal pressure caused by shock compression must be lost to or transferred to magnetic pressure at the MPB. The key role played by the neutral exosphere in the MPB demonstrated by Crider et al. [2000] suggests a plausible scenario involved in the steep magnetic field build up of the MPB: after the solar wind protons are thermalized by the bow shock ($\sim 10^5 K$ pre-shock and $\sim 10^6 K$ post-shock), they charge exchange with the H and O in the Martian exosphere and relatively cold H^+ and O^+ are produced. In this way, the solar wind loses its thermal pressure. From the momentum equation, we have

$$\nabla \cdot [\rho \vec{v} \vec{v} + \vec{I}(P + \frac{B^2}{2\mu_0})] = G - L \quad (4.2.1)$$

where terms in the right hand side are both zero for the case without charge exchange while for the case with charge exchange, we have a loss term $L = -\sum_i m\bar{v} \nu_i$ in which ν_i is the charge exchange reaction rate. Since this loss term is actually ignorable, the total pressure with and without charge exchange should have the same value approximately. And because in stagnation region the speed of flow is small, to conserve the total pressure, the magnetic field has to increase to compensate, and the increment of the magnetic pressure should be equal to the loss of thermal pressure at any point. To formulate it, we write

$$(P_0 - P_{CE}) = \left(\frac{B_{CE}^2}{2\mu_0} - \frac{B_0^2}{2\mu_0} \right) \quad (4.2.2)$$

in which P and B are the thermal pressure and magnetic field of any point in the flow field, subscripts 0 and CE denote the physical values before and after the CE and μ_0 has the usual meaning. Macroscopically, the loss of thermal pressure by charge exchange produces both a curl in magnetization (hence a magnetization current which increases magnetic field) and a initial drop in total pressure, which must be brought back up to the total solar wind pressure by recompression of the flux tube containing the cooler plasma. Microscopically, charge exchange results in replacement of protons with large diamagnetic moment by protons with small diamagnetic moment, with corresponding increase in field magnitude, and the recompression of the flux tube increases both plasma density and magnetic field.

The role of charge exchange (CE) in the interaction between solar wind and Mars has been mentioned previously [Nagy et al., 1990; Lundin et al., 1990; Breus et al., 1991; Hunten, 1992] as one way the Martian atmosphere being eroded. Some estimations of the

Martian atmospheric loss rate due to CE have been given [Russell, et al., 1983; Luhmann and Bauer, 1992] and also some models have been constructed for more detailed studies [Zhang et al., 1993; Kallio et al., 1997]. It is also worth mentioning that CE has been encapsulated in MHD models to study the solar wind-Venus interaction [i.e., Bauske et al., 1998; Kallio et al., 1998] and they appear successful. However, it is improper to extend their conclusions simply to the Martian case because only CE of oxygen is considered in the above models but the Martian exosphere is dominated by H at least around and beyond the altitude we are concerned presently (refer to the description in section 4.3). Consequently, we assert that the study of the connection between the CE and magnetic field in the Martian case, which we present in this paper, hasn't been previously described.

4.3 Fluid Model of Solar Wind

In this section we develop a model based on CE theory to reproduce the dayside magnetic field observed by the MGS MAG. In this model it is assumed the field pressure increases to compensate for the loss of the solar wind thermal pressure when the charge exchange between the proton and neutral components (mainly H and O) occurs.

To study the role of CE, we set up our model in two steps. First, we constructed flow model I (FMI) which describes the flow in the dayside Martian magnetosphere without CE. From this model, we calculated flow behaviors and fields and compared them with results from other successful models to check model validity. Then, based on FMI, we added the charge exchange reaction in flow model II or FMII. Both of those models are three dimensional, but some parts of them can be simplified to be 2D.

The model calculations rely on several input parameters. First, we implement a neutral density model [Crider et al., 2000a] which is a compilation of the neutral exosphere of Kim et al. [1998] and the low altitude model of Shinigawa & Cravens [1989] (left panel in figure 4.3). Next, we take the CE reaction cross sections for H from the experimental data of Fite et al. [1960] and those for O from the paper of Stebbings et al. [1964] (right panel in figure 4.3). Finally, shapes and locations of the bow shock and the MPB are results from the paper of D. Vignes et al. [2000], and those of ionopause (IP) are from Knudsen et al. [1982] and Crider et al. [2000]. Those boundaries are shown in Figure 4.3-4.6.

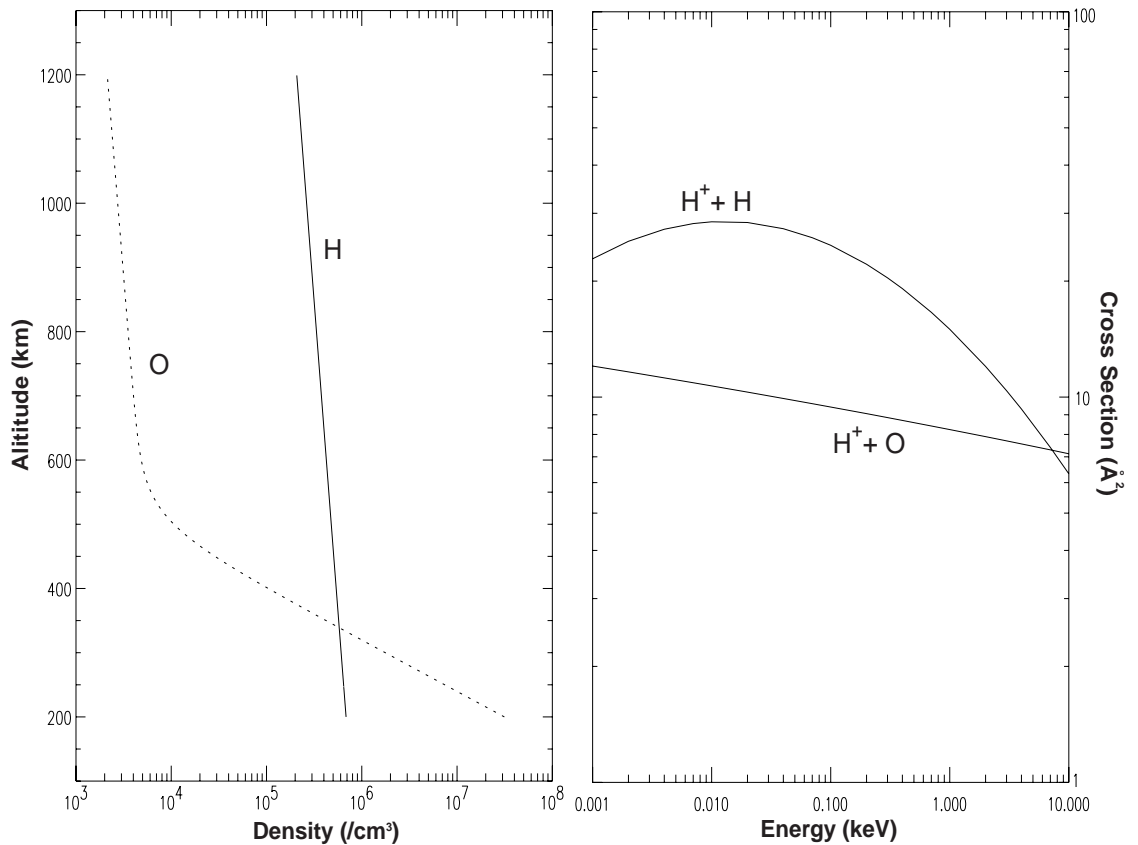


Figure 4.2 (left) Martian H and O exosphere density profiles [Crider et al., 2000a]; (right) Cross sections of charge exchange reactions (data for $\text{H} + \text{H}^+$ are from Fite et al. [1960] and data for $\text{O} + \text{H}^+$ from Stebbings et al. [1964]).

We use Mars-Solar-Ecliptic coordinates here. That is, the x axis points from Mars to the Sun, the y axis is the negative of the revolution velocity direction of Mars and the z-axis forms the right-hand system with x and y.

To build FMI, our first step is to set up a solar wind flow model which is based on the results of Spreiter and Stahara's model (SSM) [1992; 1980; 1970]. First, it should be noted that the SSM is obtained by solving the simplified MHD equations in which the field and flow have been decoupled from the assumption of frozen-in magnetic field. The flow is axisymmetric around the x-axis so that all flow parameters (velocity, temperature, density, etc.) that need computing are in 2D space only. Here we choose the xy plane. Instead of solving the MHD equations, we use the post-shock flow velocity model given by SSM. Moreover, in agreement with Crider et al. [2000], a shear layer is incorporated to reduce the flow speed from the SSM's value to 5km/s in a layer 50-100km thick at the lower altitude boundary; this accounts for the fact that Mars is not an ideal obstacle and that the velocity must not exceed the escape speed at the ionopause. Knowing the velocity field, we could calculate the geometry of any flow line easily if the starting point is given. Pressure and density can be calculated along each flow line if we solve adiabatic and gasdynamic Bernoulli's equations. Therefore, if we calculate many flow lines, we obtain a "mesh" and can use it to interpolate the flow parameters at any point. Next, to calculate the magnetic field, considering the linearity of the equations describing the field, we only need to calculate the field in a 2D plane for three specified cases although the magnetic field is not axisymmetric generally. The field of any point in the 3D magnetosheath for arbitrary uniform \bar{B}_{sw} (solar wind magnetic field upstream of bow shock, assumed to be spatial uniform in our model) could be obtained by linear

superposition of the field vectors in the 3 planes [Alksne, 1970]. Details of FMI are as follows:

Flow Model I (FMI)

Being a semi-empirical model, FMI is constructed to reproduce the dayside simulation results of Spreiter and Stahara's gasdynamic model. Several parts are included as following:

Boundaries:

Bow shock is a conic function: $r(\theta) = \frac{l}{1 + \varepsilon \cos \theta}$, here r is the distance between the focus (locating on x-axis with $x = x_0$) and point in the bow shock, θ is the angle between x and the vector pointing from focus to the point, l is the semi-latus and ε is the eccentricity. In our model, $\varepsilon = 1.02$, $l = 2.04R_M$ and $x_0 = 0.55R_M$ [Kallio, 1996].

Ionopause is expressed by a polynomia in solar zenith angle (SZA) with coefficients in $\{a_i\}$:

$$\text{For } \text{SZA} > 5^\circ, IP_alt(km) = \sum_{i=0}^8 a_i (\text{SZA})^i$$

$$\text{For } \text{SZA} < 5^\circ, IP_alt(km) = \sum_{i=0}^8 a_i (5)^i, \text{ here } IP_alt \text{ is altitude of ionopause in}$$

unit of kilometer and coefficients $\{a_i\}$ are given like

$$\text{this: } \{390.54, -28.737, 3.7057, 0.20712, 6.0645 \times 10^{-3}, \\ -9.7293 \times 10^{-5}, 8.6282 \times 10^{-7}, -3.9667 \times 10^{-9}, 7.3726 \times 10^{-12}\}$$

Only as a reference, the shape and location of MPB is shown in figures. It's a

conic function, too: $r(\theta) = \frac{l}{1 + \varepsilon \cos \theta}$, here $\varepsilon = 0.94$, $l = 0.83R_M$ and

$x_0 = 0.98R_M$. It should be kept in mind that in our model MPB is the natural result of the CE between solar wind and Martian exosphere.

Flow velocity model:

This “empirical” model (the reason empirical being in quotation marks is that the following analytic velocity model is going to reproduce results from SSM but not any observation data) simulates several features which a realistic velocity model should carry. First is the velocity drop at the bow shock. Being consistent with SSM, the gasdynamic bow shock condition is employed. That is, $\vec{V}_{ps} = (|\vec{V}_{sw}| \cos \Theta, |\vec{V}_{sw}| * f * \sin \Theta)$, where \vec{V}_{ps} and \vec{V}_{sw} are solar wind post- and pre- shock velocities respectively, Θ is angle between \vec{V}_{sw} and bow shock normal, f is the relevant coefficient with $f = \frac{\gamma - 1 + \gamma M^2}{\gamma + 1}$, here γ and M have usual definition. Second, as we note in the text, a shear-layer in which the flow velocity is less than Martian escape velocity is incorporated, and the shape of this layer is given by $r_{sh}(SZA) = r_{ip}(SZA) + c [r_{bs}(SZA) - r_{ip}(SZA)]$, where $r_{sh}(SZA)$, $r_{ip}(SZA)$ and $r_{bs}(SZA)$ are the radial distance from Martian center to the shear-layer, ionopause and bow shock with corresponding solar zenith angle, and c is an coefficient and we choose 0.005 here. Finally, the velocity field in the magnetosheath and shear-layer is given by simulating results from SSM. To do that, we begin with define the velocity magnitude on the shear-layer top:

$V_{shear} = V_{ps} * [1.25 - \cos(SZA/2)]^3$, then the velocity magnitude:

$$V_{mag} = V_{ps} \frac{r - r_{sh}}{r_{bs} - r_{sh}} + V_{sh} \frac{r_{bs} - r}{r_{bs} - r_{sh}} \text{ when } r_{sh} < r < r_{bs}$$

$$V_{mag} = (V_{shear} - V_{esc}) \frac{r - r_{ip}}{r_{sh} - r_{ip}} + V_{esc} \text{ when } r \prec r_{sh}$$

(where r is radial distance from Martian center to field point, V_{esc} is Martian escaper velocity), and velocity direction:

$$\Theta_{flow} = [\Theta_{pbs} - \Theta_{sh}] \frac{r - r_{sh}}{r_{bs} - r_{sh}} + sh_ang, \text{ when } r \succ r_{sh}$$

$$\Theta_{flow} = [\Theta_{sh} - \Theta_{ip}] \frac{r - r_{ip}}{r_{sh} - r_{ip}} + ip_ang, \text{ when } r \prec r_{sh}$$

(where Θ_{flow} , sh_ang and ip_ang are angles from positive \hat{x} to flow velocity, shear-layer tangent and ionopause tangent with the same SZA).

Flow parameters:

After the velocity field is set, the flow parameters (pressure, density and temperature) can be obtained by calculation along an arbitrary flow pipe by assuming the fluid is ideal, adiabatic and Bernoullic.

$$\frac{u + P}{\rho} + \frac{1}{2} V^2 = const.$$

$$\frac{P}{\rho^\gamma} = const.$$

$$P = (\gamma - 1)u, \text{ where we choose } \gamma = \frac{5}{3}.$$

Magnetic field:

With the assumption of frozen-in flux, we could calculate the magnetic field [Spreiter et al., 1980; Kallio, 1996] with arbitrary initial interplanetary magnetic field (IMF). However, considering the linearity of the frozen-in equations ($\nabla \times (\vec{B} \times \vec{V}) = 0$ and $\nabla \bullet \vec{B} = 0$), we only need to calculate 3 specified cases and the field of other cases could simply be obtained by superposition of the 3 cases

[Alksne, 1970]. Obviously, the magnetic field calculated in this model should be divergence free.

The comparison of FMI results with those from SSM can tell us how reliable FMI is. Some calculation results will be given in next section.

Next, by adding charge exchange, we have FMII and could get the new magnetic field by keeping total pressure constant for any point.

Flow Model II (FMII)

Comparing results of SSM and FMI, adjusting the parameters, we could obtain FMI and then move on constructing FMII. To introducing the CE, we need to have Martian exospheric model and CE reaction cross-sections first.

Exosphere model includes oxygen and hydrogen as follows:

Hydrogen: $n_H = n_H^0 \exp(-\frac{z}{H_H})$, with $z = \text{altitude}(km)$ when $z < 8 \cdot 10^4 km$, or

$z = \text{altitude}(km) / 10^3$. Shown in figure 4.2 (left).

Oxygen: $n_o = n_o^0 \exp(-\frac{z}{H_o^0}) + n_o^1 \exp(-\frac{z}{H_o^1})$. Here 0,1 denote nonthermal oxygen

corona and thermal component, respectively. Shown in figure 4.2 (left).

In the above two expressions, densities are in unit of cm^{-3} : $n_H^0 = 8.68 \cdot 10^5 cm^{-3}$,

$n_o^0 = 9.66 \cdot 10^3 cm^{-3}$ and $n_o^1 = 9.99 \cdot 10^9 cm^{-3}$; scale heights in km :

$H_H = 838.8 km$, $H_o^0 = 793.5 km$ and $H_o^1 = 34.7 km$. This model simulates the

Martian exosphere in solar minimum, as is the case of MGS. The reactions with

H_2 and He are not taken into account due to the low cross sections.

CE reaction cross-sections.

$$H^+ + O \rightarrow H + O^+ : Q(A^o)^2 = 13.47 - 0.2 \log_{10} E(eV)$$

$$H^+ + H \rightarrow H + H^+ : Q(A^o)^2 = -0.0785 \log_{10}^2 E(eV) - 0.2965 \log_{10} E(eV) + 1.176$$

, where E is the energy of incoming solar wind ions. Shown in figure 4.2 (right).

Finally, we can calculate the loss of thermal pressure along flow lines. Assuming the initial solar wind proton distribution function is Maxwellian and including only effects of CE collision, the following expression of the distribution function evolution along flow line can be derived from the continuity equation:

$$f_2(E) = f_1(E) \left[\frac{A_1 V_1}{A_2 V_2} - \left(\sum_{i=H,O} n_i \sigma_i(E) * \sqrt{\frac{2E}{m}} dt \right) \frac{(1 + \frac{V_1}{V_2})(1 + \frac{A_1}{A_2} + \sqrt{\frac{A_1}{A_2}})}{6} \right],$$

where subscripts 1 and 2 denote values before and after time interval dt , f is distribution function, V is flow velocity and A is streamline cross section which could be given by FMI. We can see the second term in above square braces would be zero if CE is not included.

After the distribution function is calculated, the pressure after CE is known. According to what we explained in the text, for each point in the field, the loss of thermal pressure can be calculated by comparing result from FMI with that from FMII. To compensate for that loss, the magnetic field has to increase and the MPB is seen to form. Furthermore, it's worthy mention that the newly produced magnetic field should keep being divergence free for the magnetization current will not violate it. Having the coordinates of MGS' trajectory, we can reproduce magnetic field along any orbit and results will given in next section.

Although it's beyond the scope of this paper, we'd like to give a brief comment to show why the SSM is chosen to be the reference of FMI. Various models have been constructed to simulate the interaction between the solar wind and nonmagnetic objects. (Especially, MHD self-consistent models have been developed recently and most major characteristics of the magnetosphere have been reproduced [i.e., Tanaka et al., 1997; Bauske et al., 1998; Kallio et al., 1998; Liu et al., 1999].) However, SSM has several advantages fitting our needs: firstly, as a model carrying a long history, SSM provides us with results that are wide-spread, easy-available and well-tested. That allows us to reproduce SSM's results easily. Secondly, the magnetic field in SSM, assumed to be frozen-in and then decoupled, could be calculated independently for arbitrary initial input. That point is crucial for case studies with limited computation resources. From this perspective, paradoxically, self-consistent MHD models are too sophisticated for us to isolate and study the connection between CE and magnetic field. Finally, and most importantly, in the Martian case, the validity of SSM also has been proven at least in region upstream of the MPB [Crider et al., 2000b]. That gives our research a robust basis.

Before going further, a few assumptions should be clarified here. Firstly, it is assumed that interactions of hot post-shock protons are much more important to pressure loss than the electrons' interactions because electrons are much more weakly shock-heated and their contribution to thermal pressure is very small. Therefore in our model, we simply ignore the pressure effects of the solar wind electrons. Secondly, this model is a first-order simulation, in which we assume that the CE won't change the geometry of each flow line, especially at the beginning. Then the effect of the CE is assumed to be confined in the region from the bow shock to the ionopause and no any other ionization

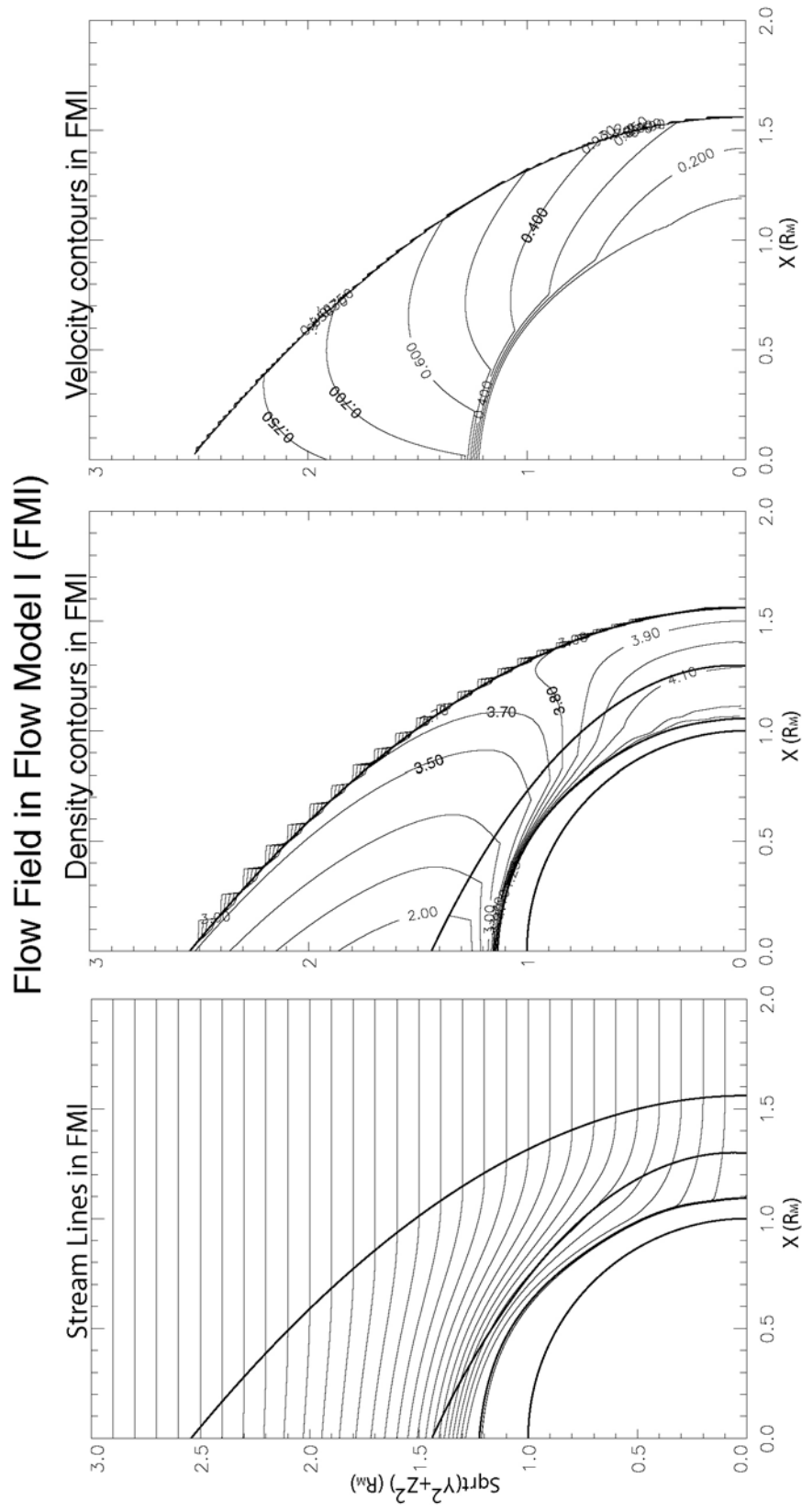
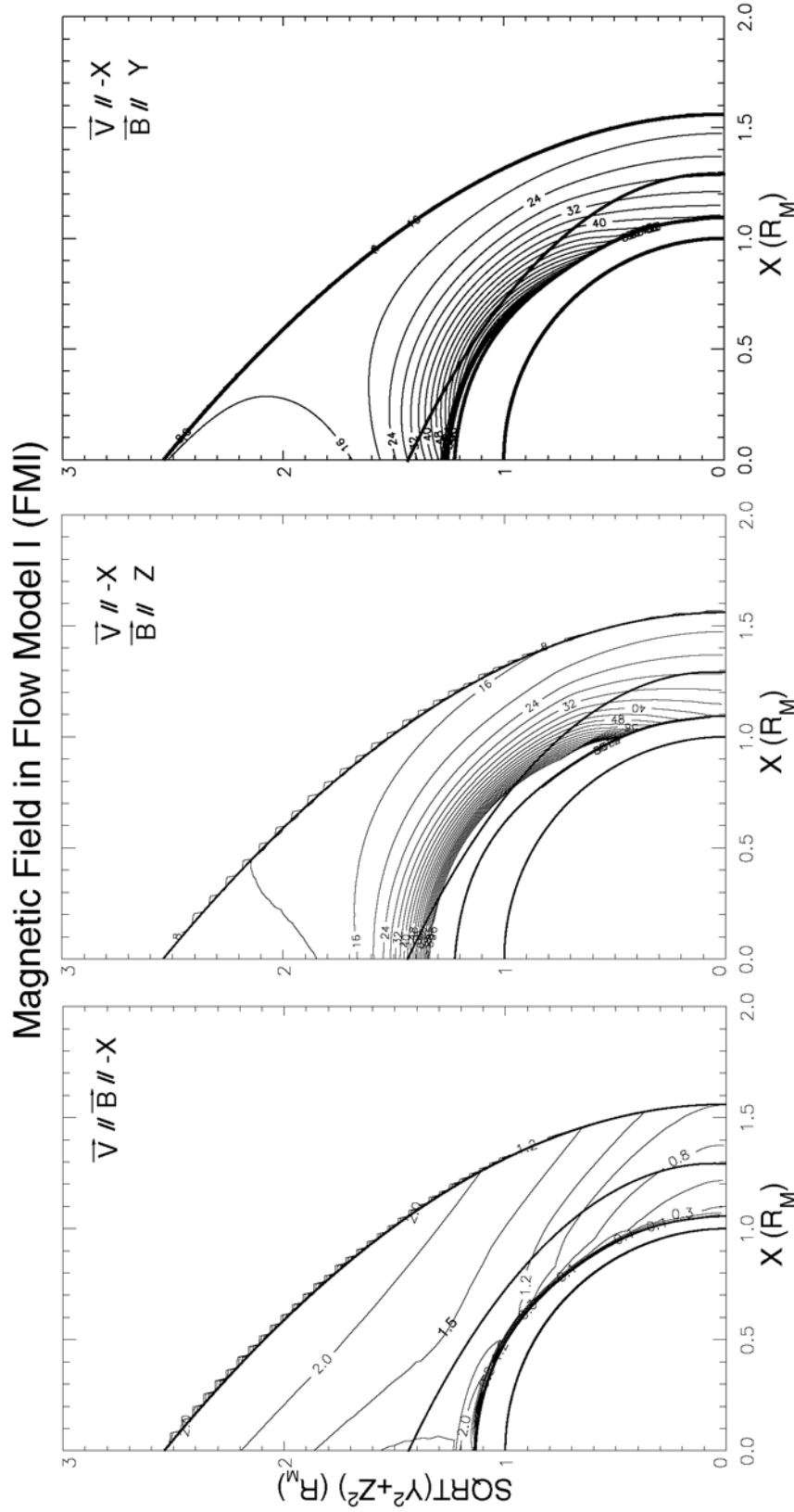


Figure 4.3 Calculated flow field in the dayside by FMI. The panel in left shows the shape of the stream-lines. The middle exhibits density contours and the right are the speed contours (and temperature has a same contour map as that of speed). Numbers on each contour line are the ratio of postshock values to preshock values.



included. Next, for the low Mach number of the post-shock flow, we assume the behavior of protons is localized. Finally, except for the magnetic field, all model parameters employed are taken as axisymmetric.

4.4 Model Results

First are some results from FMI. In figure 4.3 the left panel we can see streamlines in dayside. Calculation is carried out along each line from right side of panel to the left. Also figure 4.3 exhibits the density and speed contours in dayside. Figure 4.4 shows the magnetic field in three specified cases which have been mentioned above. Comparing them with those from SSM, we can say that the correctness of FMI has been proved.

Next let's see some results from FMII. To get the following results, we choose typical solar wind parameters ($V_{sw}=400\text{km/s}$ along $-x$ direction; Mach number=8; proton density $n_{sw}=2.5/\text{cm}^3$) as input to the model, lacking of relevant instruments onboard MGS.

First of all, the reaction rates of charge exchange are shown in Figure 4.5. The left panel is for the reaction $\text{H}+\text{H}^+=\text{H}^++\text{H}$, and the right for $\text{O}+\text{H}^+=\text{O}^++\text{H}$. Both are shown in contours, and the scale is given by the vertical color stripe at right side of each panel. Note that the two scales are not the same. And because the charge exchange is assumed to be axisymmetric around the x -axis in this model, it is sufficient just to show results in one plane. According to the calculations the reaction $\text{H}+\text{H}^+$ dominates except just above the ionopause, where the maximum reaction rate of $\text{O}+\text{H}^+$ is larger, because the hydrogen exosphere extends much further out than the oxygen does, and hydrogen has a larger CE cross section than oxygen. Inside the bow shock, the reaction rate of H decreases with increasing solar zenith angle. As for the relation to altitude, generally the rate first

increases and then decreases with decreasing altitude. The rates of O have the similar functional relationship with SZA and height but are confined in a much smaller region. In other words, hydrogen plays the main role in the CE outside and somewhat inside the MPB. In this model, the peak value for hydrogen reaction occurs at zero SZA and ~400 km altitude, and the one for O is at lower altitude. This kind of distribution of CE rates is easily understood if we keep the flow lines' geometry in mind.

Then, according to the physics we presented before, if we assume the thermal pressure lost due to CE is turned locally into magnetic field pressure, we should be able to see an increase in the magnetic field magnitude which is larger than the result given by the SSM. In other words, in our model, the field increases not only because of the stagnation but also because of the magnetization current caused by CE. Figure 4.6 shows the loss of the thermal pressure due to CE in terms of the increase of magnetic field, that is $\Delta B = \sqrt{2\mu_0(P_0 - P_{CE})}$. It should be noted that the ΔB here is independent of the initial \bar{B}_{sw} . Figure 4.7 gives one result of the model: contours in the xz plane with $\bar{B}_{sw}=4.5\text{nT}$ parallel to the y axis. The left panel tells us that FMI is very successful in reproducing SSM results. Comparing the two panels, we see the effects of the CE: the contours with the same number move to larger altitude after CE. What we need to prove next is whether the increase of the field in our model is sharp enough to form the MPB we observed by MGS.

In Figure 4.8, we give our simulation results for six orbits. To do this, we just need to know the coordinates of MGS vs. time and then the simulated field can be obtained in our 3D model at the corresponding position. No mapping scheme is employed except for the different locations of bow shock, ionopause, for different orbits. For most orbits

(P231, P242, P442 and P456), ER data are available and we could locate the BS, MPB and IP easily (and it's interesting to notice that, according to the ER data, the thickness of the Martian MPB varies from $\sim 200\text{km}$ to $\sim 1000\text{km}$. This indicates that the MPB of Mars is not so sharp as that of comets if compared to the distances to the obstacles; from this point of view, the Martian MPB is more than a “boundary”). However, for orbits like

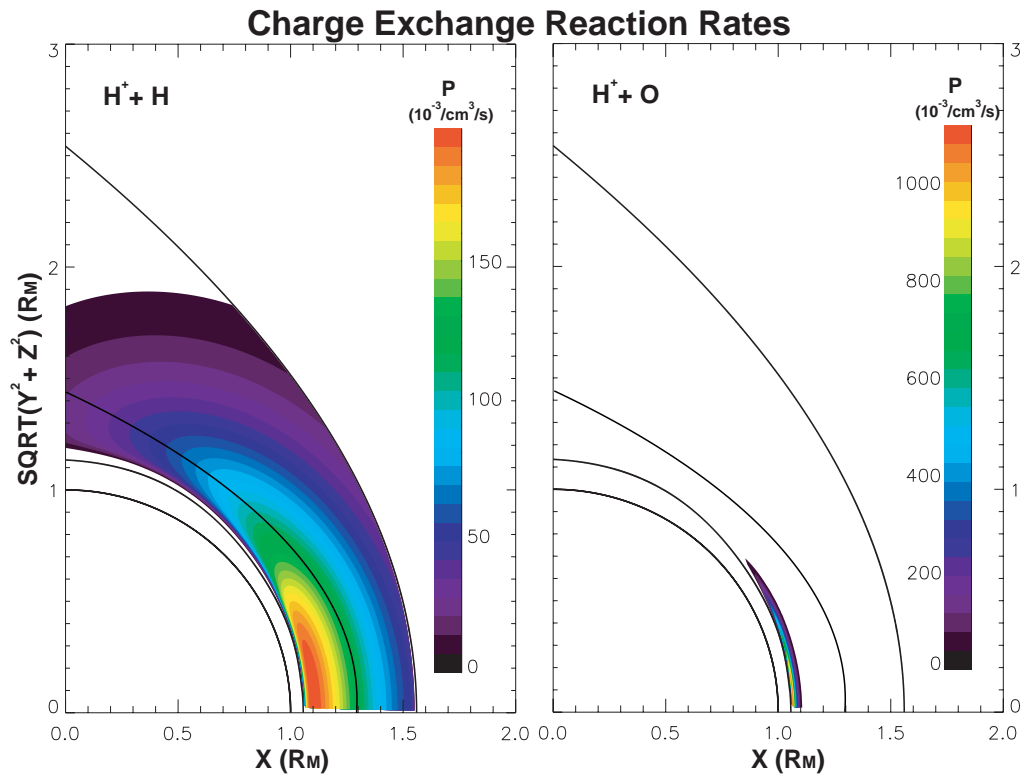


Figure 4.5 Charge exchange reaction rates calculated in FMII. (left) Rates of charge exchange between proton and hydrogen; (right) rates of proton and oxygen. We use different color scale for each panel. From the origin, four thick black curves stand for Mars surface, ionosphere, MPB, and bow shock, respectively.

P361 and P518 with ER data being unavailable for the present, the MAG data can only help us identify BS directly. For orbits like this, we make use of the observed weathervaning of the magnetic field at the dayside ionopause of Mars [Law and Cloutier, 1995; Cloutier et al., 1999] to locate the ionopause first, and then the MPB location and shape model [Vignes et al., 2000] to predict the MPB of each orbit. We show three panels

for each orbit. In the top left panel we show the three components of magnetic field observed by the MGS MAG and calculated by FMI in different colors. This demonstrates that above the CE reaction region FMI gives a good simulation of the data. The bottom left panel shows the magnitude of the magnetic field from MGS, FMI(green) and FMII(red) in time series. The similarity between the observations and results from FMII (especially in the grayed MPB) indicates the validity of the model and the difference between the results from FMI and FMII tells us how crucial a role CE plays in the formation of MPB! The right panel shows the resultant plot for magnetic field magnitude with altitude.

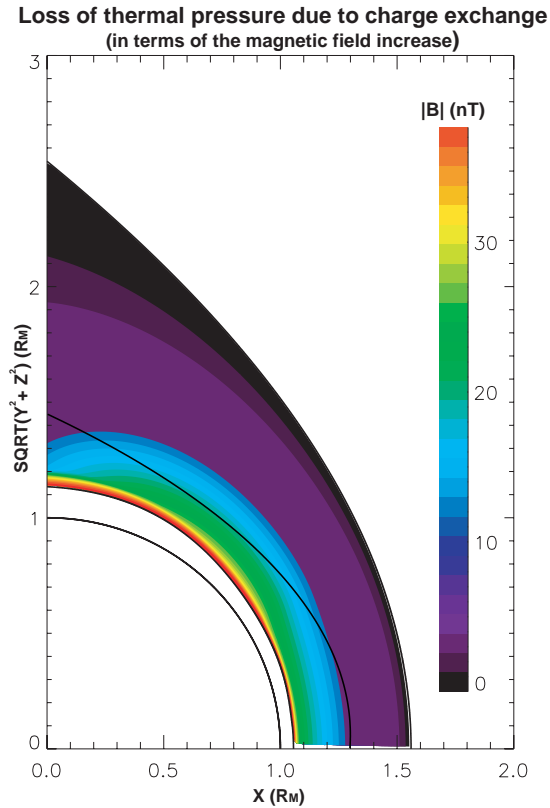


Figure 4.6 Decrease of thermal pressure due to CE, in terms of the increase of magnetic field, that is, $\Delta B = \sqrt{2\mu_0(P_0 - P_{CE})}$ in nT. Because of the axisymmetric around x-axis, only values in on plane are presented.

Moreover, in the six orbits, A and B belong to the low field case, which means $B_{sw} < 4\text{nT}$; C and D, medium field case with $B_{sw} \sim 5\text{nT}$; E and F, high field case with $B_{sw} > 10\text{nT}$. Then we can see that the smaller B_{sw} produces the more obvious difference between the results from FMI and FMII, consistent with what was mentioned above.

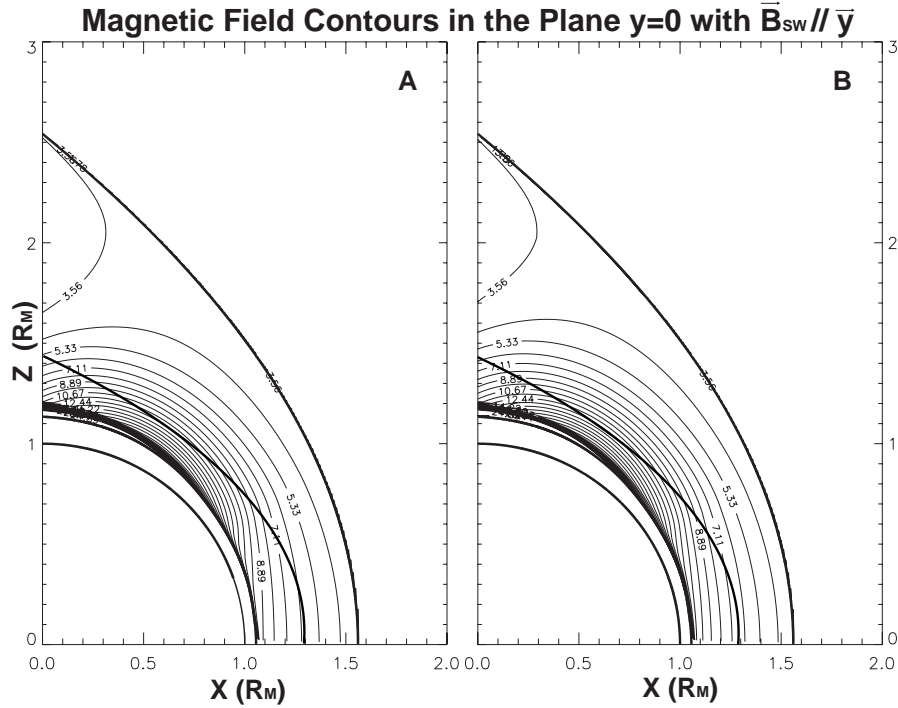


Figure 4.7 Normalized magnetic field (medium field case, preshock $B=4.5\text{nT}$) contour map in plane $y=0$ (A) Contour without CE (FMI). (B) Contour with CE being added (FMII). The relocation of contours after CE can be seen by comparing (A) and (B).

We feel that the overall results for these six orbits indicate that the model scenario involving charge exchange is correct. Errors in our model could be introduced in several ways: initial inputs to our model, such as speed, Mach number, density, magnetic field, etc. of the undisturbed solar wind; positions of the ionopause, bow shock, and MPB. The Martian crustal magnetic field may also contribute to the total field magnitude, e.g., in P456 the magnetic field is much higher than what FMII could produce in the lower part of the MPB. The inaccuracy of some or all of the above parameters can affect the

simulation results. However, since our goal in this paper was not to construct an elaborate model but to use a reasonable model with typical initial input to test the importance of the CE in the MPB formation, our simplifications has been justified by the results fitting with observations.

Above we summary the calculation results from the fluid models. To save calculation time, those charge exchange reaction rates calculated in FMII will be kept on being used in the mode presented next Further discussion about the implications of FMII results will be presented in section 6 after the Monte Carlo model of the exosphere being introduced next.

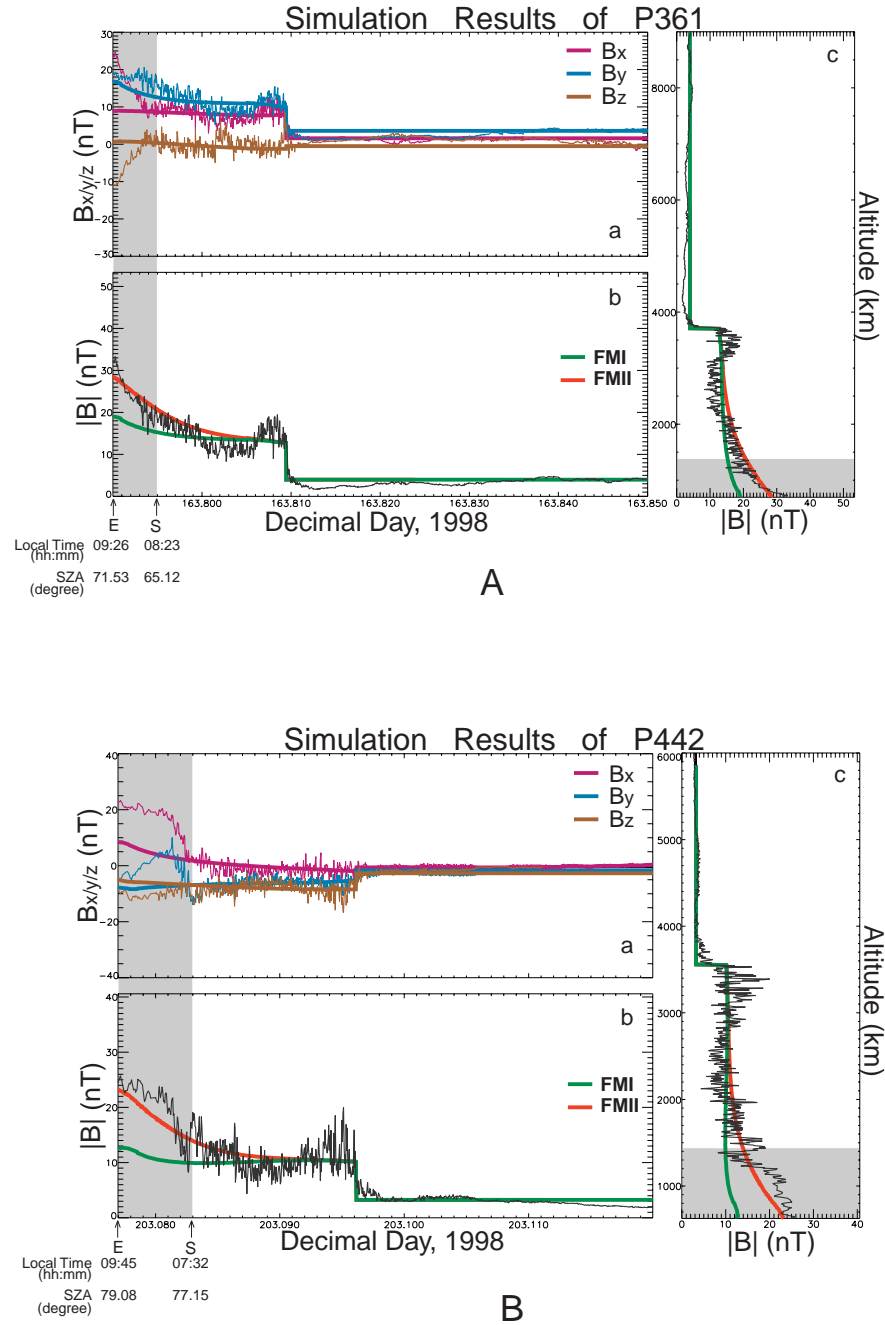


Figure 4.8 Simulation results of six examples. They are outbounds of (A) P361 and (B) P442 (low field case); (C) P231 and (D) P518 (medium field case); (E) P242 and (F) P456 (high field case). For each example, a) (top left) three magnetic field components time series data from MGS and FMI: B_x (purple), B_y (blue) and B_z (brown); b) (bottom left) the magnitude of magnetic field time series data from MGS (black), FMI (green) and FMII (red); c) (right) the magnitude of magnetic field vs. altitude from MGS (black), FMI (green) and FMII (red). Gray stripes are locations of MPB. Numbers below the two small arrows indicated by 'E' and 'S' on the left lower corner of each b) show the locations of S/C crossing the MPB.

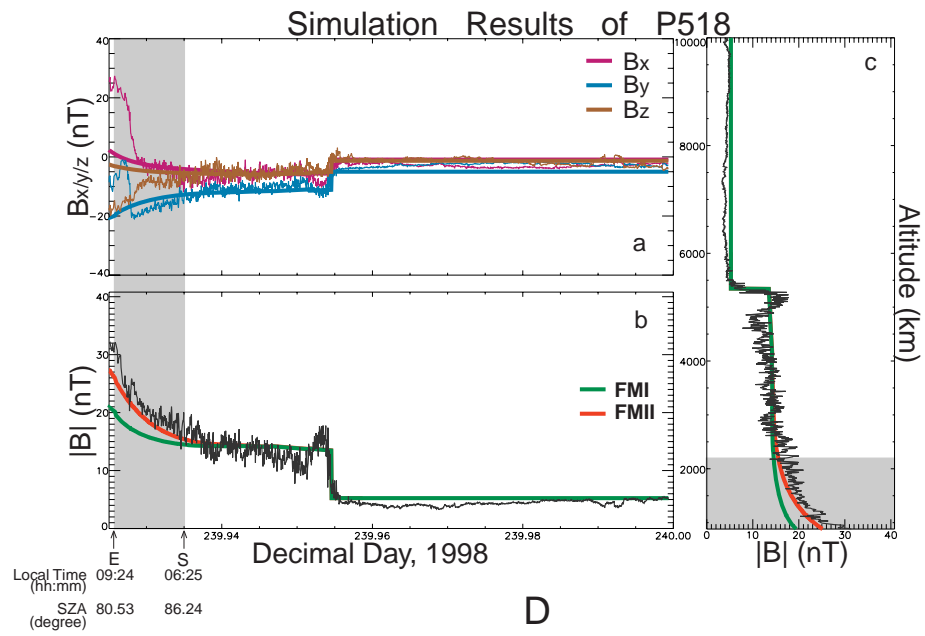
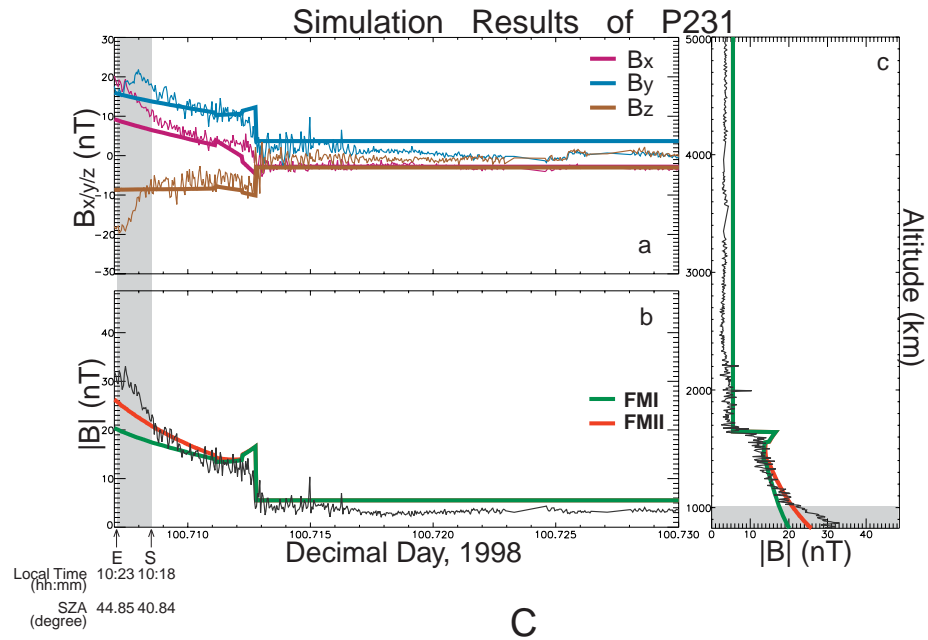


Figure 4.8 (continued)

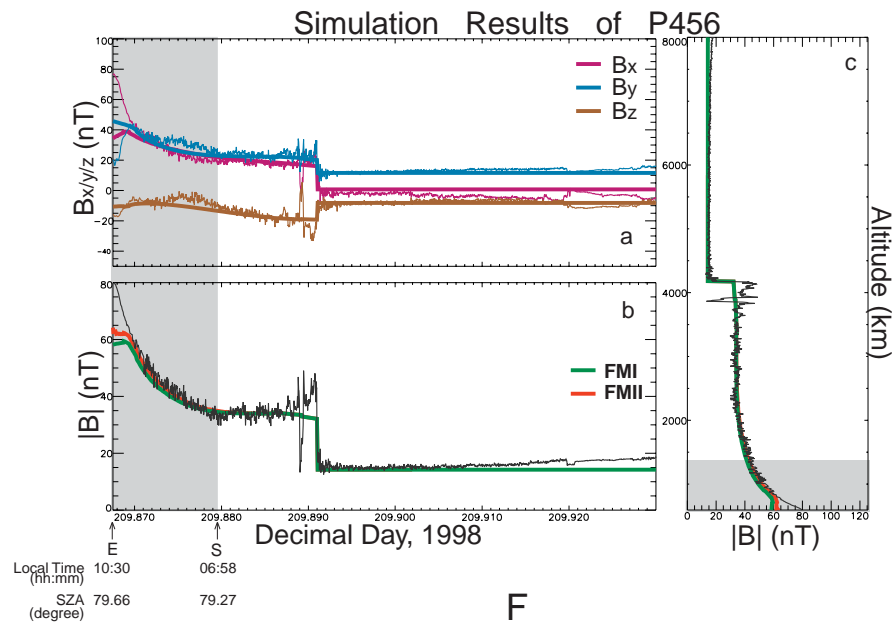
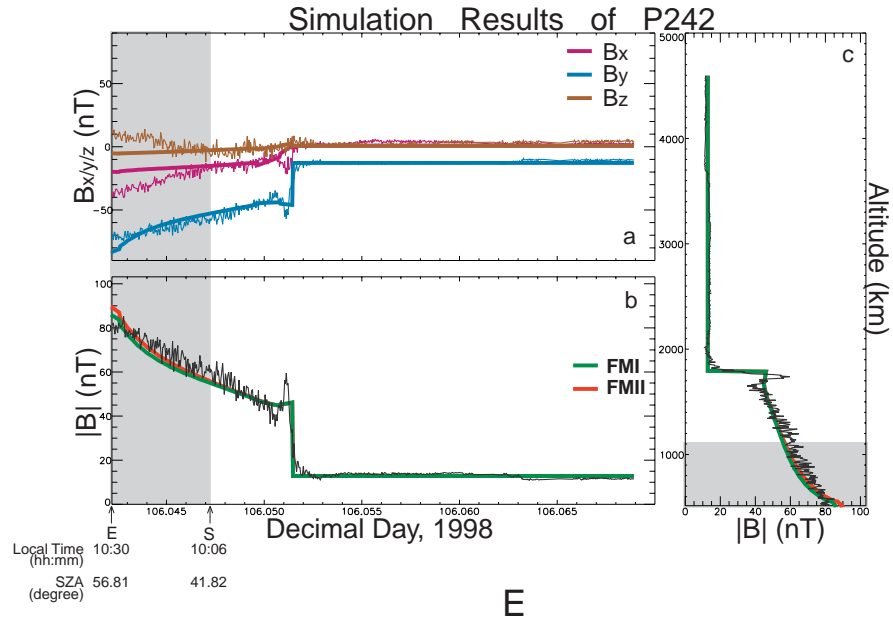


Figure 4.8 (continued)

5. Martian Exosphere Charge Exchange with Solar Wind

As stated in section 3, the exospheres of terrestrial planets (Venus, Earth and Mars) are very different in the degree of involvement in the interaction with solar wind. Without the protection from strong intrinsic magnetic field, both Venusian and Martian exospheres are exposed to the solar wind directly. Due to the low exobase temperature, charge exchange with solar wind plays important role in the loss of Venusian exosphere [Chamberlain and Hunten, 1987]. The same mechanism works in the Martian case, too, although it may not be so prominent. In this section we present the model devoted to study the structure of Martian exosphere subject to the charge exchange with solar wind.

5.1 Underlying Physical Picture

The loss of Martian exosphere, like all other exosphere, is caused by thermal escape and nonthermal escape. The thermal escape, a kind of evaporation in the terrestrial planet case, is the direct way and controlled by characteristics of planet itself: such as the planet gravity field, exobase temperature, and etc. Small moons which have weak gravity field can blow-off exosphere, another kind of thermal escape, like the way solar wind leaving the Sun. The nonthermal escape includes sputtering and all ionization process [Hunten, 1982]. Here ionization indicates the indirect way in which exospheric neutral particle is ionized firstly and then picked-up by solar wind magnetic field and finally lost in interplanetary space. From this perspective, this mechanism is controlled not only by internal factors but also external factors.

The ionization of the exosphere includes three mechanisms: photoionization (PI), electron impact ionization (EII) and charge exchange (CE). Next we discuss briefly each of them.

Photoionization (PI), which lead to the existence of ionosphere directly, occurs when an electron is kicked off the neutral particle A when A is hit by solar EUV photons with energy in excess of the A's ionization potential I_A :



The resulting photoelectron carries off the extra energy of the photon, that is

$$E = h\nu - I_A \quad (5.1.2)$$

and photoion A^+ retains its initial momentum and may end up either in ground state or an excited state which need higher I_A . The PI reaction rate is proportional to the cross section of species A and solar EUV fluxes. Cross section can be obtained by calculation or lab experiment, and change of solar radiation flux is measured by $F_{10.7}$ flux. The rates used in this paper are deduced from those given for 1AU by Banks and Kockarts [1973] since the photoionizing flux drops with the inverse square of the solar distance. An ion produced by PI could be swept away by solar wind and lost.

Charge exchange (CE) is a process in which a neutral particle and an ion exchange the charge, that is,



here we take the traditional picture of CE which is a fly-by process wherein an electron simply jumps from B to A with no momentum transferred. In the case of charge exchange of solar wind proton with exosphere, we are mostly concern with two reactions:



which result in changes in both solar wind and exosphere. Both reactions substitute part of thermal exosphere component by energetic particles H_E , which can not only make

alternation to the density and temperature profile but also enhance the loss of exosphere. On the other hand, the post-shock solar wind is cooled off and slowed down by picked-up ions, therefore changing the magnetic field also. The cross sections of reaction (5.1.4) and (5.1.5) have been studied by Fite (1960), Banks and Kockarts [1973], Stebbings et al. [1964].

Electron impact ionization (EII) is a process in which an energetic electron impacts a neutral and ionizes it. EII can be represented as



with the energy of electron exceeds I_A , and extra energy (incident electron energy minus I_A) distributes itself between two electrons. According to Crider [1999], typical energy distribution is one-sided and most energy goes to the incident electron. The cross sections of H and O are available in papers by Shah et al. [1987] and Thompson et al. [1995].

Ions produced by the above three mechanisms would be carried away by the solar wind and lost. Production of energetic neutral particles (ENP) by CE with solar wind is expected to change the distribution function of exosphere, and this dissertation focuses on this topic.

Now let us make an estimate of the change of density and temperature in the Martian case. Assuming equilibrium has been reached and a fluid approximation is applicable, we can deduce the density change caused by CE with the equation $\nabla \cdot (n_E v) = P_{CE}$, where n_E is the density of ENP and P_{CE} is production rate. Checking the dimension of above equation, we have

$$n_E \sim \frac{P_{CE} l}{V_E} \sim \frac{n_H f_{CE} l}{V_E} \Rightarrow \frac{n_E}{n_H} \sim \frac{f_{CE} l}{V_E} \quad (5.1.7)$$

where f_{CE} is the CE rate at Mars with maximum value $\sim 5 \times 10^{-7} s^{-1}$, l is the length of flow pipe assumed to be $5R_M \sim 1.6 \times 10^4 km$, and V_E is the flow speed $\sim 100 km/s$. Then the upper limit of n_E/n_H is $\sim 1 \times 10^{-4}$! This small number means CE can hardly change the density profile of Martian H exosphere. However, the situation is very different for the temperature structure. If we define the kinetic temperature as

$$T = \frac{\int f(\vec{v}) v^2 d\vec{v}}{\int f(\vec{v}) d\vec{v}} \quad (5.1.8)$$

where symbols carry their usual meanings. Keeping in mind that n_E/n_H is very small, we have

$$\frac{T_{CE}}{T} = \frac{\int f'(\vec{v}) v^2 d\vec{v} + \int f^{SW}(\vec{v}') |\vec{v}' + \vec{V}_{SW}|^2 d\vec{v}'}{\int f(\vec{v}) v^2 d\vec{v}} \quad (5.1.9)$$

where the first term in the numerator is the component from the thermal part and $\sim T$ because of the small n_E/n_H , and the second term is the contribution from the charged exchanged group which we assume essentially have solar wind temperature $\sim 10^6 K$ and \vec{V}_{CE} is the solar wind bulk velocity $\sim 100 km/s$. Expanding the second term, we have

$$\int f^{SW}(\vec{v}) |\vec{v} + \vec{V}_{SW}|^2 d\vec{v} = \int f^{SW}(\vec{v}) v^2 d\vec{v} + \int f^{SW}(\vec{v}) V_{SW}^2 d\vec{v} + \int f^{SW}(\vec{v}) (2\vec{v} \cdot \vec{V}_{SW}) d\vec{v} \quad (5.1.10)$$

where ratio between the first term to T is $\sim (n_E/n_H)(T_{sw}/T) \sim 1$ with $T \sim 10^2 K$, the ratio of the second term is $\sim (n_E/n_H)(100 km/s / 2 km/s)^2 \sim 1$, and the third term equals to zero assuming isotropic distribution function. Then we have $T_{CE}/T \sim 2$ which is prominent. This is reasonable because the change of distribution function concentrates on the high-speed end. In short, CE will change the distribution function of exospheric neutrals, this change is so small that we can hardly see the change of the zero moment of it, however, because solar wind has high velocity and is hot, change in the second moment of the

distribution function is distinct. Furthermore, because of the topology of the interaction of solar wind with Mars, there should exist no more spherical symmetry in the temperature structure.

Before moving forward, it's worthy of mention that CE also happens between the Martian ionosphere and cold H exosphere and this causes the existence of hot H and O Martian corona. However, since it has been pointed out by Russel et al. [1983], Breus [1986] that that hot population of H and O is so low that there should be no major effects on the solar wind interaction, in our model only the cold H exosphere CE with solar wind would be considered.

In section 5.2, we show how the Monte Carlo model of Martian H exosphere is described, and all results are described in the final section.

5.2 Monte Carlo Model of Martian Hydrogen exosphere

As we have stated in section 3, the Monte Carlo method is equivalent to solve the Boltzmann equation. The central point in the Monte Carlo process is to trace the movement of a set of test particles in lifetime and accumulate statistically their information which can be converted to phenomenological hydrodynamic parameters, for instance, concentration, temperature and bulk velocity [Hodges, 1994]. Next, we introduce the aspects of the Martian hydrogen exosphere model piece by piece.

Calculation domain and data audit zones

The life of each test atom always begins from the inner boundary and ends with either escaping from the outer boundary or any termination event (PI, EII) happens. In this calculation, the calculation domain ranges from a lower boundary, the exobase with altitude 200km, to the upper boundary, with altitude at $3 R_{Mars}$, where the number density

of exosphere hydrogen drops to around one hundredth of the value at the exobase and is of the same order of magnitude as that of solar wind protons. The Monte Carlo data audit zone is a spatial volume in which movement data (time and velocity) of the test particle is recorded. In this model, for convenience, we divide the calculation domain into audit zones thusly: firstly, the domain is divided into 40 radially concentric spheres that span from the lower boundary to the upper boundary; afterwards each sphere is again sliced into 12 sectors with 2 hours durations each by constant local time; then each slice is finally divided into 6 blocks along the latitude angles which keep the solid angle of each audit zone equal.

Continuity and boundary conditions

All boundary conditions in this model are chosen to keep the continuity of exosphere particles: on one hand, any test particle returning to the lower boundary is assumed to be immediately replaced at the same point by a new thermal atom, as should be the natural result coming from the existence of a collision-dominated upper atmosphere lying beneath the exobase; on the other hand, the test particle is claimed to escape if it hits the upper boundary with speed large enough to escape while it is “reflected” if its speed is smaller, and this is equivalent to the assumption that no event happens beyond the upper boundary. Here we presume that ‘no event’ happens beyond the upper boundary since exosphere beyond is extremely thin.

Description of particle’s movement in gravity field

All we are concerned about is the movement of the test particle. Since the collision frequency is quite low, it is expected that the particle will spend most (or even all) of its lifetime in the status of free flight in the Martian gravity field. Therefore, after

being launched into the calculation region, the particle should move in segment of ballistic trajectory between any two events (collisions). The categories of particles have been shown in figure 3.1.1. After the initial condition (\vec{r}, \vec{v}) is known, the particle always moves in a plane defined by \vec{v} and \vec{r} pointing from attraction center, and the orbit shape can be described by

$$r = \frac{p}{1 - e \cos \psi} \quad (5.2.1)$$

where e is the eccentricity, p is the focus parameter and ψ is defined as the angle from the x-axis (pointing from the attraction center to the apogee) to the position vector. By conserving the energy and angular momentum, the particle has its radial and horizontal components of velocity in orbit plane like

$$v_r = -e \sqrt{\frac{GM}{p}} \sin \psi \quad (5.2.2)$$

$$v_\psi = \sqrt{\frac{GMp}{r^2}} \quad (5.2.3)$$

here GM is the Martian gravitational parameter.

Orbit parameters are derivable from following formula as long as (\vec{r}, \vec{v}) at any point are get known.

$$e = \sqrt{1 - 4un(1 - w)} \quad (5.2.4)$$

$$p = 2unr \quad (5.2.5)$$

$$\psi(\vec{r}) = \arccos\left(\frac{1 - p/r}{e}\right) \quad (5.2.6)$$

where $u = \frac{v^2 r}{2GM}$ and $n = v_\psi^2 / v^2$. The basic orbit plane vectors are given by

$$\begin{cases} \hat{x} = \hat{r}(\cos \psi - \sin \psi \sqrt{(1-n)/n}) - \hat{v} \sin \psi / \sqrt{n} \\ \hat{y} = \hat{r}(\sin \psi + \cos \psi \sqrt{(1-n)/n}) + \hat{v} \cos \psi / \sqrt{n} \end{cases} \quad (5.2.7)$$

where ‘ \wedge ’ means a unit vector.

Time along an elliptic and hyperbolic trajectories are given relative to the periapsis point, respectively

$$t - t_p = \sqrt{\frac{p}{GM}} \left\{ \frac{er \sin \psi}{1 - e^2} + \frac{2p}{\sqrt[3]{(1 - e^2)^2}} \left[\frac{\pi}{2} + \arctan \left(\sqrt{\frac{1+e}{1-e}} \cdot \frac{1 - \cos \psi}{\sin \psi} \right) \right] \right\} \quad (5.2.8)$$

$$t - t_p = \sqrt{\frac{p}{GM}} \left\{ \frac{er \sin \psi}{1 - e^2} - \frac{p}{\sqrt[3]{(e^2 - 1)^2}} \ln \left[\frac{\sqrt{e+1}(1 - \cos \psi) + \sqrt{e-1} \sin \psi}{\sqrt{e+1}(1 - \cos \psi) - \sqrt{e-1} \sin \psi} \right] \right\} \quad (5.2.9)$$

It should be noted that all above formula are based on Hodges’s work [1994] and with some error corrected.

Collision/Event types and descriptions

In the Monte Carlo method, it’s called an event when the particle’s free movement is interrupted by some collisional encounter with an atom, ion, electron, and photon. Several collisions are included in this research and their characteristics follow next:

Charge exchange (CE). Physics of charge exchange has been mentioned in section 5.1. In our research we take only the CE between exospheric H and solar wind proton into account. Due to the restricted computation resource, we make use of the CE rates calculated by the model in previous section, which is equivalent to assuming the cross section is independent of energy. By doing this, we greatly simplified the Monte Carlo calculation and save a lot of calculation time compared to how collision rates are calculated in Hodges [1994]. After each CE, the code keeps on tracing the movement of the newly produced energetic hydrogen atom.

Lyman alpha scattering (LS). This is not a chemical but physical reaction which provides a net anti-solar force and leads to the change of the particle's trajectory [Chamberlain, 1979; Fahr and Shizgal, 1983]. Physical description of this collision includes two steps: firstly the Ly- α proton is absorbed by the test particle and then reradiated immediately. We take the line center 121.6nm as the wavelength of the Ly- α so that the velocity change in the exospheric H in both absorption and reradiation of Ly- α proton is 327cm/s. In our study, we assume the Martian H exosphere is optical thin and choose a medium Lyman scattering rate $9.64 \times 10^{-4} s^{-1}$ (interpolated from the rates on Earth and Venus [Hodges and Tinsley, 1981]) which is much larger than those of other collisions and that is the reason we include it in the model.

Photoionization (PI). A hydrogen atom is deprived of an electron when a solar photon hit it with energy larger than 13.6eV. The photoionization rate depends on the solar activity which is measured by $F_{10.7}$ index. In our research we choose the medium photoionization $4.8 \times 10^{-8} s^{-1}$ (interpolated from the rates on Earth and Venus [Hodges and Tinsley, 1981; Hodges, 1994]) and assume that any photoionized particle would be swept off by solar wind electromagnetic field immediately so that photoionization works as a sink of neutral particles in the model.

Electron impact ionization (EII). This reaction will not be included in this research but is worthy of mention. EII has being studied by Crider [1999] to simulate the change of electron spectrum observed by MAG/ER onboard MGS. Generally the EII has reaction rate approximately as half as that of CE and works as another sink of neutral particles since ions produced by EII is assumed to leave exosphere by solar wind EM filed immediately, too.

Besides the above collisions, the self-rotation of Mars is also incorporated into the model by adding an extra velocity component defined by the Martian rotation angular velocity— $7.09 \times 10^{-5} \text{ rad/s}$ pointing northward—crossing the particles leaving exobase. Moreover, the effects of a background exosphere component, the oxygen in this case, should be considered, too.

After knowing how to describe the particle's movement in the gravity field and type of collisions, we still need to determine when, where and what collision will occur. To achieve this, when a test particle is launched into the calculation regime at time t_0 and its life begins, one number R_i randomly chosen from a uniform distribution ranging 0-1 is assigned initially to that particle for each above interaction i . Then, following the trajectory of that particle, the survival function of interaction i at time t is given by

$$\eta_i(t) = \ln(R_i) + \int_{t_0}^t \nu_i(\bar{r}) d\tau \quad (5.2.10)$$

where the encounter frequency of i at position \bar{r} , $\nu_i(\bar{r})$, in the second term may vary spatially. The $\eta_i(t)$, being negative initially, increases with time by the integration, and then the one reaching zero first determines the location, time and type of interaction. In order to determine the magnitude and direction of the target particle's velocity in the reference of the test particle, three random variables are attributed and they are

$$R_v = \frac{\int_0^v f(\bar{v}_r) v_r^3 dv_r}{\int_0^\infty f(\bar{v}_r) v_r^3 dv_r} \quad (5.2.11)$$

$$R_{\theta} = \frac{\int_{\theta_0}^{\theta_s} \sin \theta d\theta}{\int_0^{\theta_s} \sin \theta d\theta} \quad (5.2.12)$$

and

$$R_{\phi} = \frac{\int_{\phi_0}^{\phi_s} d\phi}{\int_0^{\phi_s} d\phi} \quad (5.2.13)$$

where the (V, θ, ϕ) are components of the velocity.

Flow chart

In figure 5.1 we show the flow chart of the codes. As we can see, each test particle is launched from the exobase and its trajectory must be one kind of conic curves in Martian gravity field before its movement being interrupted by some interaction. From the very beginning of each particle's life, a group of variables initially being attributed by negative random number each has been given to the particle to represent interactions, as are shown in the diamond blocks and, technically speaking, any interaction can be easily plugged in the codes. Some interaction occurs if and only if the value of corresponding variable increased to be positive as the particle moves. In current model, the life of the particle is terminated when it either is photoionized by solar radiation or reached the upper boundary with escaping or even larger speed.

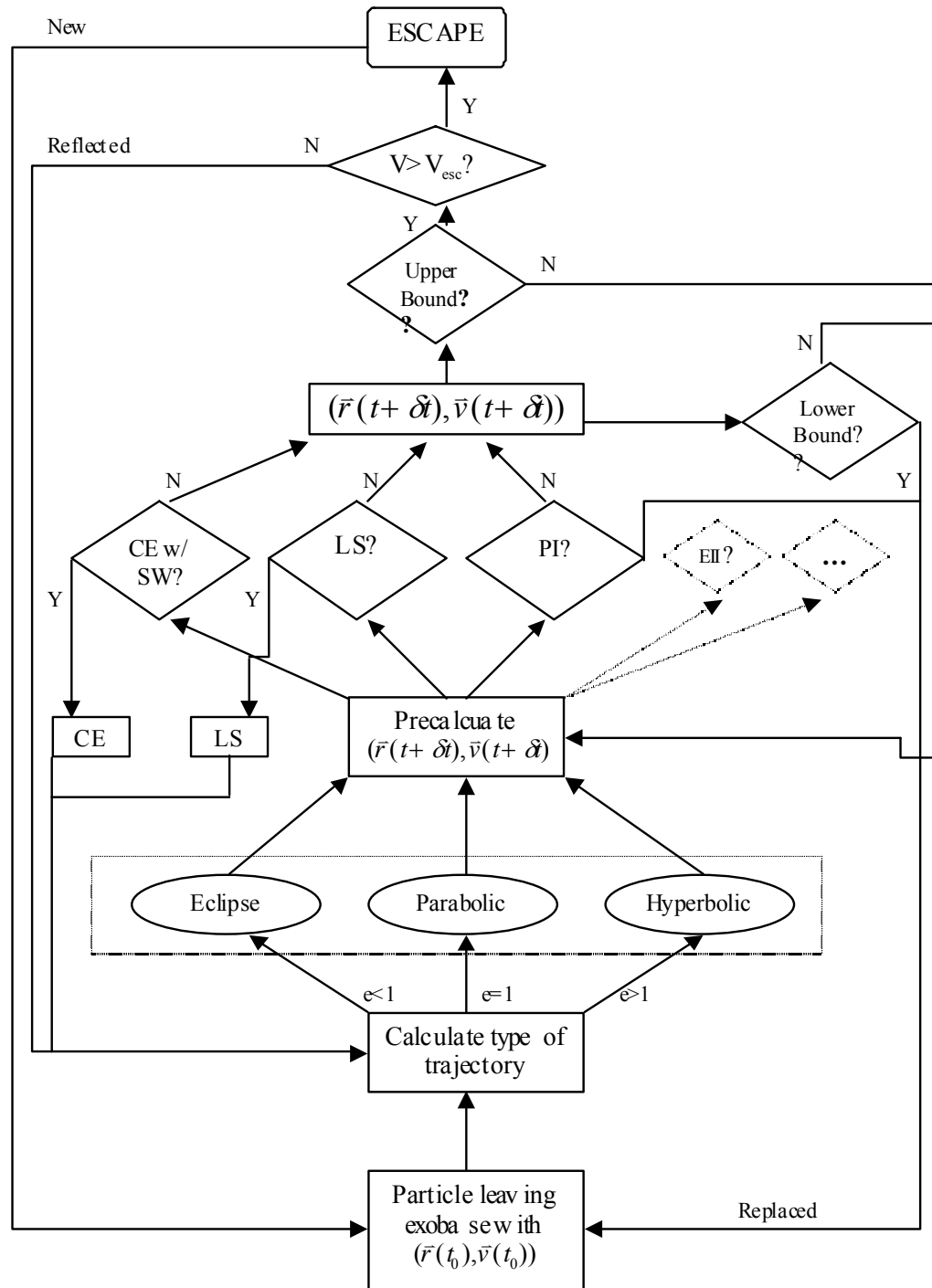


Figure 5.1 Flow chart of the codes

5.3 Model Results

Now we present the results of four runs of the exosphere codes. First we run the codes without CE, LS and PI as a benchmark and name it as the primary exosphere (PRE). Then the codes are re-run, this time all interactions is included, to simulate the charge exchanged, Lyman scattered and photoionized exosphere (CELSPE). By comparing those two outputs, we could see clearly how the CE affects the structure of a collisionless Martian exosphere. After that we investigate the effects of CE on collisional Martian exosphere by introducing background major constituent O in two more runs, which are named as the primary exosphere with O (PREO) and the exosphere with CE and O (CELSPEO). Table 5.3.1 shows elements of each model explicitly.

Table 5.3.1 Martian Exosphere Models

		CE	LS	PI	Planetary rotation	O
Collisionless	<i>PRE</i>	×	×	×	√	×
	<i>CELSPE</i>	√	√	√	√	×
Collisional	<i>PREO</i>	×	×	×	√	√
	<i>CELSPEO</i>	√	√	√	√	√

To get following results, we chose a typical exobase temperature of 350K all around the exobase, and all movement information of particles is recorded in the Mars-Solar-Ecliptic coordinates. That is, the x-axis points from Mars to the Sun, the y-axis is the negative of the revolution velocity direction of Mars and the z-axis forms the right-hand system with x and y and points to north. For reference, theoretical models of collisionless hydrogen exosphere (THE), including both the exosphere model with satellite group (EWS) and exosphere model with no satellite group (EWNS), have been calculated analytically with all formulas have already been presented in section 3.1 and 3.4.2.

5.3.1 Collisionless Models

For the collisionless models, first let us see how the exosphere distributes with altitude. The panel A of figure 5.2, 5.3 and 5.4, which present the spherically averaged value at each altitude point, depicts the exosphere density, radial velocity and temperature profiles, respectively, and the theoretical curves (in black) are plotted as the criteria. It's obvious that in each plot the PRE and EWNS curves overlap each other, as is consistent with the assumptions of PRE so that demonstrates the integrity of the code. Next let's have a closer look at those figures.

In figure 5.2A, by comparing the two black curves, we can see that the existence of satellite particles increases the exospheric density. PRE (green symbols) obviously doesn't have any satellite particles. However, Lyman scattering can work somewhat like the collisions between particles and produce a small amount of satellite particles which lead to larger density in CELSPE but not as large as EWS. Moreover in figure 5.2A, for both PRE and CELSPE, at each altitude point, there are three symbols that represent the globally averaged, dayside averaged and nightside averaged density, respectively. Overlapping of the three symbols claims the symmetry in density is kept even after CE and LS.

The figure 5.3A shows that the existence of satellite particles produced by LS can similarly decrease the value of radial velocity in CELSPE. Furthermore, at data points with central distance $\sim 3R_M$ there is a small bulge whose existence can be seen more clearly in 3-D results and explained there.

In figure 5.4A are the temperature profiles where effects of CE are distinct. In order to show the anisotropy, we also give out temperature components in both horizontal

and radial directions (T_h and T_r) besides the total temperature (T_t). It is explicit that temperature changes greatly in CELSPE: the difference for T_t grows with altitude; and for T_h it increases similarly as T_t while for T_r , difference is prominent at high altitude only. The change of CELSPE thermal structure can only be caused by the CE with solar wind, since both LS and rotation can hardly alter the velocity distribution function, and the order of magnitude of the change is in accordance with the initial estimation in section 5.1.

Because the change of exosphere is not expected to be isotropic in 3-D space, next we further depict the exosphere models' results in several specified planes. In each following figure, there are always two columns and the left is for primary exospheres and the right exospheres with CE.

Figure 5.5A presents the density contours in equatorial, noon-midnight and terminator cuts (from up to bottom panels; and note that following figures about contours, all in 2 columns and 3 rows, are constructed in the same order). Comparing two panels in each row, we can finally assert that, except for a small outward expansion of contours caused by LS, change of density is hardly discernable and even the spherical symmetry is kept.

The asymmetry effects of CE can be seen from figure 5.6A, which shows contours of radial velocity in three cuts. It is obvious that LS can produce satellite particles to reduce the bulk radial velocity. However, the energetic particles produced by CE have the tendency to increase the radial velocity in the flank of Mars, and due to the shield of Mars few energetic particles can be found in nightside. The effects of the satellite particles produced by LS and the high-speed escaping particles produced by CE

combine together and make an asymmetry in the radial speed field, shown as the “green bulge” in the contours in the equatorial (the right panel in row (a)) and noon-midnight planes (the right panel in row (b)), and that’s also the reason we see a “bulge” around $3R_M$ in figure 5.3A.

In figure 5.7A are temperature contours in the three cuts. In plots of the right column we can see that the green region ($\sim 200K$ from color scale) extends much further outward than in the left, as caused by CE. Moreover, some hot regions, which have “warmer” color like yellow and red, can be seen located between the bow shock (BS) and magnetic pileup boundary (MPB). This is because more NPEH atoms produced by CE travel through the flank and fly to nightside under the influence of gravity field, and because of the shield of Mars itself and the high speed of those particles, we can see a cooler region at nightside. Similar result can be seen in plots in the second row which are contours in the noon-midnight cut. Furthermore, the spherical symmetry in the temperature structure of PRE is destroyed because of the presence of CE, too. In the last row are contours in the dawn-dusk plane and in this plane the increase is almost symmetric.

Finally in figure 5.8A we show the normalized distribution function of PRE and CELSPE at several altitudes, as well as the isotropic Maxwellian distribution (with temperature determined by the theoretical exosphere model) for reference. Due to the absence of satellite and forbidden incoming particles (which have speed large enough to escape), the anisotropy in PRE distribution grows with altitude and extends to the low velocity range (refer to the figure 3.1 and 3.3A). That’s the reason the PRE curves fit with Maxwell curves pretty well in the panel (a)-(d) except at the high-speed end (note in

(a) and (b) the escaping speed locates on point 5 at x-axis and in (c) and (d) on (4)), while in panel (e) and (f) an “overshoot” merges at $x=6$ (refer to table I for velocity range at each integer x point) and is compensated by particles in both sides and this phenomena can be explained by the same reason as above: at high altitude the incoming particles dominates in the ideal Maxwellian distribution so that the distribution of PRE gets far from Maxwellian-like even in the small speed range, and since the relative weight of particles with small speed decreases (figure 3.1 and 3.3A) so that the “overshoot” must occur to compensate. Since LS can only change direction of particle’s velocity and hardly the magnitude, the difference between PRE and CELSPE should be accounted for CE. For CELSPE each curve is composed by two parts, one is the thermal part on left and the other is the hot part on right. Clearly CE with solar wind introduces a group of energetic particles whose energy spectra concentrate on the very-high-speed tail, with relative percentage of energetic particles increasing upward. The change of the thermal part of CELSPE curve (especially for $x=7$) is most distinct in the post-shock region (as shown in (b)-(c)) since solar wind bulk speed is greatly decelerated to $\leq 100\text{km/s}$ there, and in (e) and (f) we see that the change of distribution function mainly locates in velocity range as high as 110km/s and beyond, while in (d) changes in both thermal and non-thermal part are obvious.

5.3.2 Collisional Models

From above we can see that: in this collisionless exosphere model on one hand the kinetic temperature of the exosphere will increase due to the hot ENHA group (with post-shock temperature $\sim 10^6\text{K}$) produced by CE; on the other hand the increase doesn’t distribute evenly and has a maximum region located between BS and MPB, because most

ENHA produced in the dayside must pass through that region. However, will the role of CE stays as prominent as before or maybe become trivial after the effects of the background major exosphere component—O—being included? That’s the reason we introduce the collisional Martian exosphere models that will count atomic oxygen in and being more realistic-like.

We know that the thermal Martian oxygen exosphere has very a small scale height while the hot oxygen corona is rare so that it is assumed that the collision between O and H is confined in a small region. Therefore, by making use of the model in section 4.3, a thin layer of isothermal oxygen exosphere ranging from the exobase up to 1000km altitude is present in model PREO (the primary exosphere with O, the benchmark model) and CELSPEO (the charge exchanged exosphere with O), and the validity of the simplification is obvious from figure 4.2. The thermal part of this oxygen exosphere actually presumes its temperature being constant—350K. Furthermore, to simplify the calculation and save CPU time, we also make another assumption that the oxygen-hydrogen collision is always elastic and has an energy-independent cross section: $3.5 \times 10^{-20} m^2$.

The results from PREO and CELSPEO are shown in the part B of figure 5.2—5.8, which are all constructed in the same order as that of corresponding part A. In figure 5.2B, density profile of PREO doesn’t fit the analytic EWNS profile anymore but falls between the EWNS and EWS lines since the presence of O exosphere can help to produce satellite particles, and moreover, in CELSPEO the LS can’t change density as much as before because of the same reason. The radial velocities are larger than those of analytic model THE in figure 5.3B and the “bulge” still exists but getting much smaller,

as is because the more satellite particles are produced than before because of the presence of O exosphere. The reason why the radial speed increases is obvious in the figure 5.4B, which depicts the temperature profiles and we can see that even the PREO has larger temperature than PRE. A closer look at the figure shows that the kinetic temperature at the exobase is about 25-30K larger than it should be. This small error is introduced by the assumed constant temperature of the O exosphere: when colliding with O with temperature 350K at higher temperature, the hydrogen get its temperature larger and when it falls back to exobase it will “heat up” the exosphere there and that is the reason we see a exobase temperature higher than 350K. Furthermore, after CE the increment in temperature components is still prominent in figure5.4 B.

From above we can see that the existence of O exosphere depresses the influence caused by LS in the CELSPE. This point can be seen more clearly in following contour figures. For example, figure5.5B shows the density contours of the PREO and CELSPEO, and both are almost the same as CELSPE. In figure 5.6B the increase of radial velocity after LS is still outstanding while the asymmetry is not so noticeable as that in the CELSPE (and since the color scale in figure 5.6B carries a too small maximum, the contours are plotted again in figure 5.6C with a different color scale). That is all because that the collision between oxygen and hydrogen exosphere is another source of hydrogen satellite particles besides the LS. In figure 5.7B, although the relative increase of temperature is not so larger as before, the spatial distribution of hot region in the CELSPEO stays the same as that in the CELSPE, as is in accord with our instinct.

Finally in figure 5.8B are the normalized distribution functions of PREO and CELSPEO at six different altitudes as figure 5.8A. Similarly, we put theoretical result

(with exobase temperature 350K) as reference again. Likewise the PREO behaves like PRE. After the CE being included, change in the thermal part is not distinct as before since the distribution of PREO is relative large in the high-speed end of the thermal part, while the change in the non-thermal part is still obvious, especially in panel (f) part of it joins with the end of thermal part.

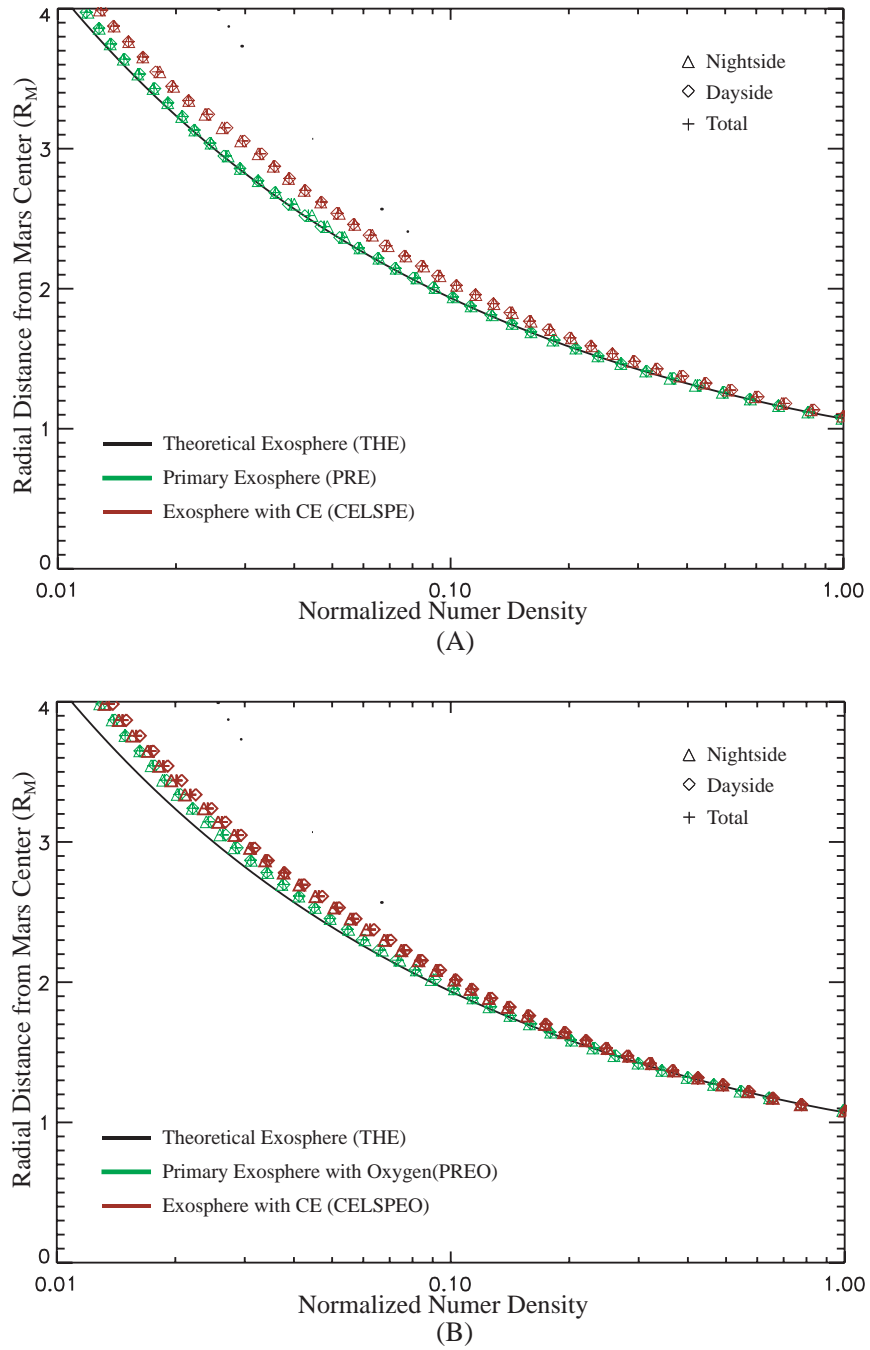


Figure 5.2 Exospheric normalized density profiles. (A): two for theoretical exosphere (THE, in black), the one with smaller value is for exosphere with no satellite particles (EWNS) while the other is for exosphere with satellite particles (EWS); collisionless primary exosphere (PRE, in green); and charge exchanged exosphere (CELSPE, in brown). For both PRE and CELSPE, at each data point there are three symbols, with plus sign for global averaged value, diamond for dayside average and triangle for nightside average. (B): profiles of THE, the collisional exosphere model PREO and CELSPEO.

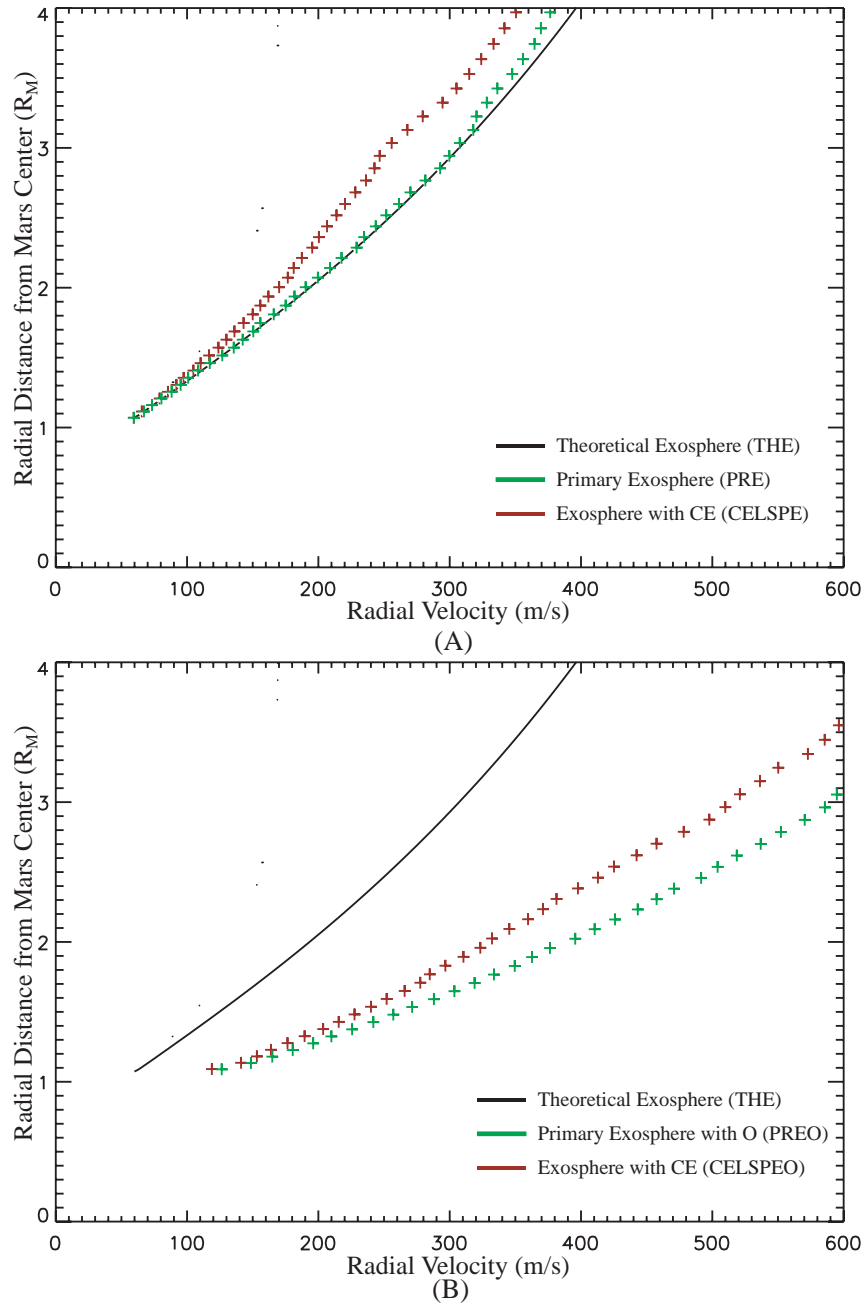


Figure 5.3. Exospheric radial velocity profiles. (A): theoretical exosphere (THE, in black), the one with larger value is for exosphere with no satellite particles (EWS) while the other is for exosphere with satellite particles (EWS); collisionless primary exosphere (PRE, in green); charge exchanged exosphere (CELSPE, in brown). (B): profiles of THE, the collisional exosphere model PREO and CELSPEO.

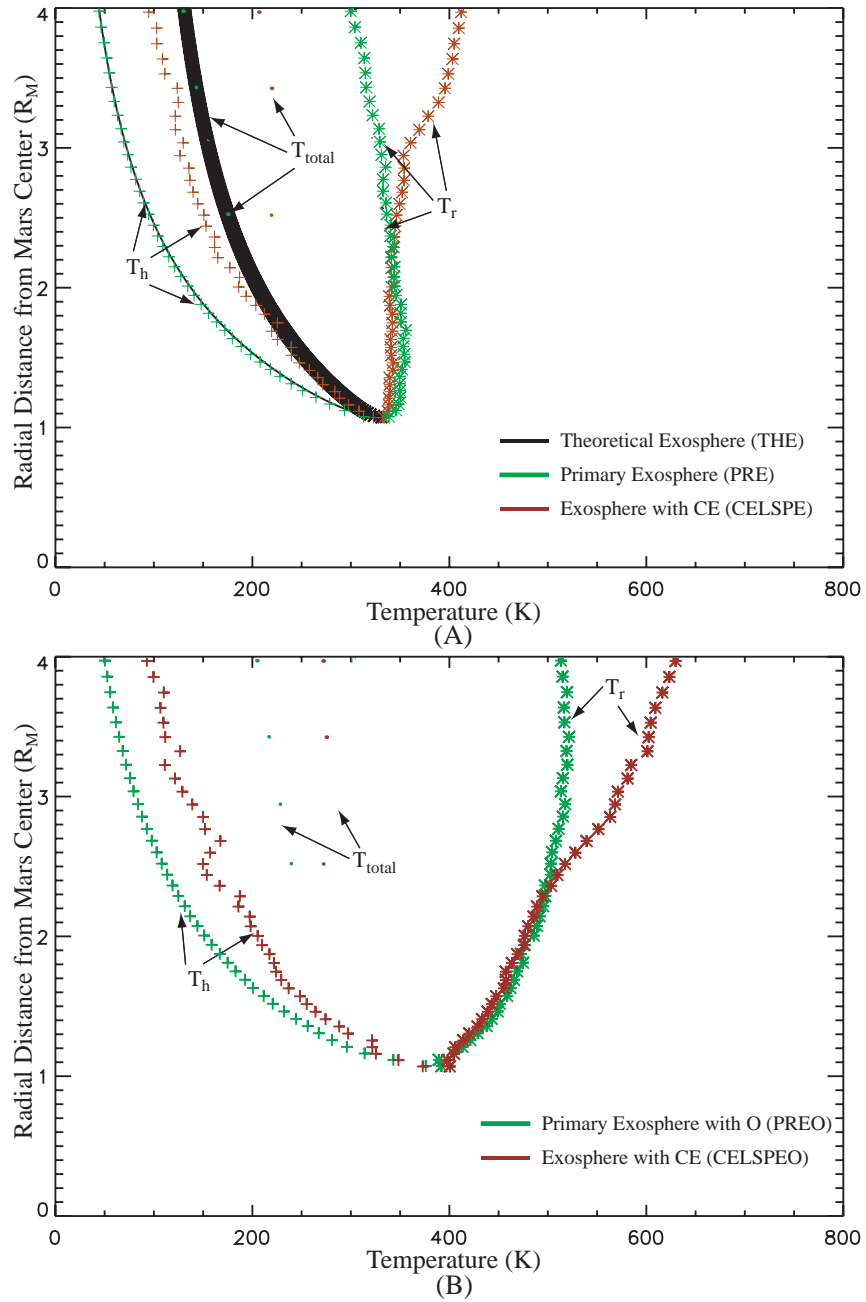


Figure 5.4. Exospheric temperature profiles. (A): theoretical exosphere (THE, in black); collisionless primary exosphere (PRE, in green); charge exchanged exosphere (CELSPE, in brown). For each case, besides the total temperature (T_{total} , middle), two temperature components in horizontal direction (T_h , left) and radial direction (T_r , right) are presented. (B): profiles of the collisional exosphere model PREO and CELSPEO.

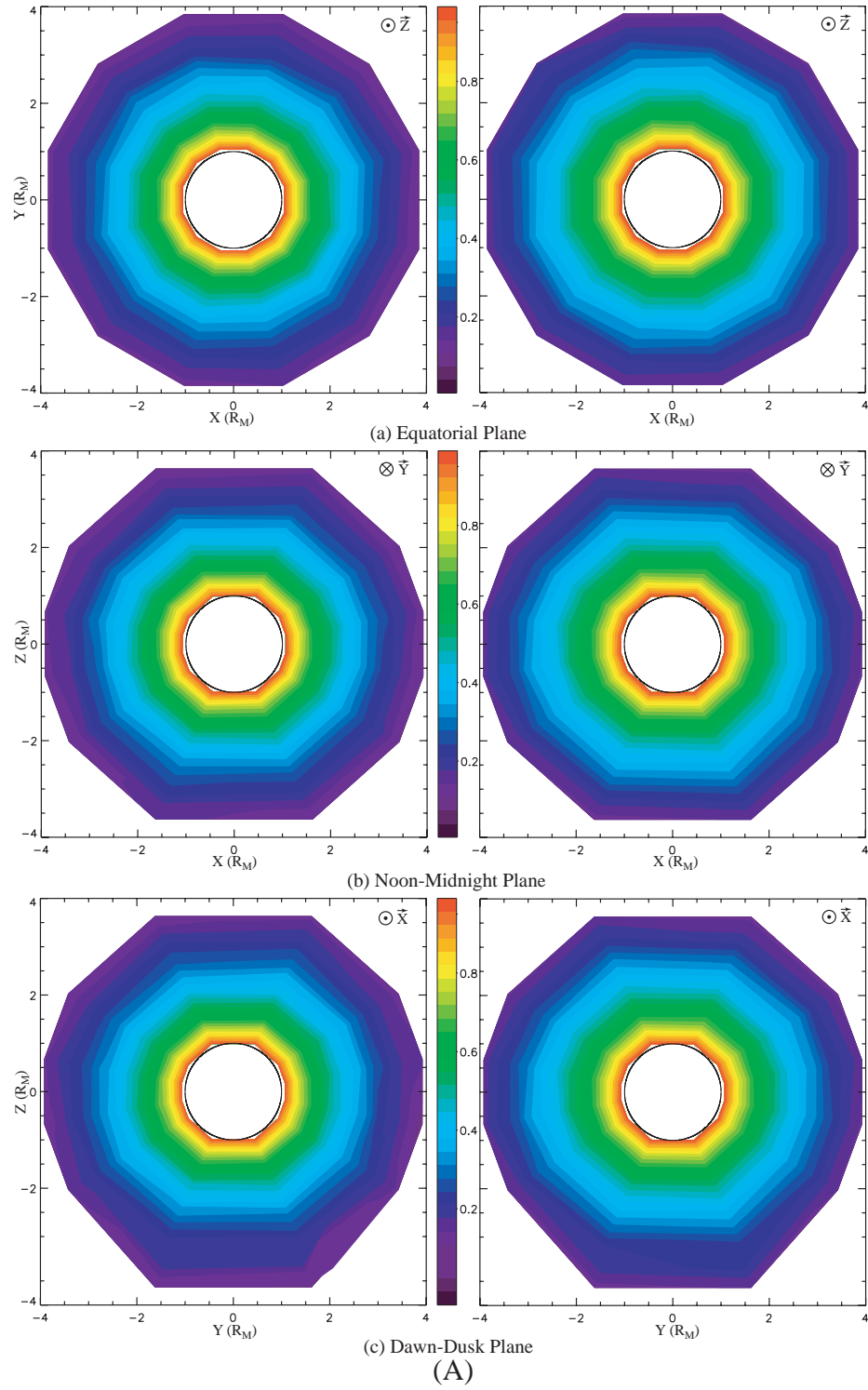


Figure 5.5 Exospheric density contours in three cuts. (A): collisionless primary exosphere (PRE, left) and charge exchanged exosphere (CELSPE, right). The Mars-Solar-Ecliptic coordinate system is used in each panel. (B): collisional primary exosphere (PREO, left) and charge exchanged exosphere (CELSPEO, right).

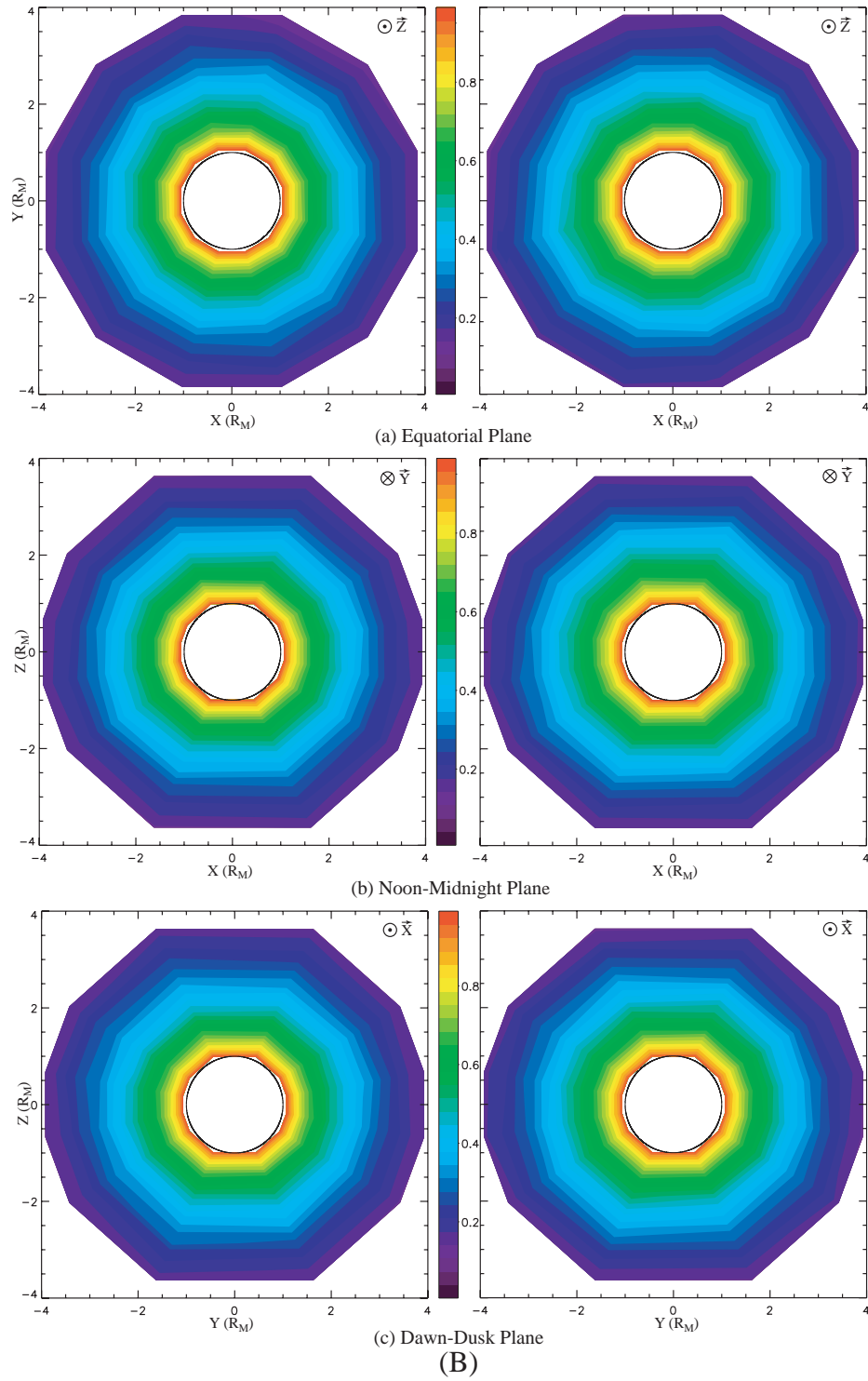


Figure 5.5 (continued)

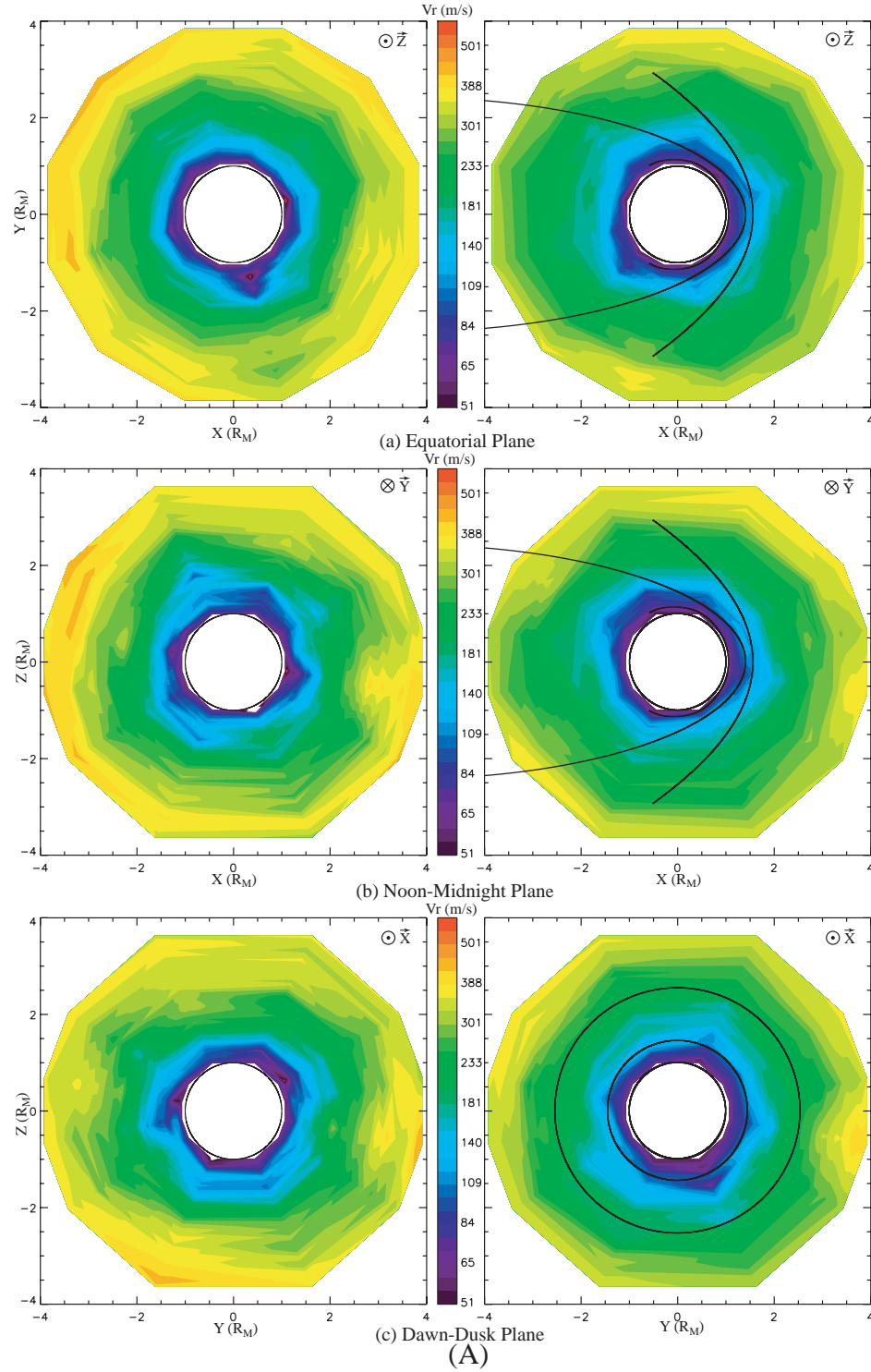


Figure 5.6 Exospheric radial velocity contours in three cuts for two cases. (A) collisionless primary exosphere (PRE, left) and charge exchanged exosphere (CELSPE, right). The Mars-Solar-Ecliptic coordinate system is used in each panel. (B) collisional primary exosphere (PREO, left) and charge exchanged exosphere (CELSPEO, right). (C) Same as (B) except for different color scale being used.

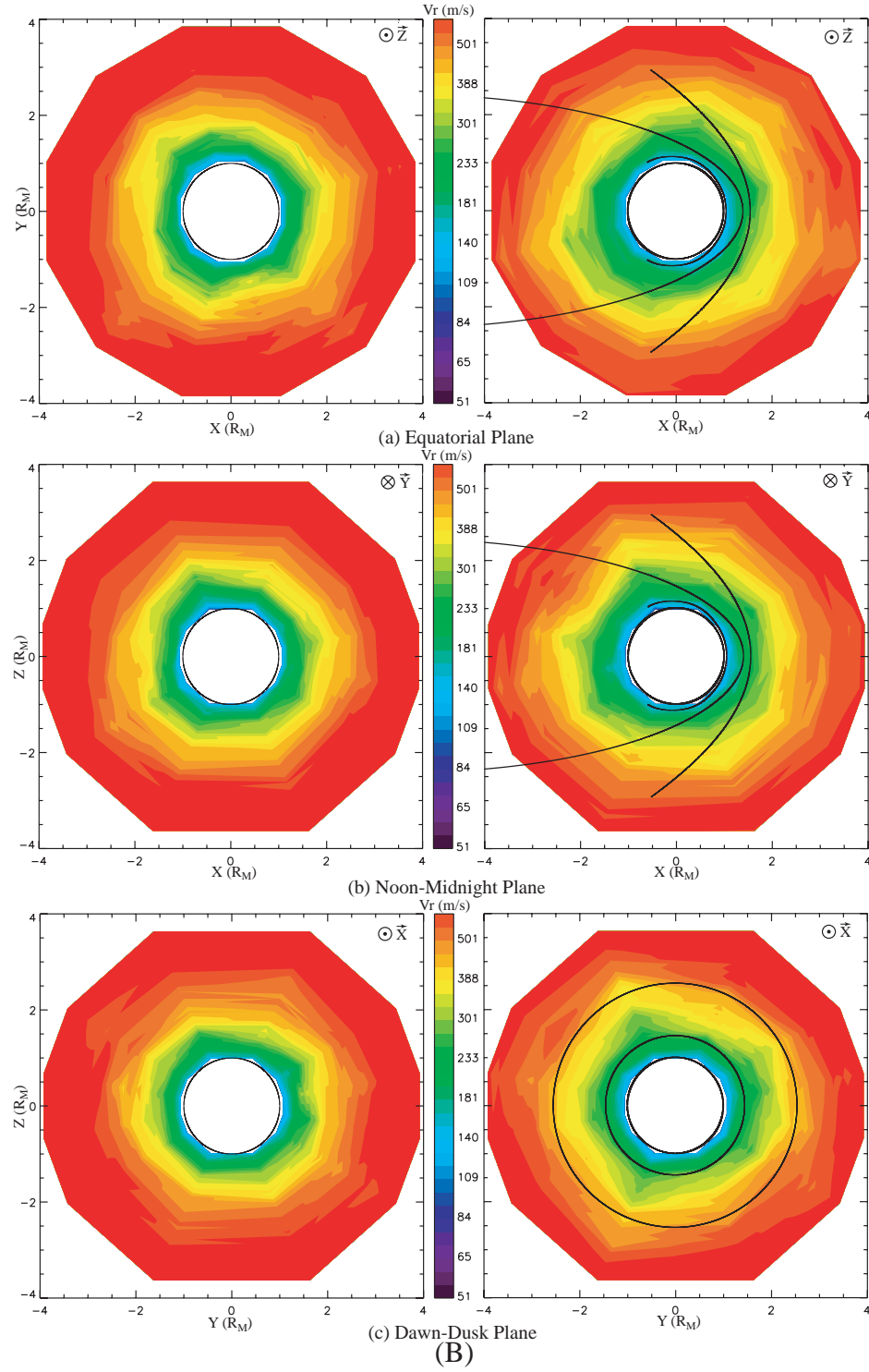


Figure 5.6 (continued)

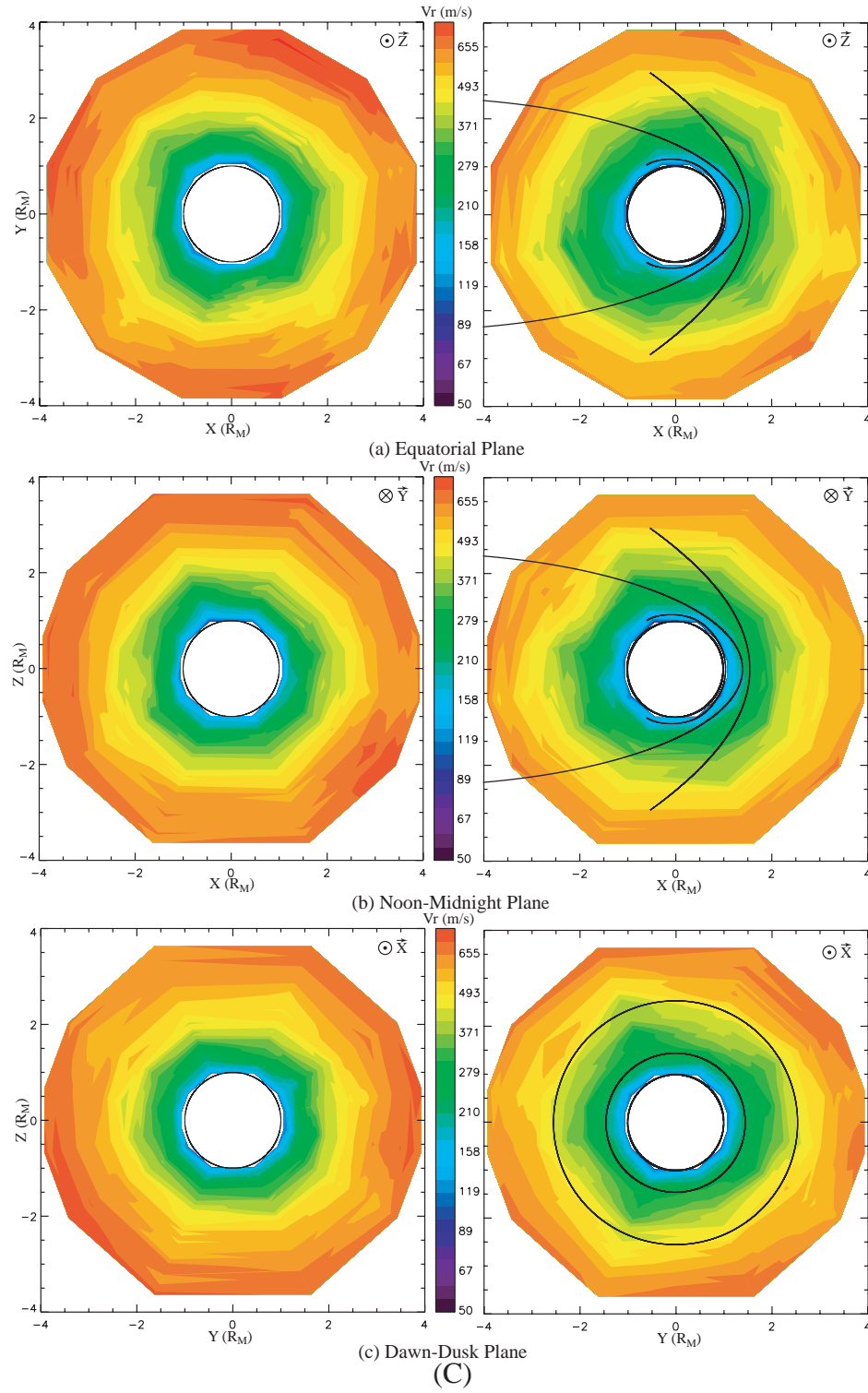


Figure 5.6 (continued)

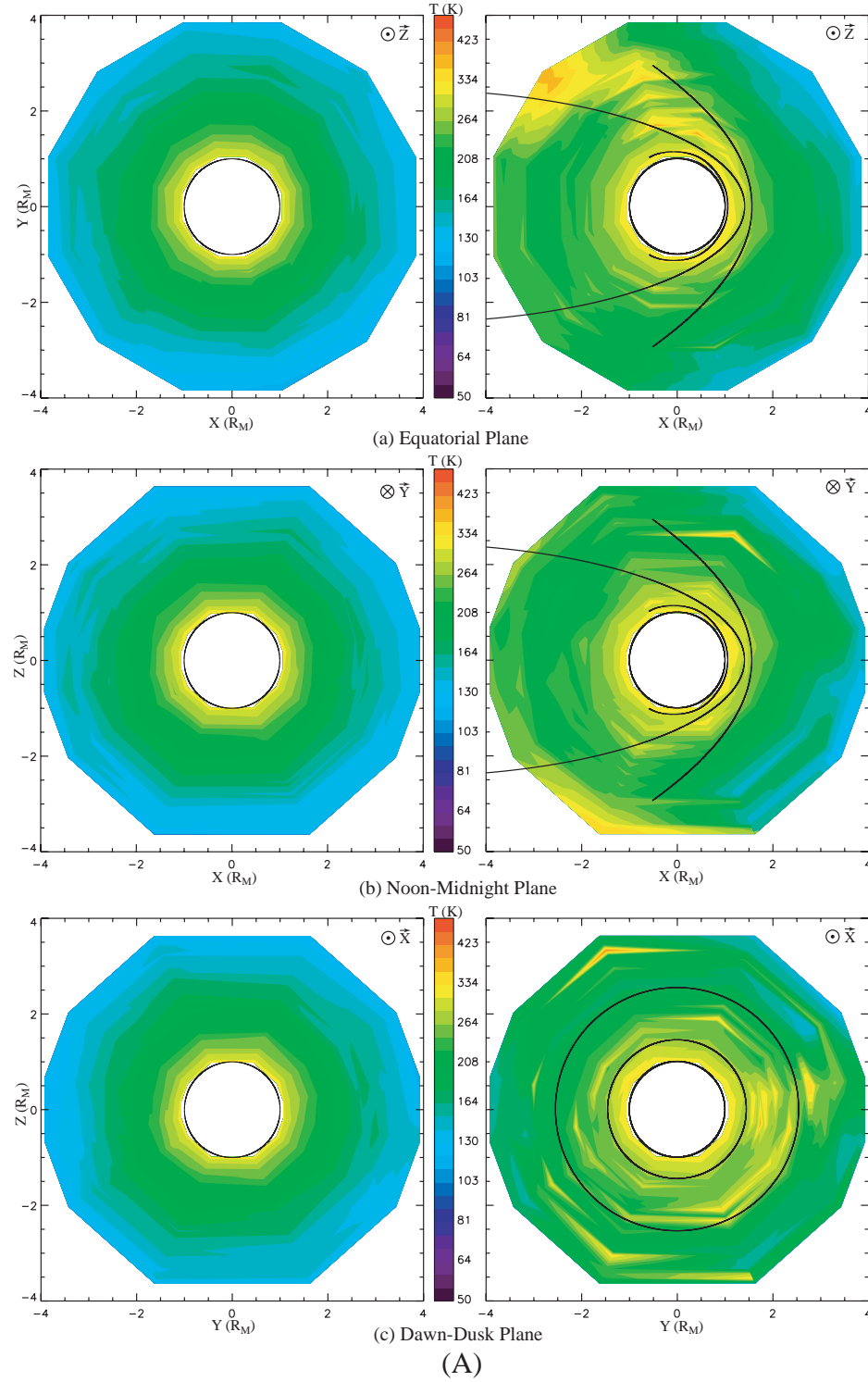


Figure 5.7 Exospheric temperature contours in equatorial (top row), noon-midnight (middle row) and dawn-dusk (bottom row) cuts. (A): collisionless primary exosphere (PRE, left column) and charge exchanged exosphere (CELSPE, right column). The Mars-Solar-Ecliptic coordinate system is used in each panel. (B): collisional primary exosphere (PREO, left) and charge exchanged exosphere (CELSPEO, right).

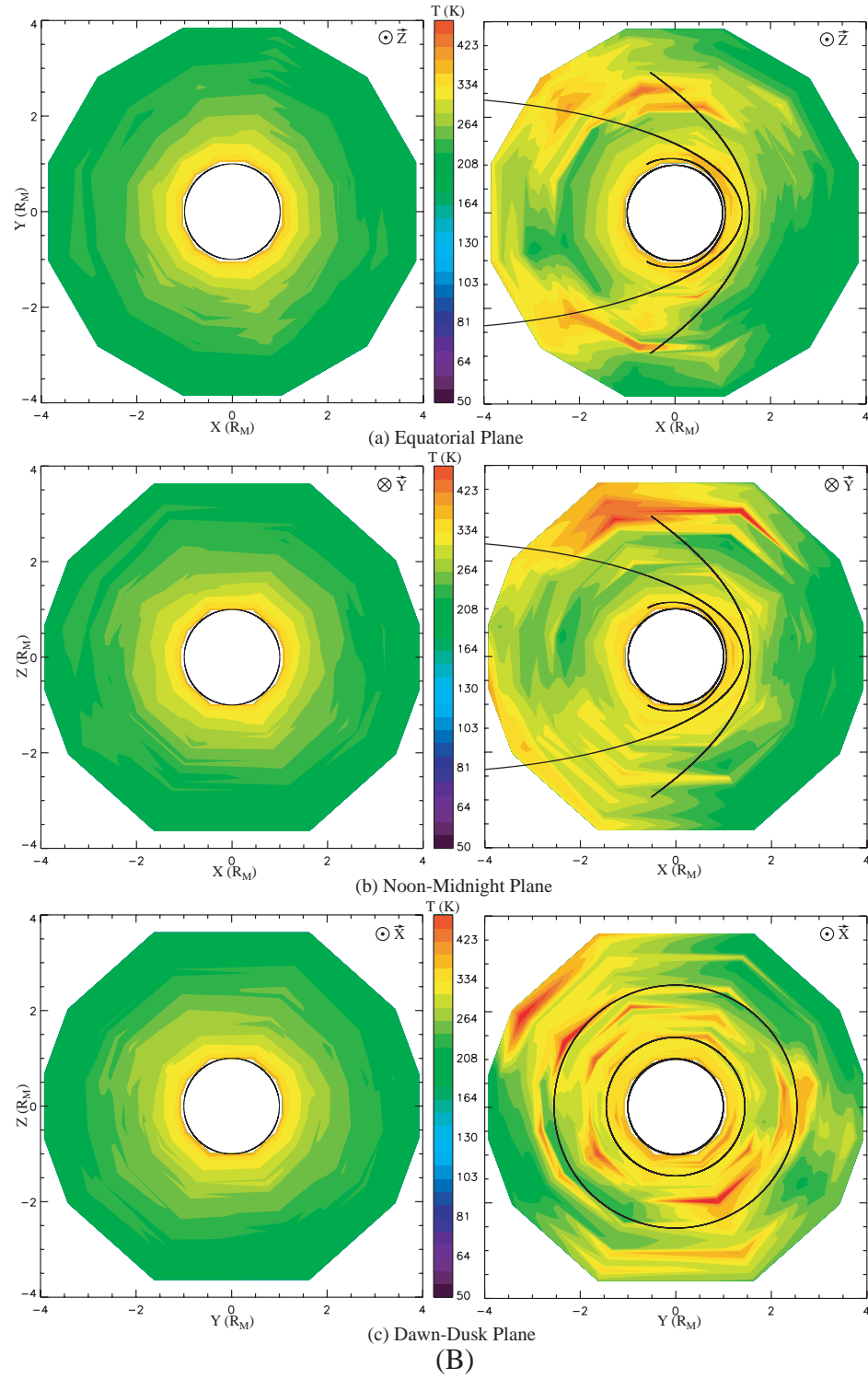


Figure 5.7 (continued)

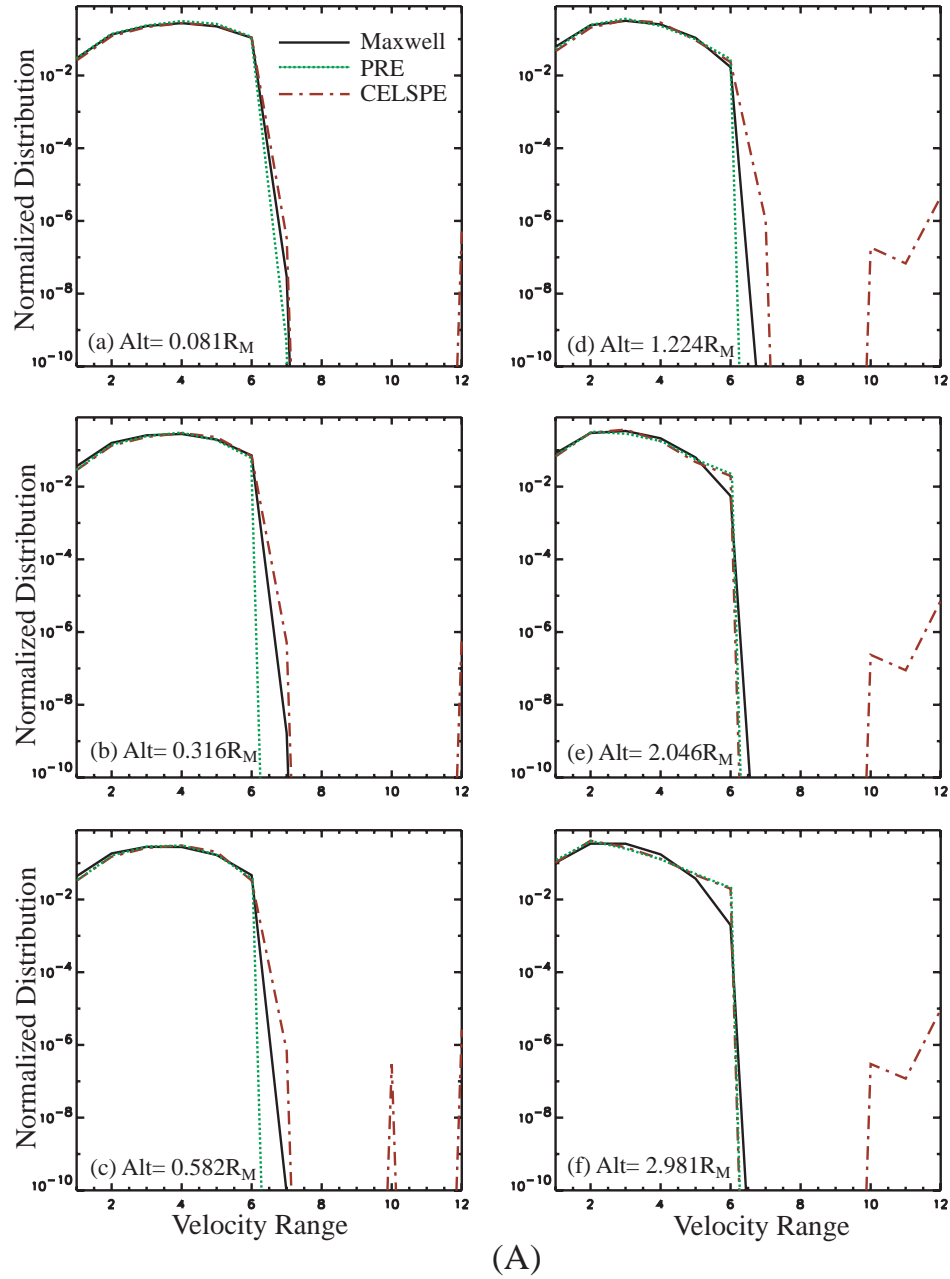


Figure 5.8 Exosphere normalized distribution functions at six different altitudes for three cases. (A): theoretical isotropic Maxwellian distribution (Maxwell, in black), collisionless primary exosphere (PRE, in green), and charge exchanged exosphere (CELSPE, in brown). The area between the x-axis and each curve should be one unit. Note the velocity range represented by each integer point on x-axis can be checked in table 1. (B): collisional primary exosphere (PREO, in green) and charge exchanged exosphere (CELSPEO, in brown).

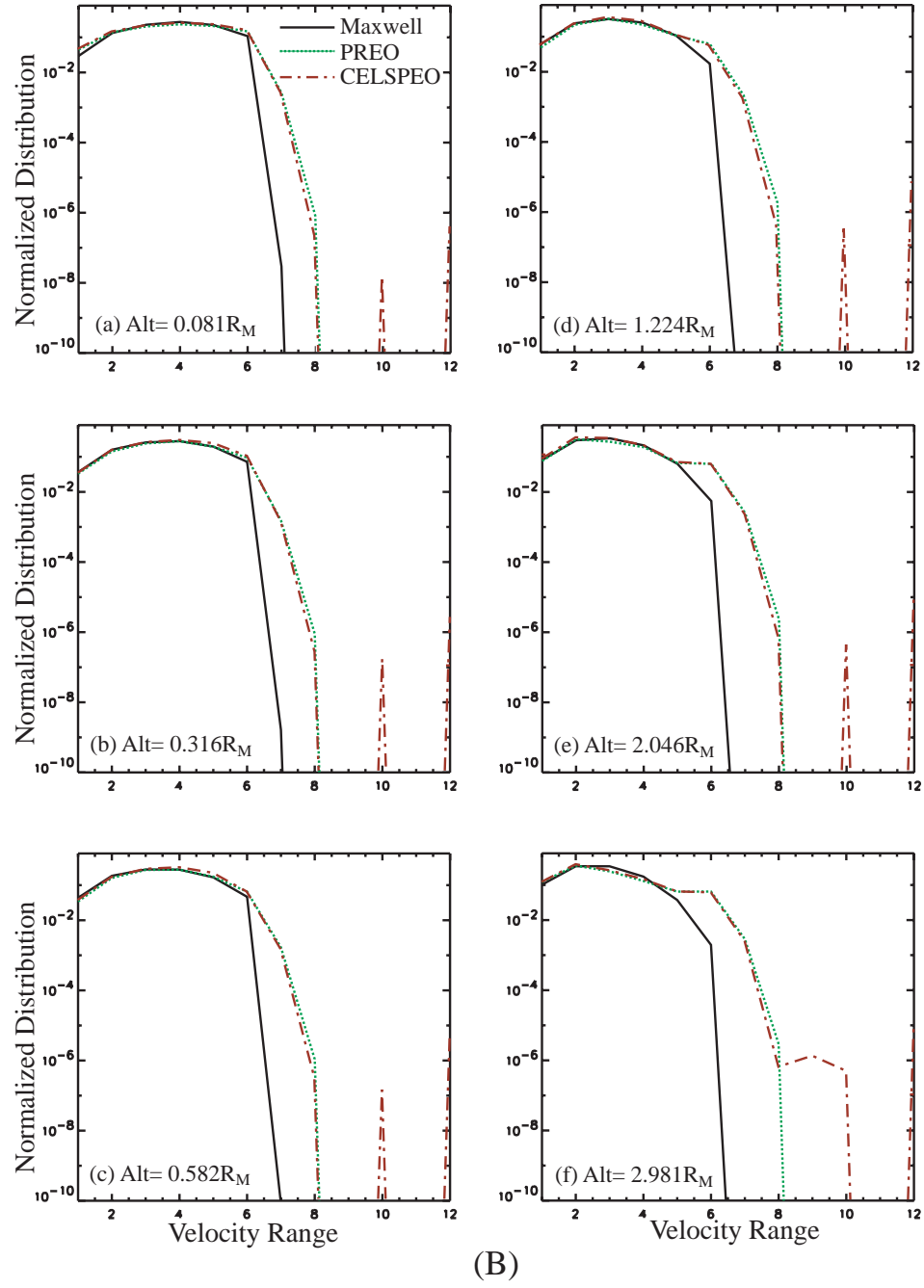


Figure 5.8 (continued)

Table 5.3.2 Velocity range used in Figure 5.8

Integer Point	1	2	3	4	5	6	7	8	9	10	11	12
Velocity Range (km/s)	(0, 0.8]	(0.8, 1.5]	(1.5, 2.2]	(2.2, 3]	(3, 4]	(4, 10]	(10, 50]	(50, 80]	(80, 110]	(110, 150]	(150, 160]	(160, ∞)

6. Discussions

So far we have shown our models' outputs in sections 4 and 5, next we would like to discuss further their implications for other research. In section 6.1, we show the importance of including the effects of charge exchange in the study of solar wind interaction with Mars and the evolution of the Martian atmosphere. Then in section 6.2 we compare the role of solar wind originated hot H component with the ionosphere originated part and make a prediction for the future observation.

6.1 Effects of Charge Exchange on Solar Wind

The ability of our simple model, the FMII in section 4.3, of the solar wind CE with the Martian exosphere to reproduce the observed steep increase of the magnetic field in MPB convinces us that that model represents the underlying physics of the MPB. That is, it has been shown that the charge exchange of the solar wind protons with the neutral exosphere—especially the H exosphere—constituents plays a crucial role in the formation of the MPB. The magnetic field pressure increases to compensate for the loss of the thermal pressure of the shock-compressed solar wind by CE.

Furthermore, although probably not the dominant mechanism, the CE systematically erodes the neutral exosphere prominently. On one hand, after the interaction $H+H^+ \rightarrow H^++H$, newly born H has a high probability to escape from Mars because of its very high thermal speed ($\sim 200\text{km/s}$, $\gg 5\text{km/s}$) while the newly born H^+ is picked up by the solar wind and lost to space also, and the loss rate of H can be estimated to be of the order of magnitude $10^{25}/\text{s}$ with the solar wind parameters in our model. On the other hand, after the interaction $O+H^+ \rightarrow O^++H$, O^+ and H are lost in the same manner as described above, but the loss contribution from this reaction is much smaller ($\sim 10^{23}/\text{s}$;

the observed total oxygen loss rate by direct solar wind pickup is $8 \times 10^{22} \sim 4 \times 10^{23}/s$ [Luhmann and Bauer, 1992]). In short, the neutral Martian exosphere can be eroded through the charge exchange interactions and the calculation of the CE rates implies that the history of the Martian atmosphere depends in part on those loss rates.

Finally, this model also provides us with a good basis to build a better model to simulate the interaction between the Martian exosphere and solar wind. Our present model reveals the physics of the MPB but is not self-consistent. To improve it, we need apply MHD equations with CE to solar wind-Mars interaction. Additionally, in order to quantitatively estimate the effects of electrons and the movement of protons sliding along the magnetic field lines, more computation is needed.

6.2 Effects of Charge Exchange on Martian H Exosphere

In order to evaluate the role of the solar wind originated hot H component, we are going to discuss two things next. The first is to estimate the structure of the ionosphere originated hot H component, and the second is to find a way to prove the existence of the calculated solar wind originated hot H component, as requiring the Lyman α radiation observation.

6.2.1 Ionosphere-originated hot H Exosphere Component

In this part a rough estimate of the Martian ionosphere-originated hot H exosphere is made by a comparative study of the Venus case.

It's well known that dual thermal- and hot- exospheres exist on Venus. The hot H exosphere was firstly discovered by the Lyman α scattering experiment onboard Martian 5. The observation is fitted perfectly in the simulation done by Anderson [1976], whose exosphere model includes two components: one with $T_c = 275K$, $N_c = 2 \times 10^5 cm^{-3}$ and

the other with $T_c = 1025K$, $N_c = 1.3 \times 10^3 cm^{-3}$. The research followed has indicated that one main source of the Venusian hot H exosphere, especially on the nightside, is the charge exchanges between the hot ionospheric H^+ and thermal exosphere constituents



[Hodges and Tinsley, 1981; Hunten, 1982], and the reactions between the H_2 and O^+ as well as CO_2^+ in ionosphere can be the major source of the hot hydrogen, too [Cravens et al., 1980]. Due to the low temperature at Venus exobase and strong gravity field this hot H exosphere should play important role in the escape and evolution of Venus atmosphere.

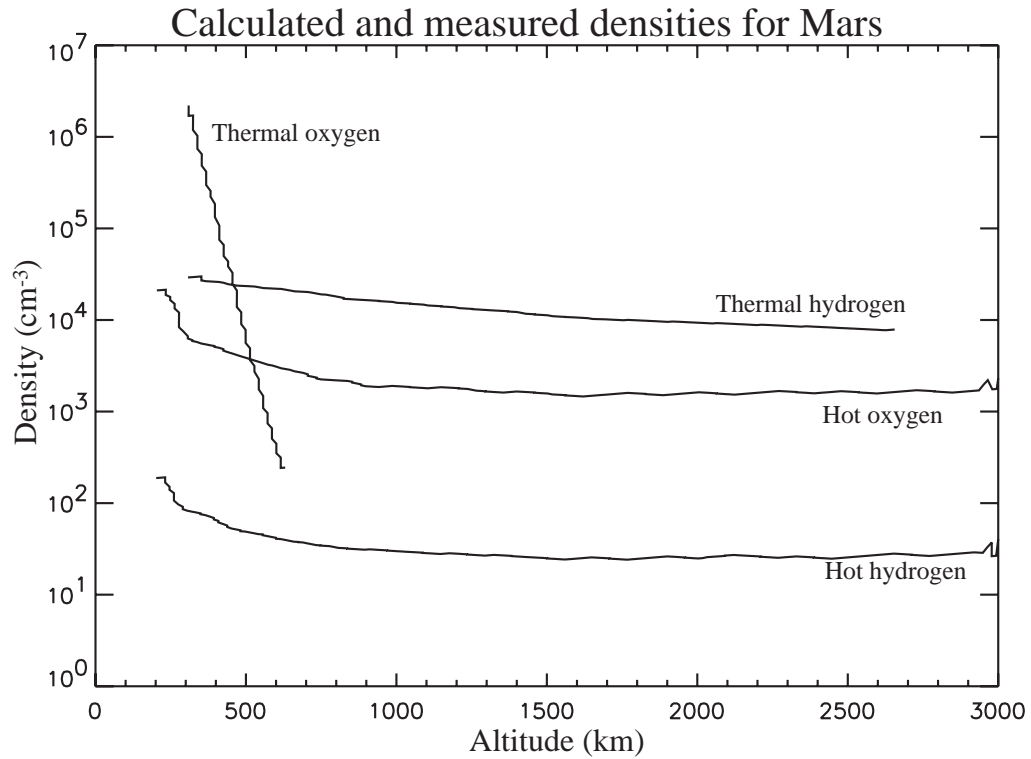


Figure 6.1 Calculated hot hydrogen and oxygen densities for Mars. The hot atom calculations were carried out using the two-stream approach. Observed thermal oxygen and hydrogen densities are also shown for comparison (reproduced from Nagy et al. [1990]).

From the similarity between Venus and Mars, we reasonably expect the same mechanism to be valid in the Martian case. However, to my knowledge, for some unknown reason there is no complete calculation on this topic except for the one Nagy et al. mentioned in their review paper [1990]. Nagy et al. presented the curve that should come from a two-stream model but the problem is no details of that model have ever been given. Anyhow we reproduce that plot here, as in figure 6.1, and we can see that the ratio of the hot and thermal densities is around a thousandth and we will prove it next.

In the following, we present our result by a simplified two-stream model which gives the structure of the ionosphere-originated hot H exosphere. The calculation of this model is carried out only in the ‘source region’ which ranges from the exobase (~200km) up to 2500km and is the place, we assume, all hot H is produced. Assuming the hot constituent is produced by (6.2.1) and (6.2.2) and lost by thermal escape and reaction



when the equilibrium is reached we have the governing equations from the continuity theorem

$$\frac{d\phi^+}{dz} + \phi^+ (2n_{O^+}\sigma_3) = (n_H\sigma_1 + n_O\sigma_2)n_{H^+}v \quad (6.2.4)$$

$$\frac{d\phi^-}{dz} - \phi^- (2n_{O^+}\sigma_3) = -(n_H\sigma_1 + n_O\sigma_2)n_{H^+}v \quad (6.2.5)$$

which are actually two-stream equations [Cravens et al., 1980] simplified by no consideration of particles’ energy cascade, and here $\phi^+(z)$ and $\phi^-(z)$ are the upward and downward directed hot hydrogen flux, respectively; σ_1 , σ_2 and σ_3 are cross sections of reactions (6.2.1), (6.2.2) and (6.2.3); v is the bulk speed of the flux and we take it being constant with a values of 7km/s (thermal speed of H at ~3000K); n_H and n_O are the

density profiles of H and O which are the same as those given in section 4 (figure 4.2), while the density profiles of relevant ionosphere constituents (n_{H^+}, n_{O^+}) can be found in the figure 9 of Barth et al. [1992] and we approximate them by taking constant values $50cm^{-3}$ and $200cm^{-3}$ all over the calculation domain. Next two boundary conditions, somewhat artificial but reasonable, are given as $\phi^- = 15\%\phi^+$ at the exobase and $\phi^- = 10\%\phi^+$ at 2500km by considering the escaping part. Then by solving (6.2.4) and (6.2.5) we obtain

$$n_H^{hot} = \frac{\phi^+ + \phi^-}{v} \sim 2 \times 10^2 (cm^{-3}) \exp[-5 \times 10^{-6} r(km)] \quad (6.2.6)$$

which is almost constant in the calculation domain because the effect of loss by reaction (6.2.3) is pretty weak. From this calculation, the ratio of hot and thermal hydrogen at 2000km is $\sim 1 \times 10^{-3}$, which has the same order of magnitude as that in figure 6.1 (from Nagy et al. [1990]). According to our assumption, beyond 2500km, the vertical distribution of this hot component would be controlled by gravity field instead and should have a much smaller scale height, like $\sim 1.4 \times 10^4 km$ with temperature 2000K at 2500km, so that the ratio of the hot and thermal hydrogen is larger than 4×10^{-3} at $1.5 R_M$.

Therefore from the perspective of density, the ionosphere-originated hot hydrogen is more prominent than the solar-wind-originated part. A particle detector onboard a spacecraft is more likely to ‘see’ the former component. Then our question is how to prove the existence of the solar-wind-originated part? This question can be answered by the estimate we presented in section 5.1, in which we assert that the solar wind originated hot hydrogen can double the kinetic temperature of ‘primary exosphere’. Similarly, the contribution of the ionosphere-originated part is negligible ($\sim 10^{-2}$ by $\frac{n_H^{hot}}{n_H} \sim 10^{-3}$ and

$\frac{T_H^{hot}}{T_H} < 10$) comparing to that in (5.1.8). It means the solar wind originated hot hydrogen can be detected by observing the thermal structure of the exosphere, as is relevant to the Lyman α scattering observation which we leave to the next subsection.

6.2.2 Lyman α airglow

The observation of Martian Lyman alpha radiation, which is important to determine the atomic-hydrogen distribution in planetary atmosphere, has been carried out by American Mariner 6, 7, and 9 as well as USSR Mars 2 and 3 from the 1960's to 1970's. The observed intensity of Lyman α by Mariner 6 and 7 ranges from 4-7kR (here 1 rayleigh equals to $10^6 \text{ photos} \cdot \text{cm}^{-2} \cdot \text{s}^{-1}$) while the ones obtained by Mariner 9 and Mars 2, 3 in the winter of 1971 are somewhat bigger. Analysis of data indicates that Mars has a hydrogen exosphere with exobase temperature $\sim 350\text{K}$ and number density $\sim 3 \pm 1 \times 10^4 \text{ cm}^{-3}$ at altitude 250km by Anderson and Hord [1971] and Anderson [1974], while Dementyeva et al. [1972] employed the same radiative theory to obtain a same temperature and a smaller critical density $\sim 6 \times 10^3 \text{ cm}^{-3}$. In figure 6.2 we present the spectral information obtained from the observations by Anderson and Hord [1971].

As shown in papers mentioned herein, for a given exosphere model, we need to employ the radiative theory in order to simulate the observed Lyman α radiation. That is, we need to solve the radiative transfer equation in optically thick medium

$$4\pi f = F \int_0^{\tau(R, R_b)} S(R') T[\tau(R, R')] d\tau(R, R') \quad (6.2.7)$$

Here $\tau(R, R')$ is the optical depth which can be obtained by integrating the scattering cross section timing number density from observation point R to point R' along the line of sight. Transmission function is given by

$$T(t) = \frac{2}{\sqrt{\pi}} \int_0^\infty \exp[-\alpha(x)t] \alpha(x) dx \quad (6.2.8)$$

where the Doppler broadening function is $\alpha(x) = \exp(-x^2)$ and $x = (\nu - \nu_0)/\Delta\nu_D$ is the frequency shift from line center ν_0 measured in Doppler widths [Anderson and Hord, 1971]. F is the solar flux and can be given by $(\pi F_{\nu_0}) \Delta\nu_D \sqrt{\pi}$ and here πF_{ν_0} is the spectral density of emission at Lyman α line center. The R_b is the vector locating on one of the boundary sphere. The $S(R)$ is the source function which shows the rate of atomic hydrogen excitation at point R by Lyman α quanta integrated over the absorption line and actually obtaining R is the core of the whole simulation problem.

Although solving (6.2.7) by including the solar-wind-originated and ionosphere-originated hot hydrogen exosphere is far beyond the scope of this dissertation, a rough estimate of their contributions to Lyman α radiation would be enlightening. We all know that the exosphere density plays a crucial role in determination of the radiation intensity. In the simplest case when single scattering applies, we know that the intensity is proportional to the column density. From our discussion in section 6.2.1 and 5.1, the Lyman α radiation from ionosphere originated hot H shouldn't exceed 100R and that from the solar wind originated part would be even smaller. Such intensity is smaller than the background radiation ($\sim 300R$ from Barth et al. [1972]) and very hard to detect. That may explain why none of previous spacecrafts have "seen" the Martian hot H exosphere. However, the Doppler broadening effects may unveil the existence of those hot components. The nature Doppler broadening by the thermal exosphere (350K) is only $\sim 0.01\text{\AA}$, the ionosphere originated hot part can extend the width to $\sim 0.1\text{\AA}$ which is still too small to be seen. The solar wind originated hot H has a bulk velocity $\sim 100\text{--}400\text{km/s}$

which can broaden the spectra line to 0.5-2 Å plus the high temperature of this part ($\sim 2 \times 10^6$ K) can further broaden the line ~ 1 Å. Such a large broadening should be observable to experiment onboard future Martian flights, such as the SPICAM onboard Mars Express (arranged to arrive at the end of 2003) and UVS onboard NOZOMI (arranged to arrive in 2003-2004 but failed recently). It's worthy of mention that actually such broadening may have been observed by Mariner 6 a long time ago but to my knowledge, maybe because of the 10 Å resolution of the instrument, no one has ever questioned such a width of the observed spectral line as shown in figure 6.2!

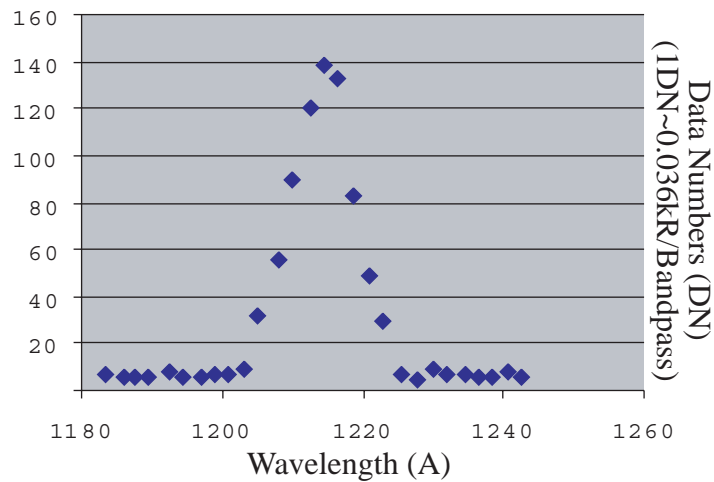


Figure 6.2 Average of 10 Mariner 6 Lyman α spectra near the bright limb (reproduced from Anderson and Hord [1971]).

7. Conclusions

In this dissertation, a detailed analysis demonstrates that charge exchange of solar wind with Martian exosphere plays an important role in the Mars-solar wind interaction. It has been revealed that charge exchange has two-fold consequences on both the shocked solar wind near Mars and the profiles of the Martian hydrogen exosphere, as have been studied by models and explicated in previous sections.

7.1 Summary of Results

On one hand, the rapid field increase in the Mars pile-up boundary (MPB), which has been indicated by both the MAG and ER data onboard Mars Global Surveyor, is larger than the prediction made by the Spreiter and Stahara gas-dynamic model [1980], as implies the involvement of other physical factors. Both the success of the model of Crider et al. [2000], which successfully explain the observed ER data in MPB, and the consideration of pressure partition leads to the idea that part of the solar wind thermal pressure may be lost by the charge exchange with the Mars exospheres and in order to compensate for the loss of thermal pressure the magnetic field pressure must increase. To test this idea, we constructed the fluid model in this dissertation and compared the model results with the MGS observations, which fit with each other quite well. Therefore, it is demonstrated that charge exchange is crucial to explain the formation of Martian MPB, therefore it plays an important role in the solar wind-Mars interaction.

Besides, the loss of both Martian hydrogen and oxygen exosphere is enhanced due to the characteristics of the charge exchange interactions. The loss rates due the CE have been estimated to be $\sim 10^{25}/\text{s}$ and $\sim 10^{23}/\text{s}$ for H and O, respectively, which are

significant contribution to the total loss of Martian atmosphere. Therefore, the charge exchange is important to the history of the Martian atmosphere, too.

On the other hand, the structure of Martian exosphere is affected simultaneously by the charge exchange also. Compared to Venus, Mars has an ionosphere that is so dilute that charge exchange of solar wind should play some role in the formation of nonthermal Martian hydrogen exosphere component, and the more important part is that the high speed and high temperature of the solar wind originated hot hydrogen part may make a noticeable change the thermal structure of Martian exosphere with a relative small amount. In order to study quantitatively how the Martian exosphere is influenced by it, we developed a 3-dimensional Monte Carlo exosphere model in which effects of the charge exchange with solar wind are isolated and studied. Simulation results show the existence of that hot population does alter the exospheric thermal structure greatly by almost doubling the temperature and destroying the spherical symmetry at high altitude. Moreover we investigate our simulation results by calculating the contribution of that hot component to Ly- α emission and compare it with data acquired by Mariners' ultraviolet spectrometers.

Also, from the Monte Carlo models we establish that the Lyman scattering and the presence of background O exosphere can change the density and radial velocity profiles of the hydrogen exosphere, while the self-rotation of the planet has few effects on the structure of hydrogen exosphere.

Finally, we conclude that the charge exchange is important in interaction between solar wind and Martian exosphere and output of our models can be used to aid modeling and data analysis for future Mars missions.

7.2 Future work and Prospects

Combined with the model by Crider et al. [2000], our fluid model and the Monte Carlo models clarify what processes are going on in the Martian MPB and exosphere. From here, the next step to understand more about the magnetic pile-up boundary and exosphere is to collect and analyze more data. Mars express, which is to be launched in 2003, carried both EM and neutral particle instruments onboard. If we are lucky enough, we could have a wealth of data very soon.

For the exosphere, in this work we focus on the charge exchange between solar wind protons and Martian exospheric hydrogen atoms. There exist other neutral atoms, like O in exosphere, that can react with solar wind protons directly or indirectly. So if we want to understand how the solar wind affects the exosphere and upper atmosphere of Mars we need to include more reactions into the picture. Moreover, other physical factor, such as an uneven exobase temperature distribution that can lead to lateral flow, may change the condition of the exosphere, too.

For the Martian magnetic pileup boundary this work provides an explanation for its formation. This work also is applicable to comets, whose comas, evaporated gases expanding as approaching the Sun, should interact with the solar wind by charge exchange, too.

Finally, part of the energetic particles produced by charge exchange can travel downward and bombard the lower atmosphere and affect the formation of the Martian ionosphere. Some studies on this topic have begun (e.g., Kallio and Barabash [2001] and Haider et al. [2002]) but the agreement between the results has not been achieved yet, and

further theoretical efforts are still needed with the approaching launch date of the Mars Express.

References

- Aamodt, R.E., and K.M. Case, Density in a simple of the exosphere, *Phys. Fluids*, **5**, 1019, 1962
- Acuña, M.H., J.E.P. Connerney, P. Wasilewski, R.P.Lin, K.A. Anderson, C.W. Carlson, J. Mcfadden, D.W. Curtis, H. Reme, A. Cros, J.L. Medale, J.A. Sauvaud, C. d'Uston, S.J. Bauer, P. Cloutier, M. Mayhew, and N.F. Ness, Mars observer magnetic fields investigation, *J. Geophys. Res.*, **97**, 7799-7814, 1992
- Acuña, M.H., J.E.P. Connerney, P. Wasilewski, R.P. Lin, K.A. Anderson, C.W. Carlson, J. Mcfadden, D.W. Curtis, D. Mitchell, H. Rème, C. Mazelle, J.A. Sauvaud, C. d'Uston, A. Cros, J.L. Medale, S. J. Bauer, P. Cloutier, M. Mayhew, D. Winterhalter, and N.F. Ness. Magnetic field and plasma observations at Mars: Initial results of the Mars Global Surveyor Mission, *Science*, **279**, 1676-1680, 1998
- Acuña, M.H., J.E.P. Connerney, N.F. Ness, R.P. Lin, D. Mitchell, C.W. Carlson, J. Mcfadden, K.A. Anderson, H. Rème, C. Mazelle, D. Vignes, P. Wasilewski, and P. Cloutier, Global distribution of crustal magnetism discovered by the Mars Global surveyor MAG/ER experiment, *Science*, **284**, 790-793 1999
- Albee, A., R.E. Arvidson, F. Palluconi and T. Thomas, Overview of the Mars Global Surveyor mission, *J. Geophys. Res.*, **106**, 23291-23,316, 2001
- Alksne, Alberta Y., and D.L. Webster. Magnetic and Electric Fields in the Magnetosheath, *Planet. Space Sci.*, **18**, 1203-1212, 1970
- Anderson, D.E., and C.W. Hord, Mariner 6 and 7 Ultraviolet spectrometer experiment: Analysis of Hydrogen Lyman-Alpha data, *J. Geophys. Res.*, **76**, 6666-6673, 1971
- Anderson, D.E., Mariner 6, 7 and 9 Ultraviolet spectrometer experiment: Analysis of Hydrogen Lyman-Alpha data, *J. Geophys. Res.*, **79**, 1513-1518, 1974
- Anderson, D.E., The Mariner 5 ultraviolet photometer experiment: Analysis of hydrogen Lyman alpha data, *J. Geophys. Res.*, **81**, 1213, 1976
- Banks, P.M., and G. Kockarts, *Aeronomy*, Academic, Orlanso, Fla., 1973
- Barth, C.A., Tutorial survey paper: Planets, Moons, and Comets, *J. Astronaut. Sci.*, **32**, 1-16, 1984
- Barth, C.A., A.I.F. Steward, S.W. Bougher, D.M. Hunten, S.J. Bauer, and A.F. Nagy, Aeronomy of the current Martian atmosphere, *Mars*, 1054-1089, The University of Arizona press, Tucson & London, 1992

- Bauske, R., A.F. Nagy, T.I. Gombosi, D.L. DeZeeuw, K.G. Powell, and J.G. Luhmann. A three-dimensional MHD study of solar wind mass loading processes at Venus: Effects of photoionization, electron impact ionization, and charge exchange, *J. Geophys. Res.*, **103**, 23625-23638, 1998
- Brinkmann, R.T., Departure from Jeans escape rate for H and He in the earth's atmosphere, *Planet. Space Sci.*, **18**, 449, 1970
- Chamberlain, J.W., Planetary coronae and atmospheric evaporation, *Planet. Space Sci.*, **11**, 901-960, 1963
- Chamberlain, J.W., and F.J. Campbell, Rate of evaporation of a non-Maxwellian atmosphere, *Astrophys. J.*, **149**, 687, 1967
- Chamberlain, J.W., and G.R. Smith, Comments on the rate of evaporation of a non-Maxwellian atmosphere, *Planet. Space Sci.*, **19**, 675, 1971
- Chamberlain, J.W., and D.M. Hunten, Theory of planetary atmospheres: An introduction to their physics and chemistry, *International geophysics series*, **Vol. 36**, Academic Press, Inc., 1987
- Chen, Y., P. A. Cloutier, D. H. Crider, C. Mazelle, and H. Rème, On the role of charge exchange in the formation of the Martian magnetic pileup boundary, *J. Geophys. Res.*, **106**, 29,387, 2001
- Cloutier, P.A., Y. Chen, D.H. Crider, C.C. Law, P.W. Walker, M.H. Acuña, J.E.P. Connerney, R.P. Lin, K.A. Anderson, D.L. Mitchell, C.W. Carlson, J. Mcfadden, D.A. Brain, H. Rème, C. Mazelle, J.A. Sauvaud, C. d'Uston, D. Vignes, S.J. Bauer, and N.F. Ness. Venus-like interaction of the solar wind with Mars, *Geophys. Res. Lett.*, **26**, 2685-2688, 1999
- Coates, A.J., Ionosoheres and magnetospheres of comets, *Adv. Space Res.*, **20**, 2, 255-266, 1997
- Connerney, J. E. P., M. H. Acuña, P. Wasilewski, N. F. Ness, H. Rème, C. Mazelle, D. Vignes, R. P. Lin, D. Mitchell, and P. Cloutier, Magnetic lineations in the ancient crust of Mars, *Science*, **284**, 541, 794-798, 1999.
- Connerney, J. E. P., M. H. Acuña, P. J. Wasilewski, G. Kletetschka, N. F. Ness, H. Rème, R. P. Lin, D. L. Mitchell, The global magnetic field of Mars and implications for crustal evolution, *Geophys. Res. Lett.*, **28**, 4015-4018, 2001
- Cravens, T.E., T.I. Gombosi, and A.F. Nagy, Hot hydrogen in the exosphere of Venus, *Nature*, **283**, 178-180, 1980

- Cravens, T.E., The solar wind interaction with non-magnetic bodies and the role of small-scale structures, *Solar System Plasma Physics*, **Geophysical Monograph 54**, 353-366, 1989
- Crider, D.H., Evidence of electron impact ionization in the magnetic pileup boundary of Mars: Observation and Modeling Results, *Ph.D. dissertation*, Department of Space physics and Astronomy, Rice Univ., 1999
- Crider, D., P. cloutier, C. Law, P. Walker, Y. Chen, M.H. Acuña, J. Connerney, D. Mitchell, R. Lin, K. Anderson, C. Carlson, J. McFadden, H. Rème, C. Mazelle, C. d'Uston, J. Sauvaud, D. Vignes, D. Brain, and N. Ness. Evidence of electron impact ionization in the magnetic pileup boundary of Mars, *Geophys. Res. Lett.*, **27**, 45-48, 2000
- Curtis, S.A., and R.E. Hartle, Mercury's helium exosphere after Mariner 10's third encounter, *J. Geophys. Res.*, **83**, 1551, 1978
- Curtis, S.A., and N.F. Ness, Remanent magnetism at Mars, *Geophys. Res. Lett.*, **15**, 7373-739, 1988
- Dementyeva, N.N., V.G. Kurt, A.S. Smirnov, L.G. Titarchuk, and S.D. Chuvahin, Preliminary results of measurements of UV emissions scattered in the Martian upper atmosphere, *Icarus*, **17**, 475-483, 1972
- Donahue, T.M., J.H. Hoffman, R.R. Hodges, and A.J. Watson, Venus was wet: A measurement of the ratio of deuterium to hydrogen, *Science*, **216**, 630, 1982
- Fahr, H.J., and G. Paul, Exospheric velocity distribution functions and derived gas dynamical properties, *J. Atmos. Terr. Phys.*, **38**, 841, 1976
- Fahr, H.J., B. Shizgal, Modern exospheric theories and their observational relevance, *Rev. of Geophys. Space Phys.*, **21**, 75-124, 1983
- Fite, W.L., R.F. Stebbings, D.G. Hummer, and R.T. Brackmann. Ionization and charge transfer in proton-hydrogen atom collision, *Phy. Review*, **119**, 663-668, 1960
- Hagenbuch, K.M., and R.E. Hartle, Simple model for a rotating neutral planetary exosphere, *Phys. Fluids*, **12**, 1551, 1969
- Haider, S.A., S.P. Seth, E. Kalio, and K.I. Oyama, Solar EUV and electron-proton-hydrogen atom-produce ionosphere on Mars: Comparative studies if particle fluxes and ion production Rates due to different processes, *Icarus*, **159**, to be published, 2002
- Hays, P.B., and V.C. Liu, On the loss of gases from a planetary atmosphere, *Planet. Space Sci.*, **13**, 1185, 1965

- Herring, J. and L. Kyle, Density in a planetary exosphere, *J. Geophys. Res.*, **66**, 1980, 1961
- Hodges, R.R., and Tinsley, B.A., Charge exchange in the Venus ionosphere as the source of the hot exospheric hydrogen, *J. Geophys. Res.*, **86**, 7649-7656, 1981
- Hodges, R.R., Monte Carlo simulation of the terrestrial hydrogen exosphere, *J. Geophys. Res.*, **99**, 23,229-23,247, 1994
- Hunten, D.M., Thermal and nonthermal escape mechanism for terrestrial planet, *Planet. Space Sci.*, **30**, 773, 1982
- Hunten, D.M., Kuiper prize lecture: escape of atmospheres, ancient and modern, *Icarus*, **85**, 1-20, 1990
- Ip, W.H., On the hot oxygen corona of Mars, *Icarus*, **76**, 135-145, 1988
- Ip, w.H., The fast atomic oxygen corona extent of Mars, *Geophys. Res. Let.*, **17**, 2289, 2292, 1990
- Jeans, J.H., *The dynamical theory of gases*, 4th ed., Cambridge Univ. Press, New York, 1925
- Johnson, F.S., and R.A. Fish, The telluric hydrogen corona, *Astrophys. J.*, **131**, 502, 1960
- Johnson, F.S., The distribution of hydrogen in the telluric hydrogen corona, *Astrophys. J.*, **133**, 701, 1961
- Kallio, E.. An empirical model of the solar wind flow around Mars, *J. Geophys. Res.*, **101**, 11133-11147, 1996
- Kallio, E., J.G. Luhmann, and S. Barabash. Charge exchange near Mars: The solar wind absorption and energetic neutral atom production, *J. Geophys. Res.*, **102**, 22183-22197, 1997
- Kallio, E., J.G. Luhmann, and J.G. Lyon, Magnetic field near Venus: A comparison between Pioneer Venus Orbiter magnetic field observations and an MHD simulation, *J. Geophys. Res.*, **103**, 4727-4737, 1998
- Kallio, E., and S. Barabash, Atmospheric effects of precipitating energetic hydrogen atoms on the Martian atmosphere, *J. Geophys. Res.*, **106**, 165-177, 2001
- Kerzhanovich, V.V., Mars 6: Improved analysis of the descent module measurements, *Icarus*, **30**, 1-25, 1977

- Law, C., Currents and magnetic field structures in the dayside solar wind interaction with Venus and Mars, *Ph.D. dissertation*, Department of Space Physics and Astronomy, Rice Univ., 1995
- Lammer, H., and S. Bauer, Nonthermal atmospheric escape from Mars and Titan, *J. Geophys. Res.*, **96**, 1819-1825, 1991
- Leverington, D., New cosmic horizons: space astronomy from the V2 to the Hubble Space Telescope, *Cambridge University Press*, 2000
- Lew, S.K., and S.V. Venkateswaren, A study of hydrogen diffusion in earth's upper atmosphere near the critical level, *J. Atmos. Sci.*, **22**, 623, 1965
- Lewis, J.S., Physics and chemistry of the solar system, revised edition, Academic Press, Inc., 1995
- Lin, R.P., D.L. Mitchell, D.W. Curtis, K.A. Anderson, C.W., Carlson, J. Mcfadden, M.H. Acuna, L.L. Hood, and A. Binder, Lunar surface magnetic fields and their interaction with the solar wind: Results from Lunar Prospector, *Science*, **281**, 1480-1484, 1998
- Liu, Y., A.F. Nagy, C.P.T. Groth, D.L. DeZeuw, T.I. Gombosi, and K.G. Powell, 3D multi-fluid MHD studies of the solar wind interaction with Mars, *Geophys. Res. Lett.*, **26**, 2689-2692, 1999
- Liwshitz, M., and S.F. Singer, Thermal escape of neutral hydrogen and its distribution, *Planet. Space Sci.*, **14**, 541, 1966
- Luhmann, J.G., and J.U. Kozyra, Dayside pickup oxygen ion precipitation at Venus and Mars: Spatial distributions, energy deposition, and consequences, *J. Geophys. Res.*, **96**, 5457-5467, 1991
- Luhmann, J.G., C.T. Russel, L.H. Brace, and O.L. Vaisberg, The intrinsic magnetic field and solar wind interaction of Mars, *Mars*, 1090-1134, The University of Arizona press, Tucson & London, 1992
- Lundin, R., A. Zakharov, R. Pellinen, S.W. Barabasz, H. Borg, E.M. Dubinin, B. Hultqvist, H. Koskinen, I. Liede, and N. Pissarenko, ASPERA/Phobos measurements of the ion outflow from the Martian ionosphere, *Geophys. Res. Lett.*, **17**, 6, 873-876, 1990
- Ma, Y., A.F., Nagy, K.C., Hansen, T.I. Gombosi, and D.L., DeZeeuw, 3D, 3 species and MHD studies of the interaction of solar wind with Mars, **abstract #SM12A-0838**, AGU meeting 2001

- Magalhaes, J.A., J.T. Schofield, and A. Seiff, Results of the Mars Pathfinder atmospheric structure investigation, *J. Geophys. Res.*, **104**, 8943-8955, 1999
- Marov, M.Y., E.I. Shematovich, D.V., Bisikalo, and J.C. Gerard, Nonequilibrium processes in the planetary and cometary atmospheres: theory and applications, *Kluwer Academic Publishers*, 1997
- Mazelle, C., H. Rème, J.A. Sauvaud, C. d'Uston, C.W. Carlson, K.A. Anderson, D.W. Curtis, R.P. Lin, A. Korth, D.A. Mendis, F.M. Neubauer, K.H. Glassmeier, and J. Raeder, Analysis of suprathermal electron properties at the magnetic pile-up boundary of comet P/Halley, *Geophys. Res. Lett.*, **16**, 1035-1038, 1989
- McAfee, J.R., Lateral flow in the exosphere, *Planet. Space Sci.*, **15**, 599, 1967
- McElory, M.B., Mars: An envolving atmosphere, *Science*, **175**, 443, 1972
- Mitchell, D. L., R. P. Lin, D. Crider, C. Law, P. Walker, P. Cloutier, and M. H. Acuña, Solar wind interaction with Martian crustal magnetic anomalies, *30th Annual Lunar and Planetary Science Conference*, **abstract no. 2061**, 1999, Houston, TX
- Murawski, K., and R.S. Steinolfson, Numerical modeling of the solar wind interaction with Venus, *Planet. Space Sci.*, **44**, 243-252, 1996
- Nagy, A.F., J. Kim, and T.E. Craves, Hot hydrogen and oxygen atoms of in the upper atmosphere of Venus and Mars, *Ann. Geophys.*, **8**, 251-25, 1990
- Nanbu, K. Direct simulation scheme derived from the Boltzmann equation, I, Monocomponent gases, *J. Phys. Soc, Jpn.*, **49**, 2042, 1980a
- Nanbu, K. Direct simulation scheme derived from the Boltzmann equation, II, Multicomponent gases, *J. Phys. Soc, Jpn.*, **49**, 2050, 1980b
- Neubauer, F.M. Gitto magnetic-field results on the boundaries of the pile-up region and the magnetic cavity, *Astron. & Astrophys.*, **187**, 73-79, 1987
- Opik, E.J., and S.F. Singer, Distribution of density in a planetary exosphere, *Phys. Fluids*, **3**, 486, 1960
- Opik, E.J., and S.F. Singer, Distribution of density in a planetary exosphere, II, *Phys. Fluids*, **4**, 221, 1961
- Ritcher, E., H.J. Fahr, and H.U. Nass, The satellite particle exospheres of planets: Application to earth, *Planet. Space Sci.*, **27**, 1163, 1979
- Schofield, J.T., J.R. Barnes, D. Crisp, R.M. Haberle, S. Larsen, J.A. Magalhaes, J.R. Murphy, A. Seiff, and G. Wilson, The Mars Pathfinder atmospheric structure

- investigation/meteorology (ASI/MET) experiments, *Science*, **278**, 1752-1758, 1997
- Seiff, A., and D.B. Kirk, Structure of the atmosphere of Mars in summer at midlatitudes, *J. Geophys. Res.*, **82**, 4364-4378, 1977
- Shah, M.B., D.S. Elliott, and H.B. Gilbody, Pulsed cross-beam study of the ionization of atomic hydrogen by electron impact, *J. Phys. B*, **20**, 3501-3514, 1984
- Shizgal, B., and M.J. Lindenfeld, Further studies of non-Maxwellian effects associated with the thermal escape of a planetary atmosphere, *Planet. Space Sci.*, **28**, 159, 1980
- Shizgal, B., and M.J. Lindenfeld, A simple kinetic theory calculation of terrestrial atomic hydrogen escape fluxes induced by charge exchange collisions, *J. Geophys. Res.*, **87**, 853, 1982
- Shizgal, B.D., and G.G. Arkos, Nonthermal escape of the atmospheres of Venus, Earth and Mars, *Rev. of Geophys.*, **34**, 483-505, 1996
- Spreiter, J.R., A.L. Summers, and A.W. Rizzi. Solar wind flow past nonmagnetic planets—Venus and Mars, *Plan. Space Sci.*, **18**, 1281, 1970
- Spreiter, J.R., and S.S. Stahara. A new predictive model for determining solar wind-terrestrial planet interactions, *J. Geophys. Res.*, **85**, 6769, 1980
- Spreiter, J.R., and S.S. Stahara. Computer modeling of the solar wind interaction with Venus and Mars, *Venus and Mars: Atmospheres, Ionospheres, and Solar Wind Interactions*, J.G. Luhmann, M. Tatrallyay, and R.O. Pepin, eds. **Geophysical Monograph 66**, 345, 1992
- Stebbing, R.F., A.C. Smith, and H. Ehrhardt. Charge transfer between oxygen atoms and O^+ and H^+ ions, *J. Geophys. Res.*, **69**, 2349-2355, 1964
- Tanaka, T., and K. Murawski, Three dimensional MHD simulation of the solar wind interaction with the ionosphere of Venus: Results of two-component reacting plasma simulation, *J. Geophys. Res.*, **102**, 19805-19821, 1997
- Tanaka, T., Generation mechanisms for magnetosphere-ionosphere current systems deduced from a three-dimensional MHD simulation of the solar wind-magnetosphere-ionosphere coupling processes, *J. Geophys. Res.*, **100**, 12057-12074, 1995
- Thompson, W.R., M.R. Shah, and H.B. Gilbody, Single and double ionization of atomic oxygen by electron impact, *J. Physics B*: **28**, 1321-1330, 1995

- Tracadas, P.W., M.T. Zuber, F.G. Lemoine, and D.E. Smith, The Removal of Periodic Gravitational Perturbations from Mars Global Surveyor's Science Phasing Orbits Applied to the Study of the Martian Exosphere, *The Fifth International Conference on Mars*, Pasadena, California, **abstract no. 6193**, July 19-24, 1999
- Vidal-Madjar, A., and J.L. Bertaux, A calculated hydrogen distribution in the exosphere, *Planet. Space Sci.*, **20**, 1147, 1972
- Walker, P.W., Y. Chen, and P.A. Cloutier, Local and global ionospheric interaction models of Martian surface magnetic anomalies, *EOS Transactions AGU*, **80**, S240, 1999
- Wallis, M.K., Exospheric density and escape and escape fluxes of atomic isotopes on Venus and Mars, *Planet. Space Sci.*, **26**, 949, 1978
- Ziering, S.P, P.N. Hu, and M. Sheinblatt, Thermal escape problem II, Transition domain in spherical geometry, *Phys. Fluids*, **11**, 1327, 1968

Appendix: Missions to Mars

Here we talk a bit of the history. In following tableA1 we give out the whole list of Mars mission spacecrafts whose information are collected from books by [Lewis, 1997; Leverington, 2000; etc.], journal papers [Albee et al., 2001; and etc.], and online resources [like NASA, NSSDC, and etc.]. For each mission, the spacecraft name, the country of origin, the launch /arrival time (if applicable), the mission type and the periapsis altitude, as well as the relevant onboard instruments and a brief comment are listed. It is noticeable that after the domination of the United States and the Soviet Union for the more than 30 years, Japan and Europe joined the Mars exploration club after the Cold War since 1990's.

Table AI: Human Exploration of Mars (1960—2003)

Spacecraft Country	Date (MMDDYY) Launch Arrrival	Mission Periap.(km)	Onboard Instru.			Brief Remarks
			MFD ¹	CPD ²	NPD ³	
1960--1969**						
<u>Marsnik 1</u> USSR	10-10-60 N/A	Flyby N/A	_____	_____	_____	Failed to reach Earth Orbit
<u>Marsnik 2</u> USSR	10-14-60 N/A	Flyby/ N/A	_____	_____	_____	Failed to reach Earth Orbit
<u>Spunik 22</u> (1962BI1) USSR	10-24-62 N/A	Flyby N/A	_____	_____	_____	Failed to depart from low Earth orbit
<u>Mars1</u> USSR	11-01-62 N/A	Flyby N/A	_____	_____	_____	Communication lost in transit
<u>Spunk 24</u> (1962BX1) USSR	11-04-62 N/A	Flyby N/A	_____	_____	_____	Failed to depart from low Earth orbit
<u>Mariner 3</u> USA	11-05-64 N/A	Flyby N/A	_____	_____	_____	Failed to separate shroud and leave the rocket.
<u>Mariner 4</u> USA	11-28-64 07-14-65	Flyby 9,846	yes	yes	no	Successful! Measure atmosphere pressure by radio occultation experiment and retuning pictures of Mars surface.

(to be continued on the next page)

<u>Zond 2</u> USSR	11-30-64 N/A	Flyby N/A	_____	_____	_____	Communication lost in transit
<u>Zond 3</u> USSR	07-18-65 N/A	Flyby N/A	_____	_____	_____	Flew by the Moon as test of Mars spacecraft
<u>Mariner 6</u> USA	02-24-69 07-31-69	Flyby 3,431	no	no	UVS	Successful! Return 75 pictures and confirm observation by Mariner 4.
<u>Mariner 7</u> USA	03-27-69 08-05-69	Flyby ?	no	no	UVS	Successful! This spacecraft is identical to Mariner 6 and it returns 126 pictures.
<u>Mars 1969A</u> USSR	03-27-69 N/A	Orbiter N/A	_____	_____	_____	Launch failure.
<u>Mars 1969B</u> USSR	04-02-69 N/A	Orbiter N/A	_____	_____	_____	Launch failure.
1970--1979						
<u>Mariner 8</u> USA	05-08-71 N/A	Orbiter N/A	_____	_____	_____	Failed at launch
<u>Kosmos 419</u> USSR	05-10-71 N/A	Lander N/A	_____	_____	_____	Failed to depart from low Earth orbit
<u>Mars 2</u> USSR	05-19-71 11-27-71	Orbiter ? Lander 0	no	no	UVP LAS	First Mars orbiter; the lander crashed in landing; discover water vapor in atmosphere
<u>Mars 3</u> USSR	05-28-71 12-02-71	Orbiter ? Lander 0	no	no	UVP LAS	Orbiter succeeded but lander was lost after landing.
<u>Mariner 9</u> USA	05-30-71 11-14-71	Orbiter 1,398	no	?	yes	Successful! Orbital photographic mapper; discover water vapor in atmosphere.
<u>Mars 4</u> USSR	07-21-73 02-10-74	Orbiter ~2,200	_____	_____	_____	Failed to insert Mars orbit.
<u>Mars 5</u> USSR	07-25-73 02-12-74	Orbiter 1,755	yes	yes	UVP LAS	Successful! Measure surface temperature and structure of atmosphere, detect a weak magnetic field.
<u>Mars 6</u> USSR	08-05-73 03-12-74	Lander N/A	yes	yes	yes	Communication lost before landing.
<u>Mars 7</u> USSR	08-09-73 03-09-74	Lander ~1,300	yes	yes	yes	Missed Mars.
<u>Viking 1</u> USA	08-20-75 06-19-76	Orbiter 300 Lander 0	no	no	ASE UAMS	Both successful! Fetch Mars surface sample, measure the meteorology and deploy seismometer and more.
<u>Viking 2</u> USA	09-09-75 09-03-76	Orbiter 300 Lander 0	no	no	ASE UAMS	Both successful! Same as Viking 1.
1980--1989						
<u>Phobos1</u> USSR	07-07-88 N/A	Orbiter N/A	MAGMAS	TAUS ASPERA SOV. SLED		Lost on the way to Mars

(to be continued on the next page)

<u>Phobos2</u> USSR	07-12-88 03-27-89	Orbiter	FGM MAGMAS	TAUS SOV. SLED , etc.	MSU/ TASPI	Partially successful. Obtain data about Mars and Phobos.
1990--1999						
<u>Mars Observer</u> USA	09-22-92 N/A	Orbiter N/A	yes	no	yes	Communication lost en route to Mars
<u>Mars Global Surveyor</u> USA	11-06-96 09-11-97	Orbiter 175	MAG	ER	no	Successful! Detect the existence of Mars origin magnetic field for the first time
<u>Mars '96</u> CIS	11-16-96 N/A	Orbiter N/A	?	yes	yes	Failed to insert Mars cruise trajectory.
<u>Pathfinder</u> USA	12-02-96 07-04-97	Land- rover 0	no	no	ASI	Successful!
<u>Nozomi (Planet B)</u> JAP	07-04-98 N/A	Orbiter N/A	MGF	ESA PET ISA EIS IMI	NS UVS	Goal: study structure and Motion of Martian upper atmosphere. Communication lost in 2002.
<u>Mars Climate Orbiter</u> USA	12-11-98 N/A	Orbiter N/A	no	no	no	Missed Mars and being destroyed.
<u>Mars Polar Lander</u> USA	01-03-99 N/A	Lander N/A	no	no	no	Communication lost before arrival.
<u>Deep Space 2</u> USA	01-03-99 N/A	Landers N/A	no	no	no	Communication lost before arrival.
2000--2009						
<u>Mars Odyssey</u> USA	04-07-01 10-24-01	Orbiter 201	no	MARIE	no	Successful to arrive Mars!
<u>Mars 2003</u> USA	May, 2003	Rovers	no	no	no	To be expected to study Mars surface.
<u>Mars Express</u> ESA	June, 2003	Orbiter Lander	no	no	ENAA	To be expected to study the atmosphere and surface of Mars.

1 Magnetic field detector.

2 Charged particles detector(s).

3 Neutral particles detector(s).

* Spacecrafts with name in boldface are, at least partially, successful.

** Decades in which the spacecrafts are launched